Volume 32 JNSChE ISSN
No. 1 2017 0794-6759

JOURNAL OF THE NIGERIAN SOCIETY OF CHEMICAL ENGINEERS

CONTENTS

DEVELOPMENT OF NEXT GENERATION FLOTATION COLUMN TECHNOLOGY FOR PROCESSING OF NIGERIAN IRON ORE 1

M.T. Ityokumbul

SYNTHESIS AND CHARACTERIZATION OF ZEOLITE A FROM ALOJI KAOLIN FOR HARD WATER SOFTENING 9

R. Abdullahi, A.S. Kovo, M. Auta, A.S. Abdulkareem and *M.O. Edoga.

UTILIZATION OF LOCAL KAOLIN AS A CATALYST SUPPORT FOR THE PRODUCTION OF CARBON NANOTUBES BY CATALYTIC VAPOUR DEPOSITION METHOD 15

Abdulkareem A. S, Suleiman B, Kariim I, Onimisi I, Kovo A. S. and Mohammed I. A.

COMPARATIVE SYNTHESIS OF SODIUM SILICATE FROM RICE HUSK AND KAOLIN 23

Ajayi, O. A., Mamman, J. and Adefila, S. S.

KINETICS AND THERMODYNAMIC STUDY OF BATCH ADSORPTION OF HEAVY METALS IN A SYNTHESIZED EFFLUENT USING RAW AND ALGINATE-FUNCTIONALIZED HUSKS 31

M. D. Yahya, I. A.. Mohammed-Dabo, A.S.Ahmed[2] and A.S Olawale.

.

OPTIMIZATION OF THE ADSORPTION OF ERICHROME BLACK-T FROM AQUEOUS SOLUTION USING NTEJE LOCAL CLAY, ANAMBRA STATE 41

Nwabanne, T. J. and Onu, E. C.

STUDY OF DRYING CHARACTERISTICS OF CASSAVA (*MANIHOT ESCULENTA*) USING A REFRACTANCE™ WINDOW DRYER 55

Akinola A. A. and S. N. Ezeorah

TRANS-ESTERIFICATION OF TOBACCO SEED OIL USING SOME AGRICULTURAL WASTES AS CATALYSTS 65

O. Motojesi, T. E. Odetoye, and D. S. Ogunniyi.

METH-ETHANOLYSIS OF CASTOR OILTO PRODUCE BIODIESEL AND ITS BLENDS WITH PETROLEUM DIESEL 77

L.O. Oyekunle, A. Jaiyeola and I. A. Adegbite

THE USE OF I_{MN} APPROXIMANTS TO ACCURATELY SOLVE STIFF DIFFERENTIAL EQUATIONS AND SYSTEMS POSSESSING STEEP AND OSCILLATORY RESPONSES 89

Femi Taiwo

Published by:
THE NIGERIAN SOCIETY OF CHEMICAL ENGINEERS
National Secretariat: Infiniti Grace House, Plot 4. Oyetubo Street,
Off Obafemi Awolowo Way, Ikeja, Lagos State, Nigeria.
E-mail: nationalhqtrs@nsche.org, nsche_headquarters@yahoo.org
Website: http:www.nsche.org.ng

JOURNAL OF THE NIGERIAN SOCIETY OF CHEMICAL ENGINEERS

A Publication on the Science and Technology of Chemical Engineering

Subscription

a.	Individual Readers	N1,500.00
b.	Overseas Subscribers	US$30.00
c.	Institution, Libraries, etc	N2,500.00

DEVELOPMENT OF NEXT GENERATION FLOTATION COLUMN TECHNOLOGY FOR PROCESSING OF NIGERIAN IRON ORE

M.T. Ityokumbul
Department of Energy and Mineral Engineering
The Pennsylvania State University
204 Hosler Building, University Park, PA 16802, USA
Email: mti1@psu.edu

ABSTRACT

Enhancing the value of mineral deposits in Nigeria will require the development of technologies for processing these ores. The reliance on turn-key projects exclusively developed outside the country for processing Nigerian mineral deposits is not good for technological advancement of the country. The development of Next Generation flotation column technology to produce concentrates for both Ajaokuta and Delta steel companies is proposed in this study. This work to be carried out by Nigerian scientists and engineers in collaboration with those in the Diaspora will mark the beginning of a new era in indigenous technology development and application in a major industrial sector with potential to increase the GDP and provide employment opportunities. While column flotation technology spans more than a century, their design and optimal applications remain a challenge. In this paper, we present the current design and scale-up protocols and discuss their limitations. It is shown that the optimal column height necessary for most applications is considerably shorter than the 10 - 17 m units that are currently deployed in industry. Against this background we highlight the research needs and approaches necessary for the development of new generation flotation column cells for use in the Nigerian mineral industry.

1.0 INTRODUCTION

Flotation is a unit operation in which separation between disperse phases is accomplished by exploiting the differences in their hydrophobicities. Traditionally, flotation has been used in mineral separation however the unit operation is now employed in the petroleum, hydrometallurgical and solid waste recycling industries (Gomez et al. 1999; Read et al. 1999; Rayak et al. 2015). In the petroleum industry, fine oil droplets must be removed from the brines prior to their disposal. Similarly, in paper recycling, ink and fine clay particles must be removed from the paper. These operations involve separation at fine sizes. With the depletion of high-grade ores, many mineral separations require grinding to finer sizes to effect liberation. In some mineral separations, liberation is achieved at fine sizes. For example, in iron ore beneficiation, the ore may be ground to 90% passing 400 mesh to effect the liberation of the silica (Eisele and Kawatra, 2007). These separations present unique processing challenges, which defy the use of conventional (mechanical) flotation technologies. With mechanical cells, entrainment of fine gangue particles into the froth product can be substantial. In the case of iron ore flotation where the silica gangue is being floated, iron losses are high when mechanical cells are used in reverse flotation.

A major development in fine particle flotation has been the introduction of bubble column flotation (commonly referred to as flotation column in the industry). A flotation column is a multiphase contactor in which air bubbles are used to effect the separation between the disperse phases. As is common with bubble column reactors and contactors, the transport, dispersion and mixing of materials and energy is induced by the passage of the discontinuous gas phase (in the form of air bubbles) in the continuous liquid or slurry phase. As presently operated in industry, flotation columns have three zones, the recovery or scavenging, cleaning and froth zones (Idlas et al. 1990a, b).

The recovery zone extends from the feed inlet point to the base of the column. In this region, particles suspended in the descending slurry or liquid phase contact a rising swarm of air bubbles, generated at the base of the column. Floatable particles that collide with and adhere to the air bubbles are transported to the cleaning zone. Gangue particles are removed from the base of the column as tailings. The cleaning zone extends from the feed inlet to the pulp-froth interface. In the cleaning zone, the particle-laden air bubbles come in contact with a progressively cleaner pulp descending from above. In the ensuing interaction, the cleaner pulp replaces the slurry entrained with the rising

air bubbles. The cleaner pulp is generated by the addition of wash water in the froth zone. Unlike the recovery and cleaning zones, the gas phase is effectively continuous in the froth zone. The coalescence of air bubbles in the froth zone reduces the surface area available for particle collection. In this regime, the ensuing competition for bubble surface favors the more hydrophobic particles while the entrained hydrophilic particles are rejected. The fresh water that is added in the froth zone washes the rejected hydrophilic particles back into the recovery zone. Thus, the combined effects of bubble coalescence and wash water addition help to reduce the recovery of hydrophilic gangue particles, thereby minimizing concentrate contamination. The advantages and disadvantages of using column flotation have been given in the elsewhere in the literature (Wheeler, 1966; Dobby and Finch, 1986; Ityokumbul, 1986).

Flotation columns were first developed and patented in the mid-1910s by Flinn and Towne (Gahl, 1916). The unit was first deployed at Inspiration Copper Company, however, the column was plagued by settlement of solids on the gas distributor and its use was discontinued. It has been shown that when solids settle on porous gas distributors, large slugs of bubbles are formed (Ityokumbul, 1986). In addition to reducing the bubble surface area available for particle collection, slug formation introduces considerable turbulence in the cell, thus promoting particle detachment from the bubble surface.

The failure of the first column installations at Inspiration Copper has been traced to an inherent flaw in the design of the sparger and tailings discharge assembly. In the initial design, the gas distributor was a flat porous plate, which covered the column cross-section leaving a relatively small hole in the center for tailings withdrawal. Hydrodynamic characterization of fluid flow near the sparger would indicate the existence of stagnation points near the column wall where the solid particles tended to settle. This design flaw was overcome in the flotation column designs introduced in the 1950s and 1960s (Hollingsworth, 1956, 1967; Wheeler, 1966).

Currently flotation column separations are carried out in units that are 10-17 m tall. While laboratory and pilot plant studies typically show good separation results, these are often not realized in full scale plant installations. This has led to some high profile column installation failures in many places around the world including the platinum industry in South Africa, the iron ore industry in the USA. These engineering failures are attributed to the adoption of inappropriate design and scale-up protocols. In this paper, we will briefly discuss the shortcomings of the current design and scale-up protocols for flotation columns from a chemical engineering perspective. An alternative approach to flotation column design and scale-up will be presented which will facilitate the development of a next generation (NEXTGEN) of flotation columns. The research and development work on these cells can be demonstrated using Nigerian iron ores in collaboration with Nigerian scientists and engineers. Research and development work is necessary if the country is to develop technologically and move from a consumer of technology developed elsewhere to an exporter of such technology.

2.0 LIMITATIONS OF CURRENT DESIGN AND SCALE-UP PROTOCOLS

The current design and scale-up of flotation columns utilize chemical reaction engineering principles (Dobby and Finch, 1986). In this approach, flotation kinetics is assumed to be first order while the behavior of solids is described using a sedimentation dispersion model. Accordingly, the recovery is given by

$$(1-R) = \frac{4\,a\,exp\left(\frac{Pe_p}{2}\right)}{(1+a)^2\,exp\left(\frac{Pe_p}{2}a\right) - (1-a)^2\,exp\left(-\frac{Pe_p}{2}a\right)} \quad (1)$$

$$a = \left(\frac{1+4\,k\,\tau_p}{Pe_p}\right)^{0.5} \quad (2)$$

$$\tau_p = \frac{L\,(1-\varepsilon_g)}{U_r + V_p} \quad (3)$$

$$Pe_p = \frac{L\,(U_r + V_p)}{E_p\,(1-\varepsilon_g)} \quad (4)$$

Where R is the fractional recovery and Pe_p is the particle Peclet number.

In Equation 2, τ_p, V_p, E_p are the particle residence time, settling velocity and dispersion coefficient respectively, while L, U_r, and ε_g are the column height, slurry velocity and average gas hold-up in the recovery zone respectively. While using chemical reaction engineering principles to size flotation columns may appear to be technically sound, the foregoing will demonstrate the flaws inherent with this protocol. There are several reasons why the use of Equation 1 to estimate the recovery may not be correct.

Firstly, Equation 1 predicts that the recovery should increase with column height (or particle residence time). This will explain the current use of columns that are 10-17 m tall. Unfortunately, flotation is a process that depends on the loading of air bubbles. If the bubbles are fully loaded over a height of 1-2 m, increasing the column height beyond that will have no effect on recovery. In fact in very tall columns, the bubble size will grow as the hydrostatic head decreases. This will even have the negative effect of promoting particle detachment from the bubbles thus reducing the bubble load (and consequently the recovery).

Secondly, for first order kinetics, the recovery should be independent of concentration. This is not the case in flotation where the recovery depends on the ratio of particle to bubble surface area (Ityokumbul and Trubelja, 1998). Experimental data from the work of Ityokumbul and Trubleja (1998) has shown that the recovery is independent of the particle to bubble surface area ratio for values less than 0.5. However, the recovery is inversely proportional to the particle to bubble surface area ratio above 0.5. The value of 0.5 for the particle to bubble surface area ratio is significant in that it suggests that the bubble capacity is reached when 50% of the surface is covered.

Thirdly, the use of a sedimentation dispersion model to describe the behavior of solid particles in a flotation column has been questioned (Ityokumbul, 1993). For example, Yiannatos and Bergh (1991) reported data on solid dispersion coefficients in an industrial size flotation column which appear to show that the solid particles were more mixed than the liquid phase (see Table 1). Furthermore, the solid dispersion data showed that the larger particles were more mixed than the smaller ones! This is not feasible as the larger particles are less likely to follow the liquid streamlines and as such their behavior is least likely to mimic that of the liquid phase. Ityokumbul et al (2000) have shown that under typical flotation conditions, only particles less than about 20 m are likely to follow the liquid streamlines. Thus, it is expected that if anything, the mixing coefficient of the larger particles should be lower than that of the liquid or smaller particles.

Table 1: Liquid and Particle Dispersion Parameters in a 0.91 m x 12 m Flotation Column (Yiannatos and Bergh, 1991)

Material	residence time, min	N_d = 1/Pe	Dispersion coefficient, m^2/s
Liquid	16.8	0.58	0.036
-38 □m	16.2	0.55	0.036
-75 +38 □m	13.2	0.69	0.055
-150 + 75 □m	8.7	10.0	1.23

In order to explain this apparent paradox one has to consider the physics of the process. The use of a diffusive-type flux requires that the perturbations in the system be random in nature (Ityokumbul, 1993). Unfortunately, this is not the case with solid particles which have a finite settling velocity. As with all slurry bubble column reactors, there is a constant relative velocity between the solid particles and the liquid phase. According to Levenspiel and Fitzgerald (1983), the existence of a constant relative flow between the phases is characteristic of Gaussian convection models. As a result of the higher terminal settling velocity of the larger particles, this class of particles will be the first to show up in the column exit. This observation is supported by the experimental data of Yiannatos and Bergh (1991). Unfortunately, the sedimentation-dispersion model interprets the early arrival of these larger particles to be the result of more mixing which is clearly not the case.

3.0 NEW APPROACH TO FLOTATION COLUMN DESIGN AND SCALE-UP

As indicated above, the current design and scale-up protocols for flotation columns are not correct. These design protocols have resulted in flotation column cells that are typically 12-17 m tall. Installation of such columns has led to numerous failures in the platinum and iron ore processing industries. For proper design of bubble column flotation cells, mathematical models of the processes taking place are required. Shah and Deckwer (1985) have given a flow path for the design and modeling of reactors. The application of this procedure requires detailed information on the material flow pattern in the reactor and a careful isolation of the important rate-determining steps and how these change with the scale of the reactor. In the case of flotation, the process leading to separation is the selective collection of hydrophobic particles by air bubbles. Thus, the development of a mechanistic model of the flotation process must focus on the bubble loading rates.

From a review of the various microprocesses involved in particle collection, Jameson et al (1977) have questioned the validity of applying the analogy between chemical kinetics and the flotation process. These authors have argued that flotation has more in common with interface mass or heat transfer than with chemical kinetics. In the light of this, several authors have developed mass transfer approaches to flotation column studies (e.g. see Ityokumbul, 1986, 1992a, b; Idlas et al. 1990a, b).

A practical and significant conclusion from the application of mass transfer principles to flotation column analyses has been the finding that short columns (3-4 m) can be successfully deployed in industry (e.g. see Ityokumbul, 1992a, b; 1993; 1995; Ityokumbul and Trubelja, 1998). Indeed, our results are consistent with the first flotation column installation which was only 2.1 m tall (Gahl, 1916). This observation contrasts sharply with current industrial practice of using tall columns (12-17 m) and was not readily accepted when it was first presented in the published literature. However, recent industrial successes with short columns validate these new approaches to the study, design and scale-up of column cells (Ityokumbul, 1996; Beneficiation Technologies, 1998; Ityokumbul et al. 2003,2005).

In separation processes, it is often convenient to characterize the difficulty of the separation using the height of transfer unit (HTU). Under free flotation conditions (i.e. when bubble surface area is not limiting), the HTU was shown to be (Ityokumbul, 1992b):

$$HTU = \frac{(U_r + V_P)}{ak\Gamma_m} \qquad (5)$$

In Equation 5, U_r and V_p are the slurry and particle settling velocities in the recovery zone, ***a*** is the bubble interfacial area, k and Γ_m are the particle transfer rate constant and maximum bubble load respectively. The product, $k\Gamma_m$, in Equation 5 is analogous to an *interfacial mass transfer coefficient*. Equation 5 suggests that the HTU decreases with increasing bubble surface area. Since the maximum bubble load decreases with particle size, the HTU should increase with decreasing particle size. This finding explains the standard practice of desliming the feed to flotation circuit.

i. An estimate of the HTU from a number of applications in flotation columns of different sizes has been made and the results are shown in Table 2.

ii.

Table 2: Estimates of HTU for Different Column Applications

Source	Application	Column Diameter, m	HTU, m
Luttrell et al., 1988	Coal	0.05	0.29
Bensley et al., 1985	Coal	0.10	0.28
Reddy et al., 1988	Coal	0.10	0.43
Kho and Sohn, 1989	Talc	0.06	0.26
Ounpuu and Tremblay, 1991	Sphalerite	1.20	0.48
Ynchausti et al., 1988	Fluorite Pyrolusite	0.06 0.06	0.70 1.50

The results in Table 2 showed that coal and talc had lower HTU relative to the other solid particles. This finding was expected as coal and talc are naturally hydrophobic minerals. These results showed the validity of the new mass transfer approach to column flotation design and scale-up. Ityokumbul and Trubelja (1998) had shown that the fractional yield in coal flotation increased with the ratio of bubble to particle surface areas. Similarly, Gorain et al. (1987) had shown that in conventional flotation cells (mechanical cells), the flotation throughput is dependent on the particle characteristics and the flux of the bubble surface area (surface area generation rate per unit area). These findings provide additional affirmation of the interfacial nature of flotation.

It is evident from the foregoing that the development of next generation flotation columns will have wide application for the efficient processing of Nigerian ores. It is noted that such technology can have broad appeal and form the basis for an indigenous company producing and marketing such technology worldwide.

4.0 RESEARCH AND DEVELOPMENT NEEDS IN THE NIGERIAN MINERAL INDUSTRY

The immediate and short-term research and development needs necessary for the successful take-off of the Nigerian mineral industry are in the areas of institutional and human capacity development. A national workshop on solid minerals development in Nigeria held at the University of Jos, June 2-5, 2008, issued a communique which recommended among other things:

i. The establishment of a Solid Minerals Technology Development Fund to support capacity building efforts in the sector

ii. The mandate of the Petroleum Technology Development Fund be expanded on the short term to cover capacity building in the Solid Minerals Sector

iii.

The adoption of an AMIRA-type model to support research activities in our tertiary institutions. Selected Universities and polytechnics may be designated as centers of excellence in mineralsrelated education

Since this workshop, Kaduna Polytechnic has been designated as a center of excellence in solid mineral development and the Nigerian Institute of Mining and Geosciences has been established in Jos with funding from the World Bank. While these efforts are laudable, more work is needed before the critical technological know-how and manpower needed for the take-off of the solid minerals can become a reality. In particular, there is an urgent need to put in place a sustainable funding mechanism to support research and training in mining and mineral research. The training needs must cover all levels of manpower including laboratory and technical staff. To underscore the need for training of technical staff for the industry, we note that Ola et al. (2009) attempted to upgrade the Itakpe sinter grade iron ore to Midrex-grade super concentrate using a three stage cleaning process: rougher, cleaning and recleaning. Unfortunately, the data showed that the highest grade was obtained in the rougher stage; a result that would suggest that sand was being added in the cleaning and recleaning stages. A plausible explanation of the results could be sampling and/or analytical errors. The urgency for undertaking institutional and human capacity development is rooted in the fact that this will pave way for successful takeoff of the mineral industry and this will significantly enhance revenue generation, employment opportunities thus contributing to poverty alleviation.

5.0 IRON ORE PROCESSING

Currently, the Nigerian Iron Ore Mining Company, NIOMCO, is the only company mining the iron ore deposits at Itakpe in Kogi State. NIOMCO is designed to produce:

- 550,000 TPY of a 67-68% Fe super concentrate for the Delta Steel Company
- 2,150.000 TPY of a 63% Fe concentrate for the Ajaokuta Steel Company

The plant was designed to operate four processing lines. Three of the lines were completed and employ a network of spirals and low intensity magnetic separation to produce a concentrate for the Ajaokuta Steel Company (ASC). The fourth line was being developed to produce a super-concentrate for the Delta Steel Company (DSC). The 4th line was to employ fine grinding of the sinter-grade concentrate and to employ reverse flotation with a suitable amine collector to remove the silica from the iron ore. The configuration of the flotation circuit is detailed below:

- A bank of 5 WEMCO cells each equipped with 11 kW motor to be used in cleaner operations. A bank of 4 WEMCO cells each equipped with 30 kW motor to be used in rougher operations
- A bank of 3 WEMCO cells each equipped with 30 kW motor to be used in scavenger operations.

The installed flotation lines employ conventional flotation circuits which are not very efficient when processing extremely fine or coarse feed material. In addition, the operation of the 4th line is going to be more cost intensive relative to the other three lines due to the need for fine grinding, coupled with the use of mechanical cells with high power and chemical (amine collector and frother) consumption. This will impact the unit production cost for the super concentrate needed for the Delta Steel Company.

Ityokumbul et al. (2003, 2005) have shown that fine and coarse silica can be removed by flotation in a column cell. Currently, the Florida phosphate plants employ conventional flotation cells for this separation. Our study was the first to demonstrate that shorter column cells could be employed for this separation. In real-time plant and column flotation performance data, the column was shown to outperform the conventional flotation cells (similar to those being installed Itakpe) while using 40-50% of the plant amine dosage. The work was carried out in a Dual Extraction Column (DEC) at several phosphate plants in Florida at feed rates of up to 5 tons per hour (TPH) at five different operating plants (Ityokumbul, 2003). Since the amine to be used at Itakpe will be imported at considerable costs reduction in amine consumption should reduce the unit production cost for the high grade iron ore needed for the direct reduction plant. Thus there is a need to carry out this type of research at NIOMCO using plant, NMDC staff and postgraduate students pursuing advanced degrees in Nigerian Universities.

6.0 CONCLUSION

There is need for Nigeria to develop technology that can be deployed in the efficient and sustainable development of its vast mineral resources. This will require putting in place a process for building the essential institutional and human capacity necessary for the successful take-off of the solid minerals industry. A funding mechanism for research and development is needed. This could take the form of a tax on minerals extracted from the ground. Such funding could be used to develop the next generation of column cells to be

used in processing Nigerian iron ore and other mineral resources. Rather than pay for turn-key projects in the mineral industry, government should promote the development and incorporation of research from Nigerian research institutes. A mechanism should be put in place that will allow Nigerians based in the Diaspora to work with counterparts in Nigeria on joint research projects that will contribute to the successful take-off of the mineral industry in Nigeria. In this way, we can turn the brain drain to brain gain.

REFERENCES

Beneficiation Technologies, "New Advanced Flotation Cell." Publication from Beneficiation Technologies, LLC. (1998).

Bensley, C.N., Roberts, T. and Nicols, S.K., "Column Flotation for the Treatment of Fine Coal." *Proc. 3rd Australian Coal Preparation Conference*, Wollong, NSW, Australia, pp. 87-103 (1985).

Dobby, G.S. and Finch, J.A., "Flotation Column Scale-up and Modelling," *CIM Bulletin*, **78**, pp. 89-97 (1986).

Eisele, T.C. and Kawatra, S.K., "Reverse Column Flotation of Iron Ore." *Minerals and Metallurgical Processing*, **24**, pp. 61-66 (2007).

Gahl, R., "History of the Flotation Process at Inspiration." *Trans. AIME*, **55**, pp. 576-645 (1916).

Gomez, C.O., Acuna, C., Finch, J.A. and Pelton, R., "Aerosol-Enhanced Deinking of Recycled Paper by Column
Flotation." Proceedings, Research Forum on Recycling, pp. 129-132 (1999).

Gorain, B.K., Franzidis, J.P. and Manlapig, E.V., "Studies on Impeller Type, Impeller Speed and Air Flow Rate in an Industrial Scale Flotation Cell. Part 4: Effect of Bubble Surface Area Flux on Flotation Performance." *Minerals Engineering*, **10**, pp. 367-379 (1987).

Hollingsworth, C.A., "Concentration of Minerals." *US Patent No. 2,758,714*, (1956).

Hollingsworth, C.A., "Concentration of Minerals." *US Patent No. 3,298,519*, (1967).

Idlas, S.A., Fitzpatrick, J.A. and Slattery, J.C., "Conceptual Design of Packed Flotation Columns." *Ind. Eng. Chem. Res*. 29, 943-949 (1990a).

Idlas, S.A., Fitzpatrick, J.A. and Slattery, J.C., "Conceptual Design of Staged Flotation Columns." *Ind. Eng. Chem. Res*. 29, 949-955 (1990b).

Ityokumbul, M.T. and Trubelja, M.P., "Carrying Capacity in a Pilot Flotation Column." *Minerals and Metallurgical Processing*, **15**, pp. 41-46 (1998).

Ityokumbul, M.T., "A Mass Transfer Approach to Flotation Column Design," Proc., 1st. International Conference on Gas-Liquid and Gas-Liquid-Solid Reactor Engineering, Columbus, OH, September 13-16, *Chem. Eng. Sci.* **47**, pp. 3605-3612 (1992b).
Ityokumbul, M.T., "A New Modelling Approach to Flotation Column Design," *Minerals Engineering*, **5**, pp. 685-693 (1992a).

Ityokumbul, M.T., "Hydrodynamic Study of Bubble Column Flotation." Ph.D. Thesis, University of Western Ontario, London, Canada, 187p (1986).

Ityokumbul, M.T., "Selection of Recovery Zone Height in Flotation Column Design," *Chem. Eng. Process*. **32**, pp. 77-82 (1993).

Ityokumbul, M.T., "Amine Flotation of Rougher Concentrate and Intermediate Pebble in a Column Cell." Final Report for work performed for the Florida Institute of Phosphate Research under Contract No. 00-02-147R and 0002-147S (Publication No. 02-147-199).

Ityokumbul, M.T., Brooks, G., Yensco, M. and Ellington, J.T., "Pilot-Plant Evaluation of Amine Flotation of Rougher Phosphate Concentrate in a Column Cell." *Minerals and Metallurgical Processing*, **20**, pp. 52-56 (2003).

Ityokumbul, M.T., Brooks, G., Yensco, M., Ellington, J.T. and Mcquien, G.E., "Coarse Silica Flotation from Intermediate Pebble Product in a Dual Extraction Column." *Minerals and Metallurgical Processing*, **22**, pp. 77-82 (2005).

Ityokumbul, M.T., de Aquino, J.A., Harris, M.C. . and O'Connor, C.T "Fine Particle Recovery in an Agitated Column Cell." *Int. J. Min. Process*. **58**, pp. 167-178 (2000).

Ityokumbul, M.T., Kosaric, N. and Bulani, W., "Effect of Fine Solids and Frother on Gas Hold-up and Liquid Mixing in a Flotation Column." *Minerals Engineering*, **8**, pp. 1369-1380 (1995).

Jameson, G.J., Nam, S. and Moo-Young, M., "Physical Factors Affecting Recovery Rates in Flotation." *Min. Sci. Eng*., **9**, pp. 103-118 (1977).

Kho, C-J. and Sohn,H.-J., "Column Flotation of Talc." *Int. J. Min. Process*. **27**, pp. 157-167 (1989).

Levenspiel, O. and Fitzgerald, T.J., "A Warning on the Misuse of the Dispersion Model." *Chem. Eng. Sci.* **38**, pp. 489-492 (1983).

Luttrell, G.H., Weber, A.T., Adel, G.T. and Yoon, R.H., "Microbubble Flotation of Fine Coal," in *Column Flotation '88*, K.V.S. Sastry (ed.), SME Littleton, CO, pp. 205-211 (1988).

Ola, S.A., Usman, G.A., Odunaike, A.A., Kollere, S.M., Ajiboye, P.O. and Adeleke, A.O., "Pilot Scale Froth Flotation to Upgrade Nigerian Itakpe Sinter Grade Iron ore to a Midrex-Grade Super-Concentrate." *J. Minerals and Materials Characterization and Engineering*, **8**, pp. 405-416 (2009).

Ounpuu, M. and Tremblay, R., "Investigation into the Effect of Column Height on the 1200 mm Diameter Column at Matagami," *Proceedings of the International Conference on Column Flotation.* G.E. Agar, B.J. Huls and D.B. Hyma (eds.), Sudbury, Ontario, June 2-6, Vol. 1, pp. 303-316 (1991).

Rayak, V.K., Relish, K.K., Kumar, S. and Mandal, A., "Mechanism and Separation of Oil from Oil-in-Water Emulsions by Air Flotation.' *Petroleum Science and Technology*, **33**, pp. 1861-1868 (2015).

Read, S,J., Lees, G.C. and Hurst, S.J., "Separation of PET from PVC Using Column Flotation." *Polymer Recycling*, **4**, pp. 1-11 (1999).

Reddy, P.S.R., Kumar, S.G., Bhattacharyya,K.K., Sastri, S.R. and Narisimhan, K.S., "Flotation Column for Fine Coal Cleaning." *Int. J. Min. Process*. **24**, pp. 161-171 (1988).

Shah, Y.T. and Deckwer, W.D., "Fluid-Fluid Reactors" in *Scale-up in Chemical Process Industries*, R. Kabel, and A. Bisio (eds.)., J. Wiley, New York (1985).

Wheeler, D.A., "Big Flotation Column Mill tested." *Eng. Min. J*., **167**, pp. 98-102 (1966).

Yiannatos, J.B. and Bergh, L.G., "RTD Studies in an Industrial Flotation Column: Use of Radioactive Tracer Technique." *Proceedings of the International Conference on Column Flotation.* G.E. Agar, B.J. Huls and D.B. Hyma (eds.), Sudbury, Ontario, June 2-6, Vol. 1, pp. 221-234 (1991).

Ynchausti, R.A., McKay, J.D. and Foot, D.G. Jr., "Column Flotation Parameters – Their Effects." *Column Flotation '88*, K.V.S. Sastry (ed.), SME, Littleton, CO, pp. 157-172 (1988).

SYNTHESIS AND CHARACTERIZATION OF ZEOLITE A FROM ALOJI KAOLIN FOR HARD WATER SOFTENING

Rekiya Abdullahi, A.S. Kovo, Manese Auta, A.S. Abdulkareem and *M.O. Edoga
Department of Chemical Engineering, Federal University of Technology, Minna
*Department of Chemical Engineering, Federal University, Ndufi Aliki, Ebonyi State
kovo@futminna.edu.ng,

ABSTRACT

Aloji kaolin was used as a combined source of silica and alumina to synthesize zeolite A and was thereafter used to soften hard water sourced from a local well in Minna. The raw Aloji kaolin was purified via sedimentation process and was followed by metakaolinization at 800^{0}C for 3 h to obtain reactive metakaolin phase material. The metakaolin obtained were used to synthesized zeolite A through conventional hydrothermal crystallization method. The synthesized zeolite A was characterized by SEM and XRD. The optimum synthesis parameters of zeolite A synthesized through conventional hydrothermal route were 3M NaOH, crystallization temperature of 90^{o}C and crystallization time of 72 h after aging for 24 h at room temperature. The crystallinity of synthesized A through conventional hydrothermal route ranged from 40 - 70%. The synthesized zeolite A was used for softening an underground (well) water containing 48 ppm of calcium ions. Zeolite A was able to remove 98% of the calcium ion content from the hard water within 5 mins of 20 mins treatment time and this treatment was carried under normal conditions.

Keyword: Zeolite A, Aloji kaolin, Metakaolinization, synthesis, Hard water, X-ray diffraction (XRD), Scanning Electron microscopy (SEM)

1.0 INTRODUCTION

Zeolites are crystalline aluminosilicates material with uniform pores, channels and cavities. The structure of zeolites contains aluminum, silicon, and oxygen in regular frameworks with cations and water in the pores (Meier *et al*., 1996). In zeolite A silicon and aluminum are tetrahedrally coordinated with each other through shared oxygen atoms. Each AlO_4 tetrahedron in the framework bears a net negative charge which is balanced by a cation. (Xu *et al*., 2007). Zeolite has a wide range of applications in catalysis, separation processes, ion-exchange and these has resulted in the use of zeolite, whether in synthetic or natural form, in many process industries such as petrochemical, nuclear agriculture, construction, heating and refrigeration, Biogas and medical (Guglielmo *et al*., 2007; Jana *et al*., 2007; Rowe *et al.*, 2008). The structural formula of zeolite is based on the crystallographic unit cell, the smallest unit of structure, represented as

$$M_{x/n}\,[(AlO_2)_x(SiO_2)_{y.\,wH2}O \quad \text{(Bekkum,1991)}$$

Where M is an alkali or alkaline earth cation, n is the valency of cation, w is the number of water molecules per unit cell, x and y are the total number of tetrahedral per unit cell and the ratio y/x usually has values of 1 to 5. In the case of the high silica zeolite, y/x can range from 10 to 100.

Generally, zeolite is synthesized from sodium aluminosilicate gel formed from various silica and alumina source by hydrothermal treatment. However, the preparation of synthetic zeolites from chemical source of silica and alumina is expensive The search for a cheap source of silica and alumina for the synthesis of zeolite motivated most researchers to use different geological materials and industrial wastes like coal fly ash, (Tanaka *et al.*, 2009), bagasse fly ash (Purnomo *et al*., 2012), Oil shale ash (Machado *et al*., 2005), Kaolinite, (Heller-Kallai *et al*., 2007) and paper sludge, (Wajima *et al.*, 2006).

The use of kaolin to synthesize zeolite has continued to gain popularity over the years. Kaolin ($Al_2O_3.2SiO_2.2H_2O$) is a two layered aluminosilicate clay mineral, consisting of one alumina octahedron sheet and one silica tetrahedron sheet in a 1:1 stoichiometric ratio. It has been used as a starting material for the synthesis of zeolite (Jing-Quan *et al.*, 2014).

Further processing of the kaolinite is required for use in zeolite synthesis either by eliminating aluminium or adding silica in a suitable form (Delucas *et al.*, 1992, and Novembre *et al*., 2011).

Zeolite synthesis from kaolin is usually carried out using the conventional hydrothermal method.

The conventional hydrothermal synthesis of zeolite from kaolin involves two basic steps: metakaolinzation, which is the calcination of the raw kaolin at high

temperature to change the chemically stable kaolin into a very reactive but amorphous material. Metakaolin (Al_2O_3. $2S_iO_2$), a calcined product of kaolin is a convenient starting material for the synthesis of zeolite A after it is hydrothermally treated with sodium hydroxide (Lijalim *et al.,* 2015; Carlos Alberto *et al.,* 2010; Kovo *et al*.,2010; and Jalil *et al.,* 2010).

During the past years many studies had been reported on the synthesis of zeolite A from natural kaolin clay (Lijalem *et al.,* 2015), but no attempt has been made to date to produce zeolite A from Aloji kaolin deposit of kaolin located in Kogi state, Nigeria.

2.0 MATERIALS AND METHODS

2.1 Materials and Pretreatment

Raw Aloji kaolin was sourced from Aloji, Kogi State and refined via sedimentation process following the procedure adopted by Alaya *et al* (2014) and thereafter characterized using SEM and XRD. The metakaolin was prepared at 800^{o}C for 3 h and characterized. Sodium hydroxide (98% purity (NaOH), analytical reagent grade, supplied by Aldrich chemical, Germany, was used for the synthesis of zeolite A.

2.2 Synthesis of Zeolite A using Conventional Hydrothermal Methods.

3g of metakaolin was sieved for mesh size of (500 mesh). The metakaolin was mixed with 50 mL of 1M NaOH solution for hydrothermal crystallization at 90^{o}C for 72 h after aging for 24 h. The solid was filtered out and washed with deionized water until the pH was 8. The sample obtained was dried in an oven at 90^{o}C for 8 h. The above procedure was repeated for different concentrations of NaOH, crystallization temperature and crystallization time as presented in Table 1. The zeolite samples obtained were characterized using SEM and XRD.

Table 1: Synthesis of Zeolite A using Conventional Hydrothermal Methods.

Samples	Concentration of NaOH (M)	Crystallization temperature ^{0}C	Crystallization time in h
AC1	1	90	72
AC3	3	90	72
$AC4_1$	4	90	24
$AC4_2$	4	90	72
$AC4_3$	4	100	72
$AC4_4$	4	110	72

2.3 Application of Synthesized Zeolites in Water Softening

Softening of water was done using the procedure of Loiola *et al*., (2012) with some modifications. 50 mg of synthesized zeolite was added to 20ml of analysed local well water. The samples were stirred at 75 % of maximum speed of the magnetic stirrer (1400 rev/min) at room temperature for 5 mins. It was then filtered and stored in plastic container for Atomic absorption spectrometer (AAS) analysis. These processes were repeated for 10, 15, 20 and 25minutes.

3.0 RESULTS AND DISCUSSION

3.1 Characterization of Aloji Kaolin

The constituent and morphology of the clay was ascertained using SEM. The kaolin was refined using sedimentation process. The SEM images of raw and refined Aloji kaolin are shown in Figure 1

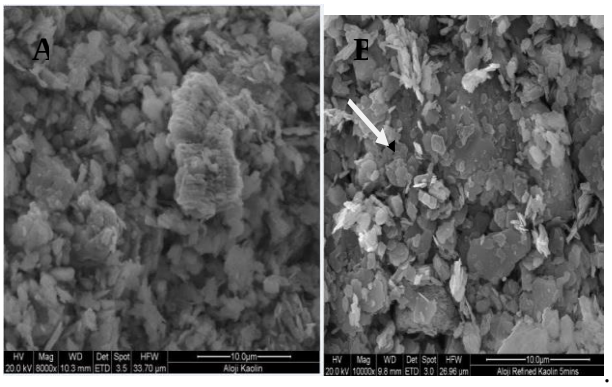

Figure1 (A)The SEM image of raw Aloji kaolin (B)The SEM image of refined Aloji kaolin

The images in Figure 1 showed that refining of the clay had taken place as a result of reduction of silica content. Quartz is known to be the main impurity in Kaolin and the refining process is expected to eliminate this non associated mineral, which exists as SiO_2. The refining process can be considerd successfully as evidence in the SEM images which showed the platy nature of kaolin. Kaolin can be recognized by its platy morphology and hexagonal outlines with small well formed hexagonal plates loosely packed (Novembre *et al*, 2011) as indicated by the arrow in Figure 1 B.

The angular orientation of SEM image A denotes the consolidation of quartz within clay mineral as shown in Figure 1 A (Nakagawa *et al.,* 2006).

The XRD pattern of refined Aloji kaolin presented in Figure 2 showed a peaks at 2θ values of 12.50^0, 24.64^0 which are the characteristic peaks of kaolinite materials. The peaks of quartz were at 2θ values of 21^0, 26.6^0 and 36.5^0 and mica was also noted at 19.20^0 which were the minor impurities associated with kaolinite (Yunan Ma

et al., 2014). Further refining is not required to completely eliminate the quartz and mica content because of the kaolin refinement is slow process however small quantities of these impurities in kaolinite do not impair the formation of zeolitic materials.

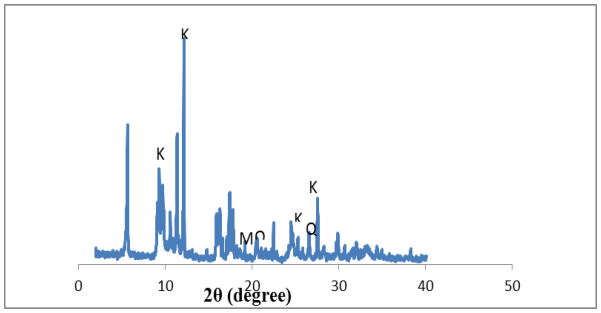

Figure 2: XRD pattern of refined Aloji kaolin

3.2 Metakaolinization

Calcination of Aloji kaolin was done at 800°C for 3 h. The XRD results of the refined kaolin earlier presented showed that the kaolin had a lot of impurities even after the refinement and for a reactive metakaolin to be achieved from such low grade kaolin, the metakaolinization temperature had to be increased (Jing-Quang *et al.*, 2014) and (Mostafa *et al.*, 2011). The XRD pattern exhibit some changes compared to that of kaolin (Figure 3). The disappearance of the diffraction peaks of kaolin corresponded to the appearance of amorphous aluminosilicate which is as a result of thermal treatment of the raw kaolin form metakaolin, an amorphous material. The highest diffraction peaks corresponded to the presence of quartz (SiO_2) at 26.65^0 and 36.55^0, which is due to the thermal stability of quartz remaining as an impurity in some synthesized zeolite.

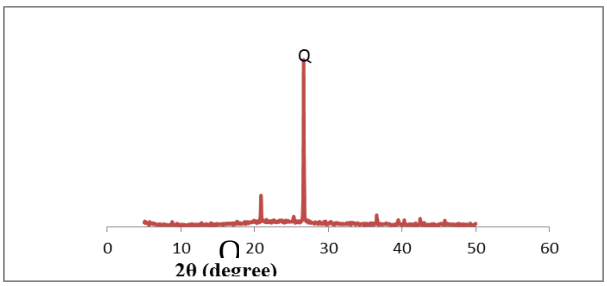

Figure 3: XRD pattern of metakaolin

3.3 Zeolite A Synthesis

The XRD Pattern of Synthesized Zeolite A

The XRD pattern of synthesized zeolite A from conventional hydrothermal route has the characteristics intensity peaks of zeolite A at 2θ values of 7.18, 10.17, 12.49, 17.6, for (AC1, AC3, $AC4_3$, $AC4_4$) respectively and which is very similar to the XRD pattern of commercial zeolite A as reported by Traecy and Higgins 2001. Some weak reflections were also observed at 2θ value of 24.04, 47.43 and 48.03 for ($AC4_1$ $AC4_2$,) which are all characteristics diffraction peaks of zeolite A. The percentage crystallinity ranged from 63 – 70% with AC3 having the highest crystallinity. The XRD pattern of synthesized zeolite A form conventional hydrothermal route is shown in the Figure 4:

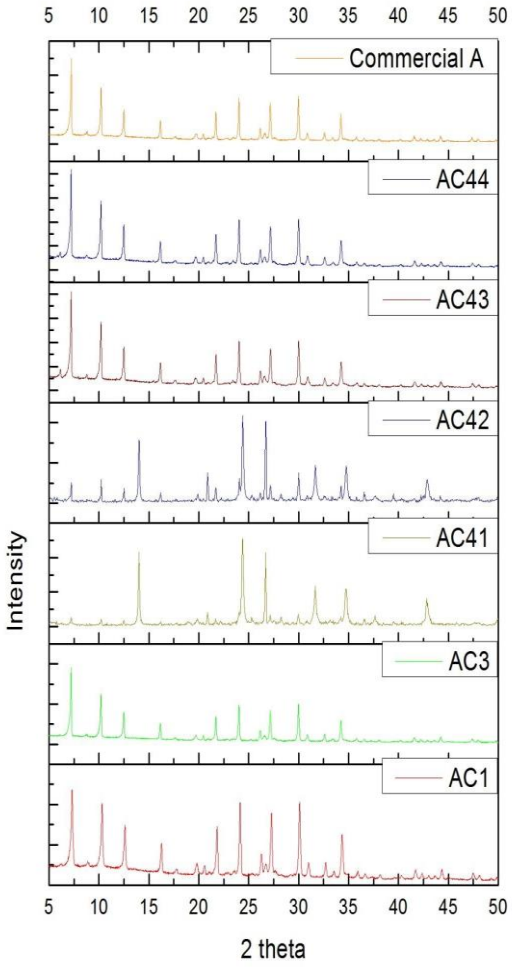

Figure 4: XRD Pattern of Synthesized Zeolite A (Convectional Hydrothermal Method)

SEM Images of Zeolite A Through Conventional Hydrothermal Route

The morphology of the synthesized zeolites A were shown by the Scanning Electron Microscopy (SEM) images in Figure 5.

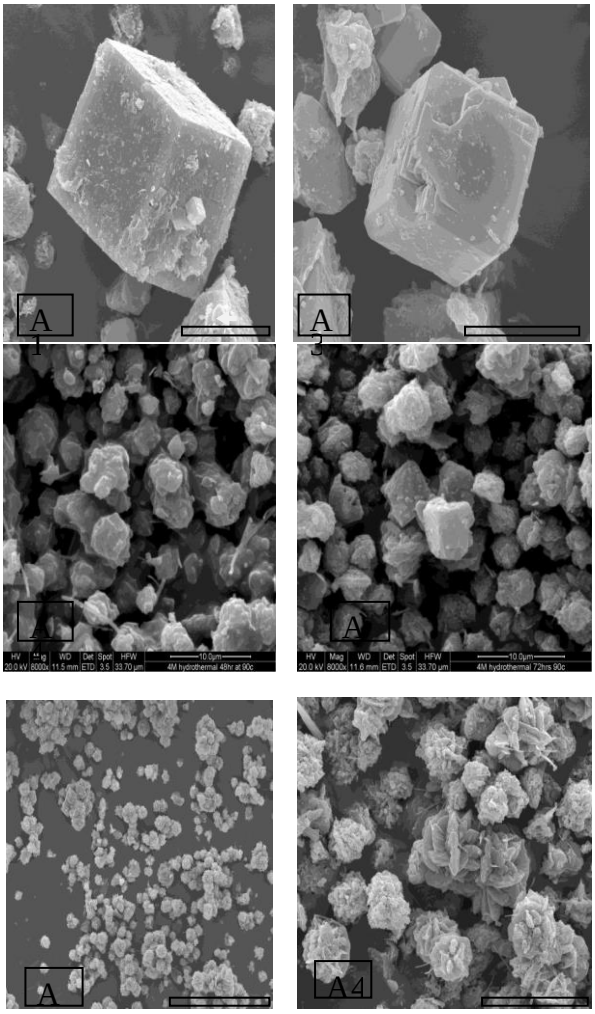

Figure 5: SEM images of Synthesized Zeolite A (Conventional Hydrothermal Routes)

The SEM showed some well developed cubic crystals for AC1, AC3 and $AC4_3$ typical of zeolte A. (Lijalem *et al.,* 2015). The cubic crystals were obtained from the sythesis of 3 M and 4 M NaOH which were the maximum NaOH concentration in the sythesis of zeolite A from metakaolin (Lijalem *et al*., 2015 and Novembre *et al*, 2011). The presence of gel in $AC4_1$ and $AC4_2$ was as a result of some crystal not fully grown from metakaolin as observed by Salami (2015). The morphology of $AC4_4$ was different from others above having the highest crystallization temperature, although no significant improvement in morphology was observed with increase in concentration of NaOH (Janijira, 2002). This might be attributed to attainment of maximum crystal growth occasioned by delayed nucleation. The percentage crytsallinity as determined using the XRD outcome showed the range of crystallinity from 1.98 - 63.62% (Table 2). The crystallinitty of AC3 was the highest followed by $AC4_4$.

Table 2: Percentage Crystallinity of Synthesized Zeolite A

Conventional Hydrothermal Samples	Samples % Crystallinity
AC1	63.36
AC3	70.63
$AC4_1$	1.98
$AC4_2$	2.09
$AC4_3$	63.62
$AC4_4$	66.48

3.4 Effect of Synthesis Parameters

Effect of Alkalinity

One of the most important synthesis parameter that controls the crystallization of zeolite is the concentration of the base. Increase in alkalinity caused increase in crystallization rate. This was due to rapid increments of solubility of the amorphous aluminosilicate precursor. Increase in alkalinity increased nucleation rate and polymerization rate between polysilicate and aluminate anions (Musyoka, 2009). The study of the effect of concentration of NaOH was screened at 1M, 3M and 4M in the synthesis of zeolite A from metakaolin (800^{o}C for 3hours). From the XRD pattern, the characteristic peaks of zeolite A prepared with concentration 1M and 3M NaOH crystallized at 90^{o}C for 72hours agreed with the peaks of commercial zeolite A (Treacy and Higgins 2001). However, maximum cystallinity was obtained with 3M NaOH 70% and increasing concentration did not increase the crystallinty of the synthesized zeolite because maximum crystal growth was expected to have been attained (Lijalem *et al.,* 2015 and Janijira, 2002). The SEM images of zeolite A synthesized at 3M NaOH showed a typical cubic shaped crystals as was similarly observed by Holmes et al (2011).

Effect of Crystallization Temperature

Crystallization temperature has been used to to study growth, optimtize yield and alter morphology as earlier mention. Increase in crystallization temperature will increase the nucleation rate, the crystal growth and the morphology of the cystals. The synthesis of zeolite A was screened from crystallization temperature of 90 to 110^{o}C as reported by Rayalu *et al*., (2000). Zeolite A formation increased with increase in crystallization temperature as evident from the increase in the intensity diffraction peaks from XRD pattern of $AC4_2$ which were similar to those of commercial zeolite A.

Effect of Crystallization Time

Crystallization of zeolites increased with time as earlier stated. This was observed in AC3 and $AC4_3$ whose

crystallinity increased with time. The crystallinity of the AC4 products was a measure of how different AC4 product was obtained. The crytallization time of 24 h used in this work resulted in the synthesis of poorly crystalline. The low crystallinity might be a result of nucleation from the competiting precursors of the aluminosilicate gel which resulted in poor crystal growth. When the crystallization time was increased to 72 h, the crystallinity of $AC4_1$, $AC4_3$ and $AC4_4$ dramatically increased to between 63-66 %. The increased time of crystallization created an opportunity to obtain sucessful nucleation process closely followed by the crystal growth. A prolong crystallization time can lead to dissollution of zeolite A into sodalite phase when synthesized in alkaline aluminosilicate gel (Novembre *et al.,* 2011). An increase in time allowed the alkalinity content of gel to cause increase in solubility of silicate and aluminate ions leading to enhanced polycondensation reaction between the polysilicate and aluminate.

3.5 Application of the Synthesized Zeolite A in Water Softening

Water softening was carried out using sample AC3 because it has the highest crystallinity. The analysis of the hard water (local well water) showed that it had calcium concentration of 48.0 ppm. The effect of time was studied using 50 mg of synthesized AC3 zeolite sample to treat 20ml of the hardwater. The effect of time over the removal of calcium ion from hardwater by synthesized zeolites is shown in Figure 6.

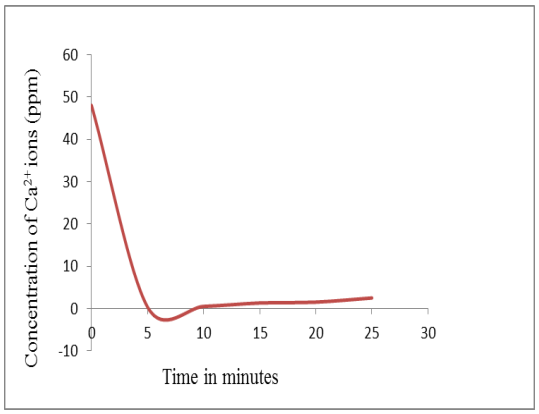

Figure 6: Water Softening Using AC3

The concentration of Ca^{2+} reduced from 48ppm to 0.3ppm within 5 minutes of treatment with AC3, corresponds to 99.4% softening, as confirmed in the work of Loiola *et al.,*(2012). However, an increase in the concentration of Ca^{2+} ions was observed after 5minutes ranging from 0.5 to 2.5 ppm which appeared as a maximum in the graph plotted. These may be as a result of prolonged treatment time as softening of hardwater using zeolite is achieved through the percolation of the hardwater sample through bed of zeolite at specific rate. Loiola *et al.,* (2012) were able to create hardness in water using a solution of calcium chloride. The hardwater prepared has a lot of calcium ions that were introduced by the solution of calcium chlorides. Loiola *et al.,* (2012) treated the hardwater for over 30 mins without observing a return of Ca^{2+} ion in the water because the water was not at its stable state and it had excess Ca^{2+} to exchange for sodium ions. The water used in this work was moderately hard and in its stable condition. The calcium ions that was taken off by the synthesized zeolite made it unstable. Treating the hard water with zeolite AC3 for more than 5 mins was an indication of the return of some calcium ions into the water as the water tended to regain its stability. Crystallinity of synthesized zeolite is very vital in water softening. Zeolite AC3 with the highest Crystallinity was able to remove about 100% hardness with 5 mins.

4.0 CONCLUSIONS

The synthesis of zeolite A was successfully carried out using Aloji kaolin. The kaolin was refined by sedimentation process and metakaolin was achieved by thermal treatment of refined kaolin at 800^{o}C for 3 h. The optimal conditions for synthesis of zeolite A from Aloji Kaolin using a conventional hydrothermal route were: concentration of base solution of 3M, crystallization time of 72hours and crystallization temperature of 90^{o}C after aging the reaction mixture for 24 h. The optimal conditions resulted in the synthesis of zeolite A with high crystallinity of 70%. The SEM images revealed a pure cubic shape typical of commercial zeolite A and XRD pattern revealed a characteristic diffraction peaks of commercial zeolite A. Base on the results of water softening test, zeolite A synthesized from Aloji Kaolin showed tremendous potential as above 98% calcium ions were removed from the hard water within 5 mins of treatment at room temperature.

REFERENCES

Alkan, M., Hopa, C., Yilmaz, Z., and Guler, H. (2005) The effect of alkali concentration and solid/liquid ratio on the hydrothermal synthesis of zeolite NaA from natural kaolinite, Micropor. Mesopor. Mater., Vol. 86, pp.176-184.

Bekkum V.H., Flanigen, E.M., Jacob, P.A., Jansen, `J.C. (1991) Introduction to |zeolite science and practice. 2nd Revised edition, Elsevier Amsterdam.

De Lucas, A., Uguina, M.A., Covian, I., Rodriguez, L., (1992) Synthesis of 13X zeolite from calcined kaolins and sodium silicate for use in detergents. Industrial & Engineering Chemistry Research, 31(9): p. 2134-2140.

Guglielmo Ventura and Lara Risegari (26 November 2007). The Art of Cryogenics: Low-Temperature Experimental Techniques. Surendra kumar. Pp 17- ISBN 978-0-08-044479-6 Retrieved 4 June 2012.

Heller-Kallai and Lapides I. (2007) Reaction of kaolinites and metakaolinites with NaOH –comparism of different samples (Part 1). Applied Clay Science, 35, 99-107.

Jana Dypayan (2007) "Clinoptilolite – a promising pozzolan in concrete (PDF). A New Look at an old Pozzolan.
29th ICMA conference. Quebec City. Canada: construction materials consultants. Inc. Retrieved 7 October 2013.

Jing-Quan Wang, Ya-Xi Huang, Yuanming Pan and Jin-Xiao Mi (2014) Hydrothermal synthesis of high purity zeolite A from natural kaolin without calination. Microporous and Mesoporous Materials 199: 50-56

Janijira Wongwiwattana, (2002). Synthesis and Kinetic Study of Zeolite Na-A from Thai Kaolin. Master of Science in Chemistry Thesis Suranaree University of Technology.

Loiola, A.R., Andrade, J.C.R.A., Sasaki, J.M., and Da Silva, L.R.D. (2012) Structural analysis of zeolite NaA synthesized by a cost-effective hydrothermal method using kaolin and its use as water softener. Journal of Colloid and Interface Science. 367: 34-39

Lijalim Ayele, Joaquim Perez – pariente, Yonas chebude, Isabel Diaz. (2015) Synthesis of zeolite A from Ethiopian Kaolin. Journal of Microporous and Mesoporous Material 215:29-36.

Meier, W. M., Baerlocher, C., and Olson, D. H. (1996). Atlas of zeolite structure types. International zeolite Association. Elsevier. 130-189

Musyoka, N. M. (2009) Hydrothermal synthesis and optimisation of zeolite Na-P1 from South African coal fly ash. MSc Thesis, University of the Western Cape.

Machado, N.R.C.F., Mitto D.M.M (2012) Synthesis of Na-A and X zeolite from bagasse fly ash, microporous and mesoporous material 162: 6-13

Mostafa, A. A., Youssef. H. F., Sorour. M. H., Tewfir, S. R. and Shalaan. H. F., (2011) Utilization of Egyptian kaolin for Zeolite A. Preparation and performance Evaluation. 2nd International Conference on Environmental Science and Technology IPCBEE vol. 6 (2011) (c) 2011 IACSIT Press, Singapore.

Novembre, D., Sabatino B.D.I., Gimeno, D., Pace C. (2011) Synthesis and characterization of Na-X, Na-A and NaP zeolites and hydroxysodalite from metakaolinite, clay minerals 46: 339-354.

Nakagawa, M., Yoshikura, S., Miura, S., Fukuda, T., Harada, A. (2006) Kaolin deposit at Melthonnakkal and Pallipuram within Trivandrum block southern India Gondwana Research 9: p. 530-538

Purnomo, C.W., Salim C. and Hinode, H. (2012) Synthesis of Na-A and Na-X zeolite from bagasse fly ash, Microporous and Mesoporous Materials 162: 6-13

Rayalu, S. S., Udhoji, J. S., Meshram, S. U., Naidu R. R., Devotta S., (2005) Estimation of crystallinity in fly ashbased zeolite-A using XRD and IR spectroscopy, Current Science, 89, p.2147-2151

Stuart M. Holmes, Abdulaziz A. Alomair and Abdul S. Kovo (2012), The direct synthesis of pure zeolite-A using virgin' Kaolin, RSC Advances, 2012, 2, 11491–11494, www.rsc.org/advances

Salam, Hawawu (2015) Comparative studies on Techniques of Synthesis of Zeolites A and Y from Kaolin and their Ion Exchange Behaviour. Master Degree Thesis, Department of Chemical Engineering, Federal University of Technology, Minna.

Tanaka, A. and Fujii, A. (2009) Effect of stirring on the dissolution of coal fly ash and synthesis of pure from Na-A and Na-X zeolite by two-step process. Advanced Powder Technology 20:473-479.

Wajima, T., Haga, M., kuzawa, K., Ishimoto., H. Tamada, O., Ito, K., Nishiyama, T., Downs, R.T., Rakovan, J.F. (2006) Zeolite synthesis from paper sludge ash at low temperature (90°C) with addition of diatomite, Journal of Hazardous Material 132: 244-252.

Xu, R., Pang, W., Yu, J., Huo, Q. And Chen, J. (2007) Chemistry of zeolite and related porous material; synthesis and structure, clement loop Singapore John Wiley 676.

Yunan Ma, Chunjie Yan, Aref Alshameri, Xiumei Qui, Chungu Zhou, Danli (2014) Synthesis and characterization of 13x zeolite from low grade natural Kaolin. Advanced powder Technology. Elsevier.

UTILISATION OF LOCAL KAOLIN AS CATALYST SUPPORT IN THE PRODUCTION OF CARBON NANOTUBES USING CATALYTIC VAPOUR DEPOSITION METHOD

Abdulkareem A. S[1,2,*], Suleiman B[1], Kariim I[2], Onimisi I[1], Kovo A.S[1] and Mohammed I.A[2]

[1]Chemical Engineering Department, Federal University of Technology, PMB 65, Bosso, Minna, Niger State

[2]Nanotechnology Research Group, Centre for Genetic Engineering and Biotechnology, Federal University of Technology, PMB 65 Bosso, Minna, Niger State

Corresponding author: kasaka2003@futminna.edu.ng Phone: +2347068482432

ABSTRACT

The work focused on the use of kaolin as support material for the development of Fe/Kaolin monometallic catalyst for multi-walled carbon nanotubes synthesis (MWCNTs) in catalytic vapour deposition equipment. The influence of process parameters such as drying temperature, drying time, stirring speed and mass of support on the percentage yield of monometallic Fe/Kaolin catalyst using wet impregnation method was further reported using a factorial experimental approach. The optimum yield of 79.40 % was obtained at a drying temperature of 120 ^oC, drying time of 5 hours, stirring speed of 7 rpm, and 9 g mass of support during the optimization of the process parameters. The highest yield catalyst was then characterized for surface area, morphology, functional group, and crystallinity using BET, SEM/EDX, FTIR and XRD respectively. The well characterized catalyst was further used for the synthesis of MWCNTs in a CVD reactor and the effect of acetylene flow rate on the MWCNTs yield was recorded. It was found that the flow rate of acetylene was directly proportional to the MWCNTs yield. The synthesized MWCNTs possessed excellent morphology and surface area. Hence, the applied kaolin support showed high proficiency for possible application as catalyst support for synthesize of good quality MWCNTs in a CVD reactor.

Keywords*: kaolin, wet impregnation, optimization, characterization, MWCNTs and CVD*

1.0 INTRODUCTION

The discovery that materials can exist in their nano scale and still maintain most of its properties stimulated many researchers around the world to begin the production of smaller, lighter, faster, and cheaper devices which possess greater functionality (Xi *et al.*, 2006). Nanoparticles, due to their smaller size and large surface to volume ratio, exhibit interesting novel properties which include nonlinear optical behavior, increased mechanical strength, enhanced diffusivity, high specific heat, magnetic behavior and electric resistivity, (Kavecký *et al.*, 2015). Though, syntheses of various nanoparticles such as gold nanoparticles, silver nanoparticles and carbon nanoparticles have been reported in literature (Afolabi et al., 2007), this present study focus on the synthesis of carbon nanotubes (CNTS).

CNTs are cylinder-shaped macromolecules having a radius as small as a few nanometers, which can be grown up to 20 cm in length. The walls of these tubes are made up of a hexagonal lattice of carbon atoms analogous to the atomic planes of graphite. They are capped at their ends by one half of a fullerene-like molecule (Guo *et al*., 1995). It has been reported that laser ablation, arc discharge and catalytic vapour deposition methods are the three main methods of CNTs production, however catalytic vapour deposition (CVD) method has been described as the viable route of CNTs production in commercial quantities and qualities (Teo *et al.*, 2004; and Kariim *et al.*, 2015). Despite the robust nature of CVD for CNTs production, it has been reported that lack of understanding of CNT growth mechanism has caused hindrance in the production of CNT with well-defined properties (Kumar, 2012). This necessitated the need to study the several parameters such as the catalyst preparation method, type of metal and support to be used, synthesis route to be applied and type of carbon source (Kumar, 2012). Among all the factors listed, catalyst and its support play a major role in the production of CNTs which brought about the need for detail study of the effects of catalyst support on the yield and qualities of CNTs produced by CVD method. Even though several support materials such as $CaCO_3$, Al_2O_3, SiO_2 and Zeolite have been reported in literature (Afolabi et al., 2007; Iyuke et al., 2007), there is little information on the utilization of kaolin as a catalyst support for CNTs growth. It is on this basis that

this present study is focused on the development of monometallic (Fe) catalyst with Kaolin support material.

2.0 MATERIAL

The chemicals and gas used in this study were of analytical grade and they include Iron (III) nitrate Nona hydrate (98.5% purity), argon gas (99.9% purity) and acetylene (99.9% purity). Kaolin used in this study was obtained in Lagos, while the distilled water was obtained from Centre for Genetic and Biotechnology, Federal University of Technology, Minna, Niger State, Nigeria.

2.1 Catalyst Preparation

Preparation of catalyst involves wet impregnation of iron salt on kaolin support and the influence of the process of impregnation on the yield of the catalyst was investigated using 2^4 factorial experimental designs. This implies that four factors were studied at two (low and upper) levels as shown in Table 1. A calculated amount (4.65g) of Iron (III) nitrate Nona hydrate salt was dissolved in 50ml of distilled water and shaken to form homogeneous solution. A given quantity of kaolin (lower level - 8g and upper level - 9g) was added to the mixture and stirred at a known stirring speed of 400 rpm and 700rpm respectively for lower and upper level for a period of twenty minutes. The slurry obtained was then oven-dried at a selected temperature of 110^{o}Cand 120^{o}C respectively for lower and upper level. The drying of the sample obtained was done in an oven for a pe riod of 5 hours and 7 hours respectively for the lower and upper level. The sample obtained was then allowed to cool at room temperature, grinded to avoid particle agglomeration and screened through 50 µm. The screened sample was then calcined at temperature of 500^{o}C for a period of 14 hours. The yield of the catalyst obtained was then calculated using the Equation 1. The detailed experimental combination obtained from the design expert with the yield of catalyst as the output is as presented in Table 2.

$$yield(\%) = \frac{mass\ of\ catalyst\ after\ calcination}{mass\ after\ oven\ drying} \times 100 \quad (1)$$

The sample that gave the best yield was analyzed using TGA, SEM/EDX, XRD, FTIR and BET to respectively determine the thermal stability, morphology, crystallinity and surface area. FTIR was also used to determine the type of bond present in the catalyst developed.

Table 1: Level of Factors for Catalyst Synthesis

	Mass of support (g)	Stirring speed (rpm)	Drying temp. (^{O}C)	Drying time (hr)
Upper (+) Level	9	700	120	7
Lower (-) level	8	400	110	5

2.2 Carbon Nanotubes Synthesis

The Fe/Kaolin composite catalyst developed was then utilized in the production of Carbon Nanotubes in Catalytic Vapour Deposition (CVD) Reactor with acetylene as the carbon source. The CVD reactor used in this study was made of a quartz tube (52 mm internal diameter, 4 mm thickness and 1010 mm length), placed in a furnace that has heating capacity of 1200^{O}C. Gas cylinders for the carbon source (acetylene) and the carrier gas (Argon) were connected to the inlet of the reactor which had flow meters to control the gas flow. The control system of the CVD allows for an appropriate temperature program in maintaining consistent and appropriate heating rate, reaction temperature, and cooling rate. The exhaust gases through an exhaust pump at the reactor outlet were collected by bubbling in water. A known weight (1.0 g) of the monometallic Fe catalyst on kaolin support was placed in the ceramic boat, which was inserted in the horizontal quartz tube of the CVD furnace. The production temperature was kept constant at 750^{o}C while the production time was varied between 20 to 60 minutes with step increment of 10 minutes. The furnace was set to the required temperature of 750^{o}C during which argon was allowed to flow over the catalyst at a flow rate of 30ml/min this is for the purpose of purging the system of the air that might have been trapped in the reactor during the process of placing the catalyst inside the reactor. When the system attained the set temperature of 750^{O}C, the argon flow rate was adjusted to 100 ml/min and acetylene was introduced into the system at the required flow rate of 20, 30, 40, 50, 60 ml/min for a period of 40 minutes. After which the flow of acetylene was stopped and the flow rate of argon was reduced to 30ml/min to cool the furnace to room temperature. The boat that contained the black soot was then removed and weighed to determine the quantity of CNTs produced. Percentage of CNTs produced was determined using Equation 2 (Lee *et al.*, 2009).

$$CNTs\ yield\ (\%) = 100\ \% \times \frac{MTotal - MCatalyst}{MCatalyst}$$

Where, MTotal = the total mass of the catalyst and carbon products after CVD reaction process;
MCatalyst = initial mass of Fe/kaolin catalyst.
The CNTs produced were characterized with SEM/EDX, TEM, XRD and BET to determine their morphology, nature, crystallinity/crystallite size and surface area respectively.

3.0 RESULTS AND DISCUSSION

3.1 Kaolin Characterization

Results obtained showed that the raw kaolin had a specific surface area of 98.79 m^2/g, pore volume of 0.08857cc/g and a pore size of 0.3102 nm. These properties showed that raw kaolin is a micro-porous material with an order of a few molecular diameter of the inter-molar distance (Hendrik *et al.* 2011). Thermal stability analysis of the raw kaolin was also conducted; the results obtained revealed that the kaolin sample was thermally stable up to a temperature of 800^oC with less than 15% lost in weight as shown in Figure 1. This is an indication that the kaolin sample will be thermally suitable as catalyst support for the production of CNTs.
Presented in Figure 2 is the SEM micrograph of kaolin, which showed that it was plate-like in nature with irregular particle shapes containing compartments of aluminosilicate. The micrograph also showed that the particles of raw kaolin were well defined with porosity that were related to the spaces between agglomerates, the presence of this agglomerates as well as large particle size defined the density of this material.

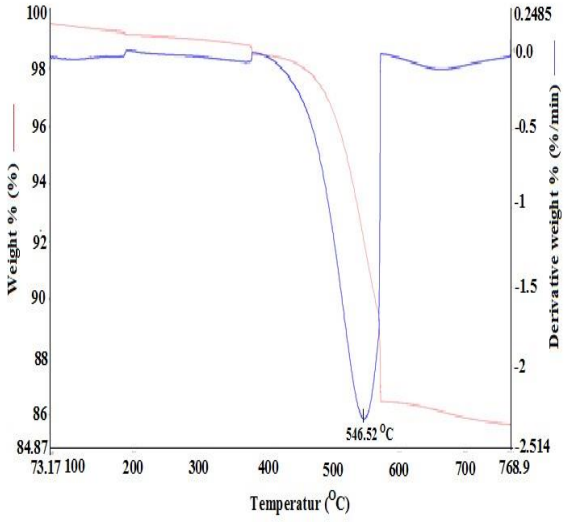

Figure 1: TGA/DTG Thermograph of Kaolin support

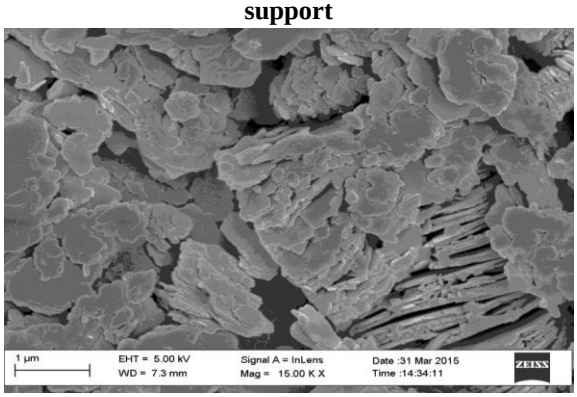

Figure 2: HRSEM Micrograph of kaolin sample

3.2 Catalyst Preparation

The effects of operating condition such as mass of support (kaolin), stirring speed, drying time and drying temperature on the yield of monometallic Fe/kaolin were presented in Table 2 using 2^4 factorial design of experiments. The optimum catalyst yield of 79.4 % was obtained at a drying temperature of 120^oC, drying time of 5 hours, stirring speed of 7 rpm, and 9 g mass of support.

Table 2: Influence of Operating Parameters on the Yield of Catalyst

Run order	Mass of support (g)	Stirring Speed (rpm)	Drying Time (hrs)	Drying Temperature (^oC)	Yield (%)
1.	8	400	5	110	77.8
2.	9	400	5	110	77.21
3.	8	700	5	110	76.74
4.	9	700	5	110	77.23
5.	8	400	7	110	77.69
6.	9	400	7	110	76.61
7.	8	700	7	110	77.84
8.	9	700	7	110	78.01
9.	8	400	5	120	75.47
10.	9	400	5	120	77.23
11.	8	700	5	120	77.28
12.	9	700	5	120	77.43
13.	8	400	7	120	77.62
14.	9	400	7	120	78.49
15.	8	700	7	120	78.60
16.	9	700	7	120	79.46

The yields of catalyst were used to carry out factorial design analysis, this involved the analysis of variance (ANOVA) to create theoretical model for the main and combined effect on yield after calcination. The equation for estimating yield in terms of significant factors is presented as follows (Equation 3):

$$\%\,Yield = +77.47 + 0.53(mass\ of\ support) + 0.33(stirring\ speed) + 0.35(drying\ time) - 0.37(stirring\ speed \times drying\ time \times drying\ temperature) \quad (3)$$

The highest yield of Fe/Kaolin produced at the optimum yield was characterized for surface morphology, elemental analysis, surface area, surface functional group and crystallinity. Figure 3 depicts the HRSEM micrograph of the catalyst sample.

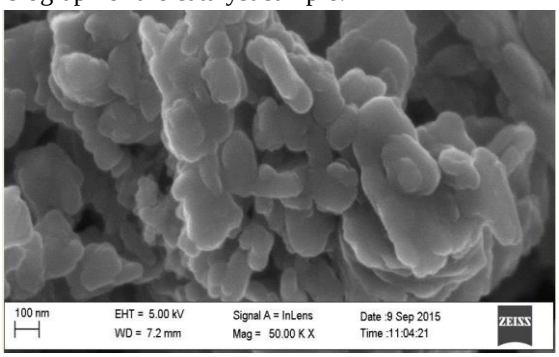

Figure 3: HRSEM Micrograph of Fe/Kaolin Catalyst

Results presented in Figure 3 showed that the catalyst is nearly spherical in geometry with the formation of agglomerate which can be linked to the formation of oxide on the surface and pores of the kaolin sample. Also, proper dispersion of the metal on the support material was achieved as shown by the presence of small pores within the composite as seen from Figure 3 compared to the starting kaolinite clay. Figure 4 showed the EDS spectral of the catalyst sample.

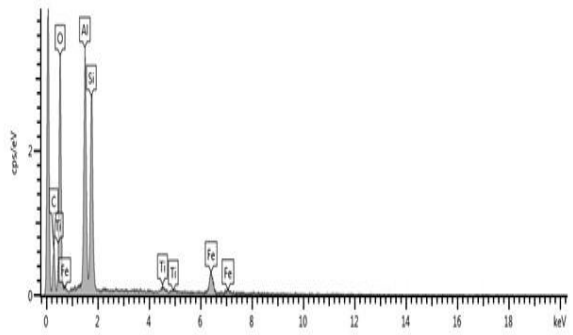

Figure 4: EDS Spectral of Fe/Kaolin Catalyst

Figure 4 showed the EDS spectrum which confirmed the presence of Fe, C, O, Al, Si and Ti chemical components in different proportions in the catalyst matrix. The observation of element such as Fe at lower energy level showed that it could be present in the oxide form.

Brunauer-Emmett-Teller (BET) analysis was used to determine the surface area, pore radius, pore volume and pore size of the catalyst. Table 3 showed the summary of the BET data of the catalyst sample obtained in a Nitrogen environment. The obtained characteristics depicted in Table 3 showed that the developed catalyst was of high and good crystallinity with pores classified as nicropores according to IUPAC nomenclature. This revealed that the catalyst produced possessed adequate textural properties that will allow the diffusion of carbon sources into the catalyst pores for CNTs growth

Table 3: Summary of BET Results of Developed Fe/Kaolin

Properties	Catalyst
Surface area (single point) (m^2/g)	119.2
Pore volume (DR method micropore volume) (cc/g)	0.07407
Pore size (DR method micropore half pore width) (nm)	0.3091

The X-ray diffraction method was used to analyze the crystalline size and texture of the catalyst sample (Figure 5). The detailed identification of the phase presence in the bulk of the Fe/Kaolin catalyst was shown in Figure 5. The estimated particle size showed that Fe/kaolin catalyst with particles in nanometer range can be produced under appropriate synthesis conditions (Kariim et al., 2015 and Iyuke et al., 2007).

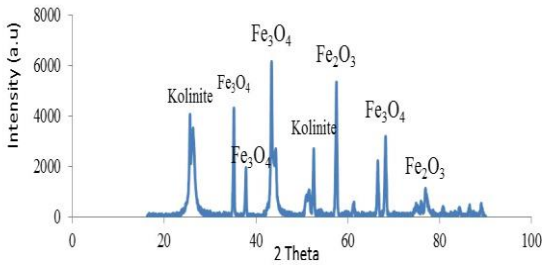

Figure 5: XRD Pattern of Fe/kaolin Catalyst Showing Peak Values

The average crystallite size of the catalyst was found to be 35.27 nm using DeBye-Scherrer Relationship (Equation 4).

$$D = \frac{K\lambda}{\beta cos\theta} \quad (4)$$

Where D is the particle size diameter, β is the full width at half maximum, θ is the diffraction angle, λ is wave length of X-ray (0.1541 nm) and K is Scherer constant (0.94). Fourier Transform Infrared Spectroscopy Analysis, FTIR (Figure 6) was used for identifying the surface functional group present on the prepared Fe/kaolin monometallic catalyst.

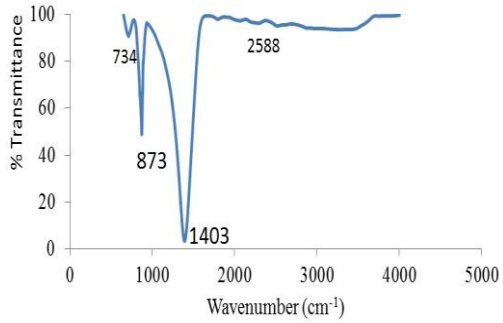

Figure 6: FTIR Spectral of Fe/Kaolin Catalyst

Figure 6 revealed the presence of several peaks with different functional groups; the observed wavenumber at 734 cm^{-1} corresponded to the O-Al-O symmetric bending vibration, the band wavelength at 873 cm^{-1} was assigned to the region of OH with Fe, while the adsorption band at 2588 cm^{-1} was attributed to OH bending hydration (Aliyu, 2016).

3.3 CNTs Production

The well characterized Fe/Kaolin was used for the synthesis of carbon nanotubes in a CVD reactor. During the latter process, the effect of acetylene flow on the percentage yield of CNTs was examined at constant argon flow rate (100mL/min), reaction temperature (750 ^{o}C) and deposition time (40 mins). Table 4 showed the results of the effect of acetylene flow rate.

Table 4: Effect of Acetylene Flow Rate on the Percentage Yield of CNTs

Runs	Acetylene flow rate (ml/min)	Mass of CNT produced (g)
1	20	0.02
2	30	0.19
3	40	0.37
4	50	0.43
5	60	0.53

From Table 4, the effect of acetylene flow rate on the percentage yield of CNTs has been observed to exhibit direct proportionality relationship. This shows that as the flow rate of the carbon source increases, more of the carbon from the source is introduced into the reactor for deposition on the catalyst surface (Kariim et al., 2015). The highest yield CNTs obtained at the flow rate of 60 mL/min was characterized for surface area, functional group, crystallinity, morphology, and EDS for elemental composition.

The BET results of the produced CNTs were as follows: specific surface area = 299.167 m^2/g, specific pore volume = 0.01106 cc/g and pore size = 0.3171 nm. These characteristics showed that the CNTs have potential as adsorbent materials for wastewater purification and in catalysis (Afolabi et al., 2007). Figure 7 showed the surface morphology of the synthesized carbon nanotubes.

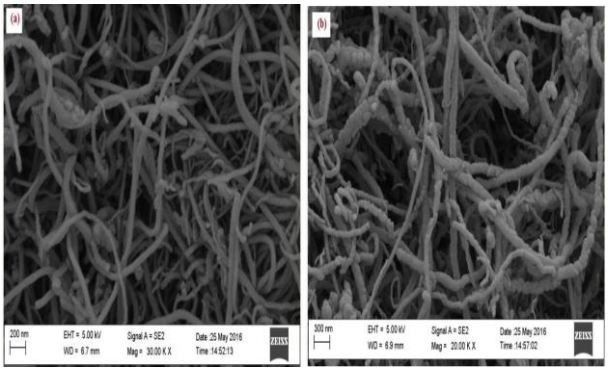

Figure 7: HRSEM of CNTs for (a) High Yield and (b) Low Yield CNTs

Figure 7 a and b showed clearly that the structural morphology of the synthesized CNTs varied. In Figure 7a high yield CNTs depicted densely populated strands of CNTs with little or low level of branched tubes compared to the low yield carbon nanotubes. Thus, it was revealed that low flow rate favored the synthesis of branched and irregular CNTs formation. The EDS analysis resulted in useful information on the elements present in the CNTs in terms of percentage composition. The results of the EDS analysis were shown in Figure 8.

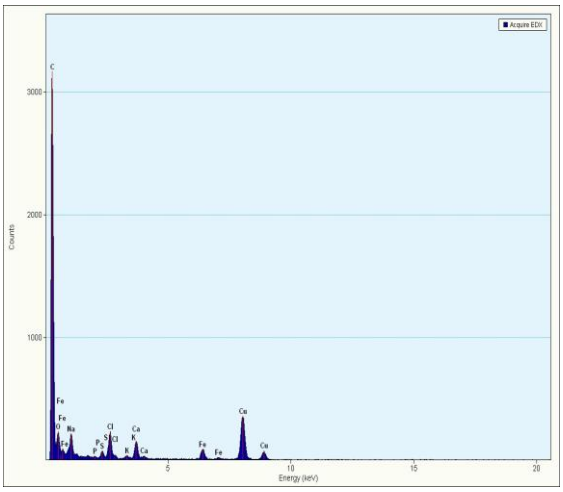

Figure 8: EDS Spectral of theSynthesized CNTs of the Highest Yield of Produced CNTs.

The EDS data showed the presence of high amount of C and other impurities resulting from the kaolinite clay used as support material.

The X-Ray diffraction technique was used to investigate the crystallinity of the CNTs produced. Figure 9 showed the XRD pattern of the produced CNTs for varying conditions for runs 1-5(Acetylene flow rate of 20-60ml/min with step increment of 10ml/min) as depicted in Table 4. The characteristics peaks of the graphitized carbon were depicted in Figure 9 at 2 theta of 25.14 and 44.73 ^{o} in all the CNTs samples produced. The presence of diffraction peaks was an indication of the iron oxides introduced by the catalyst material as an impurity, which must be removed to promotes the utilization of CNTs for various industrial applications (Kariim et al., 2015).

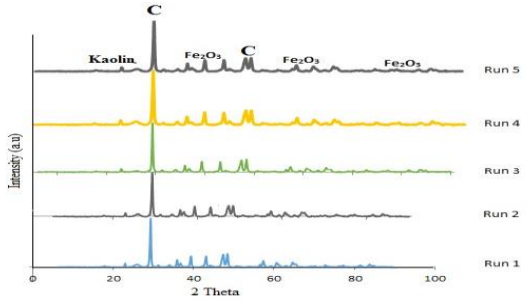

Figure 9: XRD Spectral of the Synthesized CNTs at Various Acetylene Flow Rates.

Furthermore, the surface functional group present in the synthesized CNTs was further characterized using the FTIR technique (Figure 10).

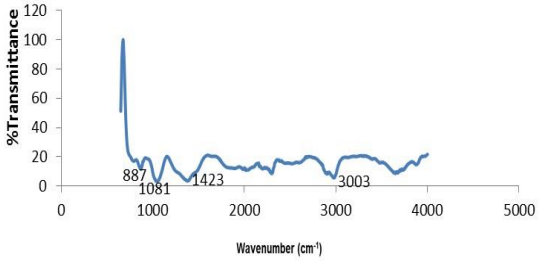

Figure 10: FTIR Spectral of synthesized highest yield CNTs

From Figure 10, the peak with wavenumber 887 cm^{-1} showed the presence of O-H bond with Fe. The peak of 1081 cm^{-1} wavenumber was the characteristic regions representing the C-O stretch and that of 1423 cm^{-1} and 3003 cm^{-1} were assigned to the C-H bends and stretches in the bulk of the CNTs sample respectively. Figure 11 represented the internal morphology of the highest yield of the synthesized CNTs.

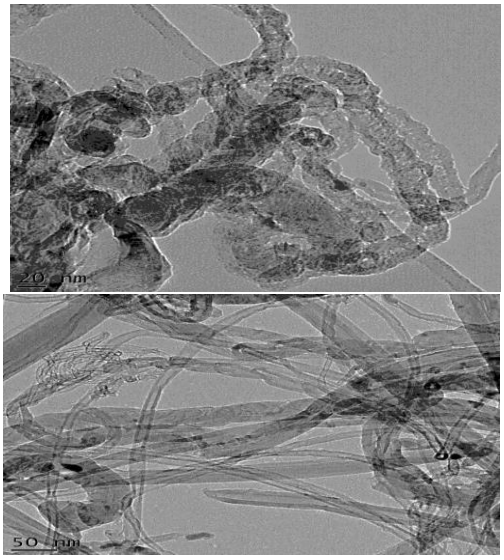

Figure 11: HRTEM Micrograph of the Synthesized CNTs.

The Figure 11 showed the internal structural makeup of the developed CNTs. It was found that the CNTs produced MWCNTs with series of concentric tubes of varied diameter. The presence of encapsulated catalyst particles in the tubes of the CNTs was depicted by the blackishly dense spots in Figure 11.

5.0 CONCLUSION

The study addressed the suitability of locally sourced kaolin as a support material for the development of monometallic catalyst for the synthesis of high quality MWCNTs in a CVD reactor. The optimum yield of 79.40 % was obtained at a drying temperature of 120 ^{o}C, drying time of 5 hours, stirring speed of 7 rpm, and 9 g mass of support during the optimization of the process parameters. Wet impregnation methods employed showed a high level of catalyst dispersion for high efficiency. Thus, the TEM images of the synthesized CNTs showed that the nanomaterial produced was MWCNTs with irregular diameter. The study further showed that the flow rate of acetylene was directly proportional to the percentage yield of the MWCNTs in a CVD reactor. Hence, the application of kaolin as a support material showed high suitability level for the development of monometallic Fe/Kaolin for the synthesis of MWCNTs.

Acknowledgement

Authors appreciate the financial assistance received from TETFund Nigeria under the grant number TETF/DESS/FUTM2016/STI/Vol 1 and also the Center for Genetic Engineering and Biotechnology, FUT Minna, Nigeria for using their facilities.

REFERENCES

Afolabi, A. S., Abdulkareem, A. S. & Iyuke, S. E. (2007). Synthesis of carbon nanotubes and nanoballs by swirled floating catalyst chemical vapour deposition method, Journal of Experimental Nanoscience 2(4): 269-277.

Guo, T., Nikolaev, P., Rinzler, A. G., Tomanek, D., Colbert, D. E., and Smalley, R. E. "Self-Assembly of Tubular Fullerenes", J. Phys. Chem., 99 (1995) 10694-10697.

Iyuke, S.E., Abdulkareem, A. S., Afolabi, A. S. & Piennar, C. H. vZ. (2007). Catalytic production of carbon nanotubes in a swirled fluid chemical vapour deposition reactor, International Journal of Chemical Reactor Engineering 5(Note S5):1-9

.

Kariim I., Abdulkareem A.S., Abubakre O.K., Mohammed I.A., Bankole M.T., Jimoh T.O. (2015). Studies on the suitability of alumina as bimetallic catalyst support for MWCNTs growth in a CVD reactor. International Engineering Conference (IEC2015); 09/2015 .

Kavecký S., Valúchova J., Čaplovičová M., Heissler S., Šajgalík P., Janek M. (2015). Nontronites as catalyst for synthesis of carbon nanotubes by catalytic chemical vapour deposition. Applied Clay Science, 114: 170-178.

Kumar, M. and Ando, Y., (2012) "Chemical Vapor Deposition of Carbon Nanotubes: A Review on Growth Mechanism and Mass Production", Journal of Nanoscience and Nanotechnology Vol. 10, 3739–3758.

Motchelaho A.M.M. 2011. Iron And Cobalt Catalysts Supported on Carbon Nanotubes For Use In The FischerTropsch Synthesis. A thesis submitted to the Faculty of Engineering and the Built Environment, University of the Witwatersrand, Johannesburg, in fulfillment of the requirements for the degree of Doctor of Philosophy, Johannesburg,:http://wiredspace.wits.ac.za/bitstream/handle/10539/11208/PhD%20Thesis-2011-Anne%20Myriam%20Megne%20Motchelaho.pdf?sequence=2

Teo, K.B.K.; Singh, Ch.; Chhowalla, M.; Milne, W.I. Catalytic synthesis of carbon nanotubes and nanofibers. In Encyclopedia of Nanoscience and Nanotechnology; Nalwa, H.S., Ed.; American Scientific Publisher: Valencia, CA, USA; Volume 1, pp. 665–668, 2003.

Xi S, Ci L, Tang D, Yan X, Li Y, Liu Z, Zou X, Zhou W and Wang G (2006), Chem. Phys. Lett. 349, 191–195.

COMPARATIVE SYNTHESIS OF SODIUM SILICATE FROM RICE HUSK AND KAOLIN

Ajayi, O. A.[a], Mamman, J[a] and Adefila, S.S[b]
[a] Department of Chemical Engineering, Ahmadu Bello University, Zaria. Kaduna State. Nigeria
[b]Engineering Environmental Management Services, Suite 5 1st Floor, Plot 1469, Ahmadu Bello Way, Garki, FCT Corresponding author: segeaj@gmail.com and aoajayi@abu.edu.ng

Abstract
Sodium silicate in powdered form was successfully synthesized from both rice husk ash and Kankara kaolinite clay.
The crystallinity of sodium silicate produced tends to increase with reaction time, temperature, and Na_2O/SiO_2 ratio. About 93% crystallinity for as-synthesized sodium silicate was obtained using Na_2O/SiO_2 molar ratio of 0.9, reaction time and temperature of 75mins and 100^0C, respectively. The starting material and product formed were characterized using XRF, XRD and SEM analysis. The result proved that the sodium silicate produced can serve as an excellent replacement to its commercial counterpart.

Keywords: Kankara kaolin, deploymerization, rice husk ash, sodium silicate

1.0 INTRODUCTION

Sodium silicate is a critical raw material for many consumer chemical processes as well as monomer for many consumer and commercial products including corrosion inhibitor, anti-scaling agent, viscosity adjustor and zeolites, just to mention but few. Sodium silicate is commonly prepared via reaction in liquid phase or in solid phase, using alkaline and quartz as raw materials (Schimmel et. al, 1993; Chakraverty et. al, 1988). In liquid phase, mixture of caustic soda, quartz sand and steam is feed into a reactor and allowed to react following equation (1).

$$nSiO_2 + 2NaOH \rightarrow Na_2O.nSiO_2 + H_2O \quad (1)$$

The solid phase involves reaction between either sodium sulphate or sodium carbonate and quartz at very high temperature (between 900^0C and 600^0C) in molten state to form sodium silicate as depicted by equations (2) and (3).

$$Na_2CO_3 + SiO_2 \rightarrow Na_2O\,(SiO_2) + CO_2.$$
$$2Na_2SO_4 + C + 2SiO_2 \rightarrow 2Na_2O\,(SiO_2) + 2SO_2 + CO_2. \quad (3).$$

This process of manufacturing sodium silicate, depicted in equations 2 and 3, is considered expensive due to the high energy required at the calcination stage (above 1000^0C), in addition to considerable air pollution by emission of dust, nitrogen and sulphur oxides (Christophliemk et al., 1988; Chungsangunsit et al., 2009). Although this calcination process is widely used in industrial scale, there is another process based on the reaction of amorphous silica (am-SiO_2) with NaOH (Brenn et al., 2000).

Kalapathy et al. (2000) reported the successful production of flexible sodium silicate films from rice husk ash.
Cha and Park (2001) also reported the successful synthesis of sodium silicate from clay from Sancheong-Hadong, Korea via alkaline leaching at 25-100^0C under atmospheric pressure. Ayegba et. al., (2015) reported the successful production of silica gel from clay and claimed that the yield depends on the reaction time and alkaline concentration.

Icenhower and Dove (2000) established the fact that the dissolution of amorphous silica (am-SiO_2) is a function of the temperature and the concentration of simple electrolyte solutions. The solubility of am-SiO_2 is relatively low at pH 7, with reported values ranging from 100 - 130 ppm at 25^0C. However, the solubility increased dramatically above pH 9. The number of silicate anions present rose as Si concentration was increased, while pH and/or temperature decreased (Tester et al., 1994; Knauss and Wolerry, 1988; House and Orr, 1992; Brady and Walther, 1990).

Silicon dioxide (SiO_2), also known as silica, is prevalent within diverse marine and terrestrial environments and

comprises a significant fraction of the Earth's crust. It is the oxygen bridge bonds between silicon atoms that give SiO_2 many of its unique properties.

The bond angle Si-O-Si is nominally about 145 degrees, but can vary from about 100 to 170 degrees with very little change in bond energy. It's this structure that gives silica its stability and rigidity toward depolymerisation, a major setback in energy minimization in sodium silicate production Greenberg, 1957; Casey et al., 1990).

Nigeria is richly blessed with kaolin amounting to about two (2) billion metric tons' deposit scattered all round the country (Ajayi, 2012). The clay of kaolinite nature contains both alumina, silica and other associated impurities depending on source location. For effective removal of alumina from clay, calcination is a critical step for kaolin activation and enhanced digestibility of alumina, followed by acid leaching for longer contact time of reaction. At the same time, Nigeria is also a high consumer of rice products. Obassi and Ajoku (2007) reported an annual national paddy rice production of 3.32 million tons amounting to about 664, 000 tons of rice husk generated per year. The disposal of rice hulls is a substantial problem for rice growers, since the hulls are not suitable for use as fertilizers and until now have to be disposed of either by open burning or burying. When burnt in an uncontrolled manner, the ash which is essentially silica is converted into crystalline forms and becomes less reactive (Chandrasekhar et al., 2006).

Accordingly, we sought to make use of the silica resulting from acid-treated kaolin and rice husk ash for sodium silicate production, while comparing the quantity and quality of the as-synthesized products from both sources.

2.0 MATERIALS AND METHODS

2.1 Materials

The rice husk was obtained from a local market in Zaria, Kaduna State, kaolin from Kankara village, Katsina State. The NaOH and H_2SO_4 were of analytical grade, obtained from local vendors, having purity of 50% and 96%, respectively. The distill water used was prepared in our laboratory (Department of Chemical Engineering, Ahmadu Bello University, Zaria).

2.2 Methods

Rice husk pre-treatment

Rice husk was soaked for 4 days in tap water to remove stones and dirt and then dried under atmospheric condition. The rice husk was then soaked in 10 w/w % sulfuric acid, boiled at 85^0C for 1 hour, then allowed to steep for 24 hours in the acid solution as explained in Ajayi et al., (2013). The acid treated rice husk was thoroughly washed, until pH=7 was reached and then dried at 100^oC for seven (7) hours, in an oven.

Charring and Calcination of the Husk

The pre-treated rice husk was charred in the open furnace for two hours at 200^oC. The rice husk was charred to ensure it does not smoke during calcination in the furnace. The charred rice husk, black in colour was transferred to the muffled furnace where it was calcined at 500 ^{0}C for 6 hours Ajayi et al., (2013) . The rice husk ash (RHA), white in colour was then ball milled for 4 hours to obtain fine particles size below 53μm.

Beneficiation of Kankara Kaolin

Raw Kankara kaolin was soaked in tap water in a plastic bucket and the slurry was allowed to stand for three (3) days. During the three days, it was periodically stirred and fresh water added after decanting the supernatant water every 12 hours. This was done to get rid of soluble impurities in the clay mineral and grits amongst others. The slurry was sieved to get rid of coarse particles with a 53 μm mesh sieve. The fine suspension thus obtained was allowed to settle and the supernatant water decanted. The sediment was dried at atmospheric condition, followed by oven drying at 100^oC for 12 hours. The product from this stage was referred to as Beneficiated Kaolin.

Calcination and Dealumination Process

The dry beneficiated kaolin powder was placed in crucibles after grinding and calcined in a muffled furnace at 750^0C for 6 hours to obtain metakaolin - a more reactive phase of kaolin (Ajayi, 2012). 20 g of metakaolin was measured into a conical flask and 20 cm^3 of distilled water was added to it. 16.8 cm^3 of 98 w/w % sulfuric acid (3 folds stoichiometric requirement) was measured and then added to the metakaolin slurry in the conical flask and the reaction was left for about 35 minutes on a heating mantle, after which additional distilled water was then added to quench the reaction. This time ensured complete dealumination of metakaolin. The reaction mixture was then filtered through the sinter glass filter, after washing to neutrality.

Synthesis of Sodium Silicate

32.5 cm^3 of water was poured into a beaker containing 1.3g of NaOH to make 1M NaOH solution. The dealuminated kaolin and rice husk were placed in a beaker containing 1M NaOH solution and left to age for

14 hours at 35^{0}C. The resulting slurry was made to react at 100^{0}C for 90 mins. After which the reaction was quenched with distilled water and washed to neutrality. This was later dried in the atmosphere and then in an oven, set at 140^{0}C for 24 hours.
The resulting sodium silicate produced from both rice husk ash and kaolinite clay was compared with commercial one using X-ray Diffractometer (XRD), to establish the desirable source of silica for further investigation. Kaolinite clay was chosen for further considerations while investigating the effects of alkalinity, reaction times and temperatures.

An estimated amount of NaOH was mixed with the dealuminated sample to obtain Na_2O/SiO_2 molar ratio ranging between 0.7 and 0.9. The resulting mixture was homogenized left to age for 4hrs at 35^{0}C, prior to reaction at 90^{0}C and 60mins. At this stage, the best Na_2O/SiO_2 molar ratio was established, while the other factors, namely, reaction time (45-75mins) and temperature (70-100^{0}C) were determined following OVAT method of experimentation. The water quantity used was kept constant for all the experimentation.

3.0 RESULTS AND DISCUSSION

Treatment of RHA and Kankara Kaolin

The analysis was to ascertain what was achieved during rice husk pre-treatment, charring, and kaolin beneficiation, as detailed under methodology. The analytical method employed is a well-established means of compositional analysis using X-ray fluorescence (XRF).

Table 1: Compositional Analysis of Samples

Oxides	Percentage Composition (weight %)				
	Raw Kankara Kaolin	Ben. Kaolin	Deal. Kaolin	Raw Rice Husk	Rice Husk Ash
SiO_2	58.300	53.1	91.7	48.8	95.1
Al_2O_3	43.2	42.750	*ND	5.0	*ND
Na_2O	0.120	0.074	*ND	0.16	*ND
SO_3	0.189	0.185	0.68	8.75	0.05
Fe_2O_3	3.160	1.320	0.212	3.23	0.162
CaO	0.150	0.113	0.441	3.23	0.287
K_2O	1.260	0.981	1.87	10.2	0.092
ZnO	0.176	0.175	0.313	0.10	0.01
PbO	0.043	0.042	ND	1.30	0.99
MnO	0.09	0.019	0.01	0.679	0.044
Si/Al (mol %)	2.29	2.11			

*ND-Not detected

The compositional analysis of the raw kaolin depicted in the second column of Table 1 indicated significant amount of oxides of potassium, iron, titanium and magnesium which were considered to be impurities. The silica/alumina ratio of kaolin was calculated as 2.29, which was an indication of the crystallinity state and purity level of the kaolin.

Beneficiation process shifted silica/alumina ratio towards 2, by reducing the free silica, which was removed through dissolution or floatation. The silica to alumina ratio of beneficiated kaolin calculated from data obtained from Table 1 gave a value of 2.11 and comparing with silica to alumina ratio of raw Kankara clay indicated a decrease in the silica to alumina ratio. The alumina content was noticed to increase proportionally to the removal of impurities. Impurities such as potassium oxide and iron oxide were observed to reduce owing to beneficiation.
Table 1 showed that inorganic content of the rice husk had a high amount of silica (95.1%) and a few impurities which can be attributed to the nature of soil, the rice was cultivated on. The silica content was observed to increase tremendously with treatment. Dealuminated samples was observed to have 91.7% silica (as shown in Table 1) pointing to removal of alumina-enrichment in term of silica. The increase in other oxides was attributed to the water used for quenching and washing. The silica content of dealuminated Kaolin was 91.7%, which was also high when compared to the rice husk ash, the sodium silicate synthesized was compared on this premise.

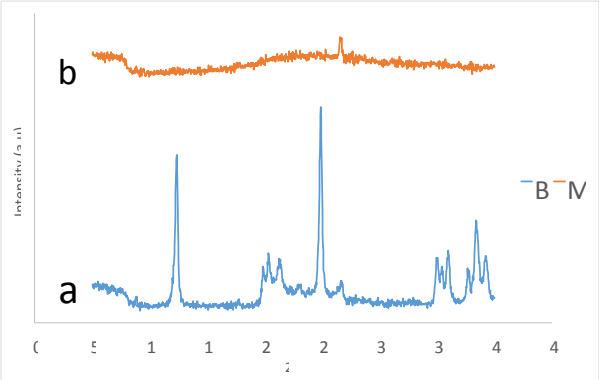

Fig. 1: XRD Analysis Kankara Kaolin

Figure 1(a) showed that the clay possessed all the necessary characteristic peaks attributed to kaolinite material. Upon heating, these peaks were observed to disappear leading to formation of semi-amorphous metakaolin, as depicted in Figure 1(b).

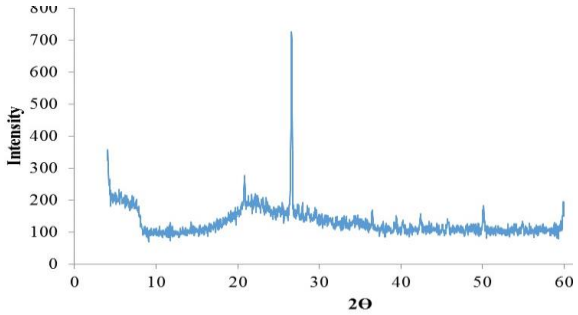

Fig 2: XRD Analysis for RHA Calcined at 500^{o}C

Figure 2 showed the diffractogram for rice husk ash. The peaks at 2Θ of around 26 showed the formation of silica which when compared with that of the husk (diffratograph not shown) tended to be sharper (Ikram and Akhtar, 1988). The appearance of this peak suggested the effect of thermal treatment of the rich husk, which also corroborated the findings from XRF and (Scanning Electron Micrograph) SEM.

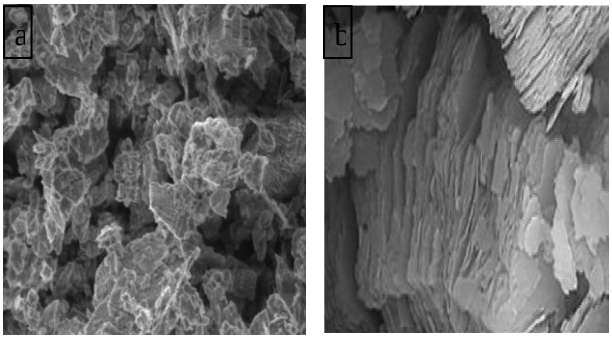

Figure 3: SEM Images for (a) Raw Kaolin (b) Beneficiated Kaolin

Figure 3a depicted the SEM for raw Kankara Kaolin showing aside the silica-alumina card-like pattern, with the rod-like halloysite material and dark spot responsible for accommodating both water molecules and cellulosic materials. Beneficiation was able to handle some of the water soluble impurities as well as the free uncombined phases, as shown in Figure 3b.

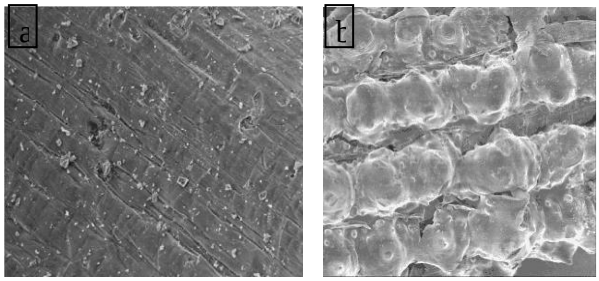

Figure 4. SEM Images for (a) Raw Rice Husk (b) Rice Husk Ash

The SEM image in Figure 4a showed that the surface structure of the raw rice husk was intact and smooth, while that of the husk (figure 4b) appeared to be exposed and uneven with cracks. This distruption might have been caused by the effect of acid treatment followed by calcination, thereby rendering the rice husk ash more amorphous.

Synthesis of Sodium Silicate

The diffractograms in Figures 5a and b were similar for silica from both rice husk ash and Kankara kaolin respectively, providing a ground for comparison of products formed from the two sources. The diffractograms indicated the presence of silica in predominantly amorphous form. The broad peak observed around 2Θ value of 26^{0}C in both cases was characteristic of opaline silica. The intensity of the peak at 26^{0}C was the same, but there were more peaks in the XRD for rice husk than in Kaolin, indicating that the silica from Kankara kaolin was slightly more amorphous and therefore expected to be more reactive.

The prominent peaks used to identify sodium silicate were at 2θ position of 16.8^{o}, 25.0^{o} and 29.3^{o}. The XRD patterns for as-synthesized sodium silicate from rice husk and Kankara kaolin in Figure 6 gave all the characteristic sodium silicate' peak when compared with diffractogram of commercial sodium silicate, indicating its purity viz-a-viz crystallinity.

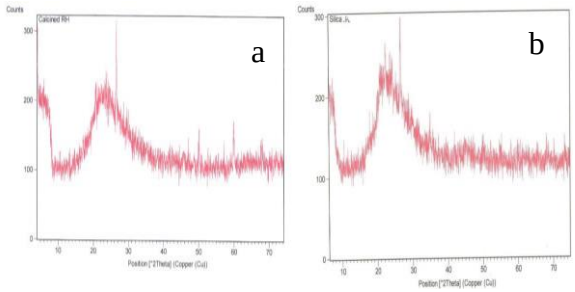

Figure 5: XRD Patterns for Silica from (a) Rice Husk Ash and (b) Kankara Kaolin

Figure 6 showed some bumps (scattered pattern) in the XRD pattern of sodium silicate from RHA and commercial sodium silicate which might suggest an amount of amorphousity. The aforementioned statement revealed that sodium silicate from kaolin might be more crystalline than that from RHA, due to the level of amorphousity notice for the former in Figure 5a and b. Consequently, Sodium silicate from kaolin was therefore used for the characterization.

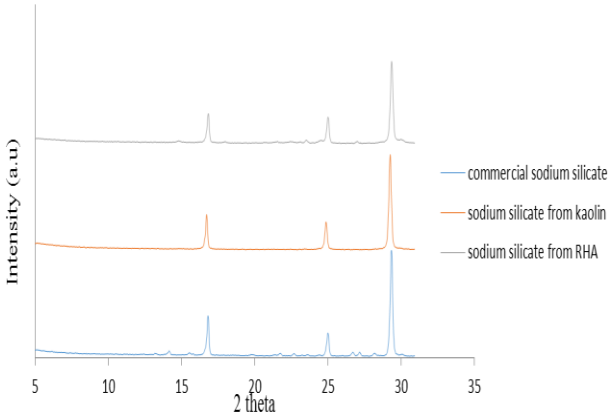

Figure 6. XRD of Sodium Silicate from Commercial, Kaolin and Rice Husk Ash

The rate of conversion of inherent silica in both RHA and kaolin was compared from a preliminary investigation. In line with the observations made from XRD for the silica and sodium silicate, kaolin tended to have a higher conversion (Figure 7).

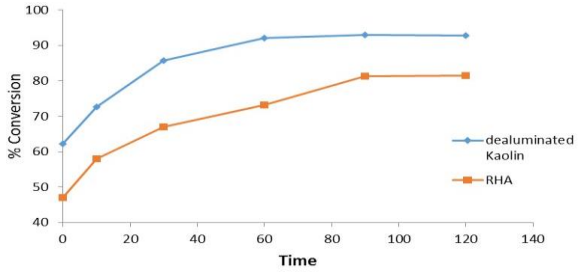

Figure 7: Sodium Silicate Conversion (%) for Kaolin and Rice Husk Ash Sources

Effect of NaOH Concentration

The absence of quartz peak in the diffractographs of synthesized sodium silicates with Na_2O-SiO_2 of 0.7 (S0.7), Na_2O-SiO_2 of 0.8 (S0.8) Na_2O-SiO_2 of 0.9 (S0.9) indicated that all the quartz was attacked and destroyed by sodium hydroxide solution (Figure 8). The NaOH added acted on the silica during both the ageing and reaction time resulting in the disappearance of the peak attributed to silica phase at 2θ = 26. The most prominent peak for sodium silicate was at 2θ = 29 degree and any further scanning resulted in low peak, hence our decision to stop at 2 theta value of 30.

The peaks in sample S0.7 is a little broad when compared to others, this suggested that it was due to insufficient NaOH in the sample needed to complete the reaction. Note that RSS denotes the commercial sodium silicate.

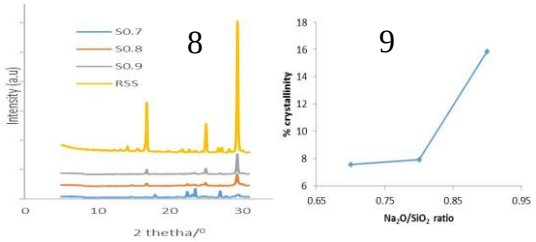

Figure 8: XRD for Sodium Silicate at various Na_2O/SiO_2 at 90^{0}C.

Figure 9. Crystallinity for sodium silicate at various Na_2O/SiO_2 at 90 C.

Percent crystallinity as obtained by X-ray measurements was defined as the ratio of intensity from the crystalline peaks of the commercial sodium silicate to the sum of the crystalline and amorphous intensities of the as-synthesized sodium silicate. The crystallinity was observed to increase as the NaOH concentration in the sample increased (Figure 9), which can be used to ascertain the extent of silica depolymerization.

Effect of Reaction Temperature

The sharp, clearly defined peaks indicated the crystalline structure (Figure 10). The XRD pattern for sample S70 (70^{0}C) did not exhibit the characteristic peaks attributed to sodium silicate. The peak at 22.82 indicated the presence of quarts, which might suggest that the temperature of 70^{0}C was inadequate for supplying the requisite heat of reaction for depolymerisation of quartz hence the failure in synthesis of sodium silicate at 70^{0}C. When the temperature was increased to 85^{0}C (sample S85) a drastic changed was observed in the diffractogram-peaks of sodium silicate began to emerge. Synthesis at 100^{0}C (S100) resulted in more crystalline sodium silicate. Comparing the XRD pattern for the various samples with that of commercial sodium silicate it was evident that intensity of peaks increased with increasing temperature (Figure 10).

In the crystallinity curve (Figure 11) it would be observed that, there was a sharp increase in the crystallinity with a small increase in temperature and gradual increase from 85^{0}C to 100^{0}C. This indicated that as the temperature of reaction between silica and sodium hydroxide increased, the solubility of the silicate also increased, thereby allowing for better crystallization of the targeted product.

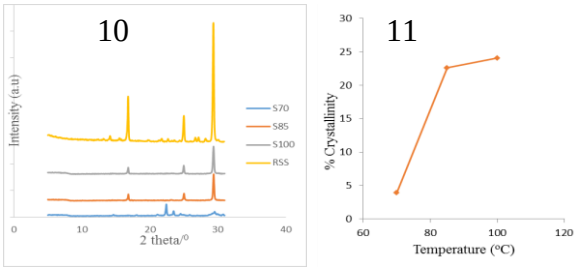

Figure 10: XRD of Sodium Silicate Syntesized at Different Temperatures for 35 minutess using Na_2O/SiO_2 of 0.85

Figure 11: Crystallinity of Sodium Silicate with Reaction Temperature

Effect of Time of Reaction

Comparing the various XRD patterns of the samples with RSS which was for commercial sodium silicate it was conspicuous that sodium silicate was formed at all the three conditions (Figure 12). For sample subjected to reaction time of 45min, at 2θ position of 22.8 the peak was attributed to the presence of quartz. This meant that, the reaction time of 45 minutes was not sufficed for the quartz particles to dissolve in sodium hydroxide solution prior to chemical reaction. At 60 minutes, this peak was not present in the XRD graph, meaning 60 minutes was sufficient for the depolymerisation of quartz present in the silica.

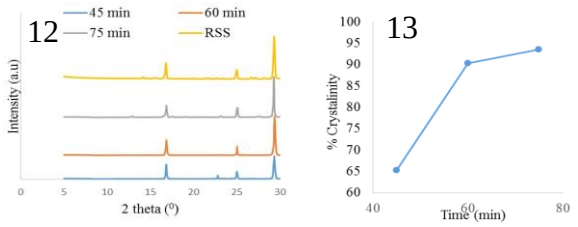

Figure 12: XRD of sodium silicate synthesized at ^{0}C and Na_2O/SiO_2 of 0.9

Figure 13: Crystallinity of Sodium Si Reaction Time various reaction times for100

licate with

The crystallinity of the as-synthesized product tends to increase as the reaction time as depicted by Figure 13. This suggested that reaction contact time played a significant role in sodium silicate crystallization reaction.

CONCLUSIONS

Rice husk ash was a very good source of silicate with higher percentage composition of silica than it was present in Kankara Kaolin, but showed lower crystallinity when compared to sodium silicate obtained from Kankara Kaolin. Sodium silicate in solid form was successfully synthesized from both sources. The crystallinity for sodium silicate calculated from XRD based on the peaks from the commercial product increased with increase in NaOH concentration, reaction time and temperature. Within the experimental range considered in this work, about 93% crystallinity was arrived at, when the Na2O/SiO2 ratio, reaction time and temperature were 0.9, 75mins and 100^{0}C, respectively.

REFERENCES

1. Schimmel G, Kotzian M, Panter H, Tapper A. *Process for producing amorphous sodium silicate*. United States Patent; 1993. nº 5,229,095.
2. Chakraverty, A., Mishra, P., and Banerjee, H. D. (1988). Investigation of combustion of raw and acidleached rice husk for production of pure amorphous white silica. *Journal of Materials Science*, *23*(1), 2124.
3. Christophliemk P, Novotny R, von Laufenberg J. *Hydrothermal production of clear sodium silicate solutions*. United States Patent; 1988. nº 4,770,866.
4. Chungsangunsit, T., Gheewala, S. H., and Patumsawad, S. (2009). Emission assessment of rice husk combustion for power production. *World Academics of Science, Engineering and Technology*, *53*, 1070-5.
5. Brenn, U., Ernst, H., Freude, D., Herrmann, R., Jähnig, R., Karge, H. G., and Schwieger, W. (2000). Synthesis and characterization of the layered sodium silicate ilerite. *Microporous and mesoporous materials*, *40*(1), 43-52.
6. Kalapathy, U., Proctor, A., and Shultz, J. (2000). Production and Properties of flexible sodium silicate films from rice hull ash silica. *Bioresource technology*, 72(3), 99-106.
7. Cha, M. S., & Park, K. Y. (2001). Preparation of Sodium Silicate from Clay. *Journal of chemical engineering of Japan*, *34*(2), 232-235.
8. Ayegba, C. O., Makinde, T., Odigwa, P., & Orijajogun, J. (2015). Production of Silica Gel from Clay. *International Journal of Materials and Chemistry*, *5*(6), 123-126.
9. Icenhower, J. P., and Dove, P. M. (2000). The dissolution kinetics of amorphous silica into sodium chloride solutions: effects of temperature and ionic strength. *Geochimica et Cosmochimica Acta*, *64*(24), 4193-4203.
10. Tester, J. W., Worley, W. G., Robinson, B. A., Grigsby, C. O., and Feerer, J. L. (1994). Correlating quartz dissolution kinetics in pure water from 25 to 625 C.*Geochimica et Cosmochimica Acta*, *58*(11), 2407-2420.

11. Knauss, K. G., and Wolery, T. J. (1988). The dissolution kinetics of quartz as a function of pH and time at 70 C. *Geochimica et Cosmochimica Acta*, *52*(1), 43-53.
12. House, W. A., and Orr, D. R. (1992). Investigation of the pH dependence of the kinetics of quartz dissolution at 25 C. *Journal of the Chemical Society, Faraday Transactions*, *88*(2), 233-241.
13. Brady, P. V., and Walther, J. V. (1990). Kinetics of quartz dissolution at low temperatures. *Chemical Geology*, *82*, 253-264.
14. Greenberg, S. A. (1957). The depolymerization of silica in sodium hydroxide solutions. *The Journal of Physical Chemistry*, *61*(7), 960-965.
15. Casey, W. H., Lasaga, A. C., and Gibbs, G. V. (1990). Mechanisms of silica dissolution as inferred from the kinetic isotope effect. *Geochimica et Cosmochimica Acta*, *54*(12), 3369-3378.
16. Ajayi, O.A (2012). Development of large pore zeolites from kaolinite clay. Ph.D Thesis, ABU, Zaria
17. Obasi E and Ajoku, K. B. (2007). Energy resource assessment of Agricultural (Rice Husk) waste in Nigeria. Country Study Report under UNIDO funded project.
18. Chandrasekhar S, Satyanarayana K, Pramada P and Majeed J. Effect of calcinations temperature and heating rate on the optical properties and reactivity of rice husk ash. *Journal of Materials Science* (Norwell), 2006; 41(1):7926-7933.
19. Ajayi, O.A, Aderemi B.O, Ahmed, A.S, Adefila, S.S, Ityokumbul, M.T (2013). Monitoring potassium in faujasite zeolite from Kankara Kaolinite clay. Paper presented at 42nd AGM for NSChE in Abuja
20. Ikram, N., Akhtar, M. (1988): X-ray Diffraction Analysis of Silicon Prepared from Rice Husk Ash, *Journal of Material Science and Technology*, 23(7): 2379-2381.

KINETICS AND THERMODYNAMIC STUDY OF BATCH ADSORPTION REMOVAL OF HEAVY METALS IN A SYNTHESIZED EFFLUENT USING RAW AND ALGINATE-FUNCTIONALISED SHEA HUSKS

M.D.Yahya[1], I.A.Mohammed-Dabo[2], A.S.Ahmed[2] and A.S Olawale[2]

[1]Department of Chemical Engineering, Federal University of Technology, Minna, P.M.B 65, Minna, Niger State, Nigeria.

[2]Ahmadu Bello University, Zaria, 810261, Nigeria.

Corresponding author e-mail: muibat.yahya@futminna.edu.ng

ABSTRACT

In this study, adsorption of synthesised solution lead (Pb^{2+}), copper (Cu^{2+}), cadmium (Cd^{2+}) and nickel (Ni^{2+}) onto raw shea butter husk (RSBH) and modified shea butter husk (MSBH) was investigated. Fourier Transform Infrared Spectroscopy (FT-IR), Scanning Electron Microscopy coupled with Energy Dispersive Aanalyzer (SEM-EDAX), and Brunauer-Emmett- Teller (BET) surface area analyzer were used for characterization of the adsorbents. FT-IR revealed that the –COOH-, -NH_2- and –OH- are the major functional groups responsible for the sorption. The SEMEDAX morphology indicated the presences of pores, cavities and the appearance of the metal ions after sorption. Batch adsorption study of the effect of contact time and kinetics of the sorption variations of the metal ions were analysed. Pseudo-second order equation gave $q_{e(calc.)}$ of amount adsorbed of 23.75 mg/g as against $q_{e(exp.)}$ of 23.96 mg/g on sorption of RSBH on Pb (II). Pb (II) recorded the highest percentage removal (90%) for all sorbents indicated. The highest amount adsorbed for most of the metal ions was achieved within a contact time of 5 minutes.

Thermodynamic parameters were evaluated and negative value of free Gibbs energy (ΔG^o) -80.37 and -1.146 KJ/mol-1 was obtained for RSBH-Cu and RSBH-Ni respectively, and (-23.56; -32.43 and -0.034) for all modified samples with exception of Ni (II). This revealed that the reactions were feasible and spontaneous.

1.0 INTRODUCTION

The recent advocacy on the agro-alimentary and solid mineral industry to be one of economic motor for sustainable development has brought about growth in the small and medium enterprises in these sectors. Mining industries form a large percentage of the small medium enterprise because of the feasibility of starting it in a growing economy like Nigeria. The blacksmith and miners are the major artisans involved in the processing of these natural substances. The ores of these minerals are heavily bonded with other compounds and the extraction processes are carried out in immediate environment or communities where their deposits are found. The result is that contamination of the soil, plants and water body occurs. These contaminants range from pathogens, heavy metals and suspended solids which have devastating effects on the environment.

Heavy metals are highly toxic to the environment and constitute serious health hazard to the ecosystem and man (Ahmad and Haydar, 2016). Johnson *et al*., 2008 categorized eleven (11) out of twenty (20) known heavy metals as hazardous. They are cadmium (Cd), selenium (Se), mercury (Hg), uranium (U), chromium (Cr), zinc (Zn), arsenic (As), lead (Pb), cobalt (Co), copper (Cu), and nickel (Ni). Smedley as cited in Podder and Majunder, (2016) reported that increase in heavy metals levels in the environment is due to both natural and anthropogenic sources; the natural sources include volcanic emissions, forest fires, and weathering reactions (Tchounwou *et al*., 2014). Ahalya *et al*. (2005) gave examples of anthropogenic sources as smelting of irons, mining, electroplating, leatherworking, sludge disposal and so on.

The presence of these metals in our environment has negative impact on human health; plants that are grown on this contaminated soil can accumulate the excesses of these metals and if consumed by man and animals can be transferred to them. Furthermore, they are toxic, non-biodegradable and persistent in nature (Larous *et al.* (2005). Recently, Nigeria recorded acute lead poisoning in as a result of mining activities in Zamfara

State in 2010 (Yahya *et al*., 2013) and Niger State in 2015. This was as result of mining activities in gold extraction. Plants, animals and man are affected through the bio-accumulation in the food chain. The effect of heavy metals poisoning is more pronounced on children and may include various health disorder such as blindness, paralysis, low IQ, seizures and even death (Grossman, 2012). Discharge of wastewater containing heavy metals into the ecosystem causes aesthetic pollution, eutrophication and perturbations to aquatic life (Gupta *et al*., 2011). Consequently, it is imperative to reduce these metal concentrations to low levels or completely remove them from waste effluents before discharge to the water bodies.

In other to effectively reduce the concentrations of these heavy metals, different technologies such as chemical precipitation (Nishimura and Umetsu 2001 as cited by Podder and Majumder, 2016), ion exchange (Figueiredo *et al*., 2016), filtration (Brandhuber and Amy 1998), reverse osmosis (Bhausaheb *et al*., 2011), electro dialysis techniques (Blanes *et al*., 2016) have been employed. However, these processes are expensive, and need high energy requirements. Sometimes generation of secondary sludge occurs, which also poses disposal challenges (Abdollahi *et al*., 2016). The possibility of developing low cost wastewater treatment materials from low cost agricultural waste materials has prompted a lot of researchers into biosorption techniques in recent times. (Benerjee *et al.*, 2012, Amirnia *et al*., 2016, Matin-lara *et al*., 2016). The use of agricultural by-products such as oil palm waste (Daud and Ali, 2004), cassava waste biomass (Horsfall and Abia, 2004) and defatted papaya seed (Gilbert *et al*., 2010) to mention a few, in wastewater treatment have also been reported. This study seeks to use an agricultural wastes matter (shea butter seed husk) for the removal of heavy metals such as cadmium, nickel, copper, and lead from synthetic wastewater using the batch modes of sorption. This differs from previous studies because of the modification using calcium alginate for enhanced sorptive sites and also simultaneous removals of other competing heavy metal ions. The kinetics and thermodynamic adsorption rate were evaluated as well.

2.0 MATERIALS AND METHODS

The stock solutions containing Cd, Cu, Pb and Ni were prepared by dissolving known masses of cadmium, copper, lead and zinc nitrate salt, $3CdSO_4 \cdot 8H_2O$, $CuCl_2.2H_2O$, $Pb(NO_3)_2$ and $NiCl_2.6H_2O$, respectively, in distilled water. All the reagents used for analysis were of analytical reagent grade. The metal concentration was analyzed by fast sequential Atomic Absorption Spectrometer (AAS) with auto sampler Varian SPS3, SpectrAA240 FS, (Varian, England).

Fresh shea butter fruits were collected between the month of July and August, from Gidan Kwanu farmland in Niger state, Nigeria. The fruits weighing approximately 1 kg were washed thoroughly with water followed by distilled water to remove impurities like dusts and inorganic matters from the surface. After washing, de-pulping was carried out to remove the fleshy mesocarp. This was followed by drying in an oven for 48 hrs at a temperature of 50 ^oC to reduce moisture content to as low as 6-7%. The drying process facilitated de-husking, which helped to remove the hard shell covering the endoderm containing the oil. The dried husks were crushed with a jaw crusher and sieved using an electrical sieve shaker to obtain a powder less than 250 µm particle sizes. The particles were then stored in polyethene bags for further use. This sample was called the raw shea butter husks (RSBH).

To prepare modified shea butter husk (MSBH), 1 g of sodium alginate was dissolved into 100 ml of distilled water kept on hotplate magnetic stirrer at a temperature of 65 ^oC (Fiol *et al.*, 2006). The dissolved jelly-like solution was continuously stirred at approximately 100 rpm until it was cooled down to room temperature (27 ±2 ^oC). A 2 % (w/v) composition of shea butter husk was chosen as it was found to be the most efficient for the encapsulation procedure (Fiol *et al*., 2003; Escudero, *et al*., 2006), was added into the jelly-like solution under an intense agitation at 150 rpm in order to produce homogeneous mixture of alginate and the husk particles. The mixture was carefully added drop wise through the nozzle of diameter 0.2 mm syringe into a solution of 0.1 M calcium chloride. The alginate chains in the mixture wrapped up the sorbents to form beads (Khorrambadi *et al*., 2011). The entrapped RSBH with the calcium alginate (CA) beads was cured in the $CaCl_2$ solution for 24 hours. The emerging hard spherical beads of 2 % (w/v) of RSBH now called modified shea butter husk (MSBH) were filtered and thoroughly rinsed with distilled water until the pH of the rinsed water is at neutral thus ensuring complete removal of excess Ca^{2+} ions and stored in a refrigerator at around 4 ^oC for further use.

2.1 Characterisation of The Adsorbents

Raw shea butter husks and cake were characterized for various properties. The functional groups of the raw sorbents were determined using the Fourier transform-infrared spectrophotometer (8400S Schimadzu, Japan). The surface morphology of the sorbent at the raw state and after adsorption was studied with high resolution

Scanning Electron Microscope. The BET tests for RSBH and the loaded metal ions (Cu II and Cd (II)) were done using the BET analyzer (NovaWin Quantachrome, 2013) for surface area and pore volume analysis.

2.2 Batch Adsorption Procedure

The measurement of metal ions uptake onto shea butter husks (RSBH) and modified shea butter husk (MSBH) were determined by batch adsorption technique using a multi-purpose flask shaker at a speed of 200 rpm and temperature of 303 ±1K (Akhtar *et al*., 2010) to obtain rate and equilibrium data (Lugo-Lugo *et al*., 2009).

2.3 Effect of contact time

The rate at which adsorption takes place is very important in equilibrium study as it determines the saturation point. The experimental runs were performed on each adsorbate at higher concentration of 250 mg/L. This was chosen in order to account for highly polluted effluents. 50 ml of the adsorbate solution was introduced into a flat bottom flask with capacity 250 ml containing 40 beads of the MSBH and 0.5 g for RSBH. These were agitated at approximate 200 rpm and filtered at fifteen minutes' time intervals (0-240 mins). The concentration in the liquid phase was analyzed using the atomic absorption spectrophotometer and sorption uptake and percentage removal calculated as:

$$q_e = (C_i - C_e)\frac{V}{N} \quad (3.1)$$

$$\%R = \frac{C_i - C_e}{C_i} \times 100 \quad (3.2)$$

where, q_e is the sorption capacity, (mg/g), V is the volume of the solution in liter (L) and N is the amount of beads or weight of adsorbent in (g) when the raw sample is used. % R is the percentage of the metal removed.

2.4 Effect of temperature

The effect of temperature on the sorption of metal ions unto the biosorbent was studied by measuring out 50 ml of the adsorbate solution into flask containing 40 beads of the MSBH or 0.5 g of RSBH. These were agitated for 120 minutes at a speed of approximately 200 rpm, 27 ^{o}C (300 K) and then filtered. The procedure was repeated at 40 ^{o}C (313 K), 50 ^{o}C (323 K) and 60 ^{o}C (333 K). The following thermodynamic parameters, namely, heat of adsorption, ΔH, entropy, ΔS and free Gibbs energy, ΔG for the adsorption process were obtained from the relation:

$$InK_C = -\frac{\Delta H^o}{RT} + \frac{\Delta S^o}{R} \quad (3.3)$$

and $$\Delta G^o = -RTInKc \quad (3.4)$$

A plot of $\ln K_c$ (q_e/C_e) versus 1/T (K) yielded an equation whose slope is ΔH and intercept is ΔS (Naiya *et al*., 2009), where, K_c is the equilibrium constant, R the universal gas constant (8.314 J/mol K); and T (K) the absolute temperature; q_e is sorption capacity (mg/g), while C_e is the equilibrium concentration (mg/L) in the solution.

3.0 RESULTS AND DISCUSSION

The BET surface area for RSBH was found to be 5.493 m^2/g. The BET surface area for the adsorbed metals (Cu (II) and Cd (II) however, decreased to 2.073 and 5.333 m^2/g. This was as a result of reduction in the pore area and volume after adsorption with the metal ions which indicated the coverage of the sorptive sites.

The IR spectra of Figure 4.1 showed that the RSBH possessed surface structures of absorption above 3000 cm^{-1} which suggested that they were unsaturated (contains C=C). Absorption was very low, below 1700 cm^{-1}. This showed that the compound was probably amide or carboxylate. There were additional moderate band in the range 1200-1000 cm^{-1} and 800-600 cm^{-1} which implied simple hydroxyl compound. The shifting of the band of the O-H (Phenol) at 1376.26 cm^{-1} for RSBH to above 1400 cm^{-1} of the loaded sample was attributed to OH (phenol) bonding. There was complete disappearance of the aliphatic nitro-compounds from the loaded sample which also indicated adsorption of the metal at 1510.31 cm^{-1} for RSBH. A shift in the sharp peak at 1635.69 cm^{-1} for RSBH and to tiny broad peaks at 1637.62 cm^{-1} for Pb- loaded (Figure 4.1 B) sorbent as an example can be attributed to the stretching of C=O corresponding to carbonyls, olefinic C=C stretching frequencies of hemicelluloses, lignin and amino groups (Bansal *et al.*, 2009). Emergence of new tiny broad bands on the modified sorbents at frequency from 3400 cm^{-1} to above 4600 cm^{-1} may be attributed to binding of –OH group with the polymeric alginate structure.

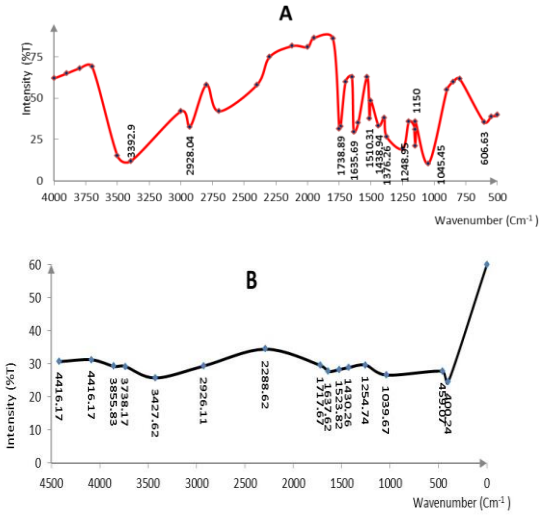

Figure 4.1: FT-IR Spectra of raw shea butter husk (A) and Pb-loaded sorbent (B)

The SEM micrographs at 1000x magnification for the MSBH (see Figure 4.2 A) clearly depicted the entrapped sorbents as shown by its white surface. Noticable were the entrapment of the husk within the alginate and the numerous pores for adsorption to take place.

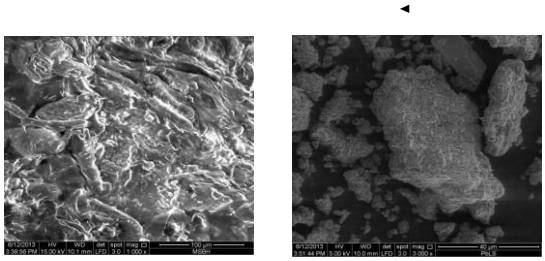

Figure 4.2: SEM micrographs of MSBH and PbLS at mag A (1000x); B (3000x)

The EDAX-spectrum for the metal ions after adsorption processes for the lead loaded sorbent (PbLS) is shown in Figure 4.2 B. The SEM micrographs (Figure 4.2 B) showed the presence of lead in the sorbent at 3000x while the EDAX (Figure 4.3) revealed the presence of Pb (II) after adsorption. The dense structure of the adsorbed lead can be vividly seen on the micrographs.

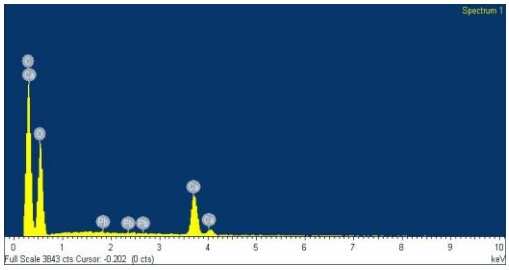

Figure 4.3: Spectrum of Lead loaded Sorbent (PbLS)

4.2 The effect of contact time

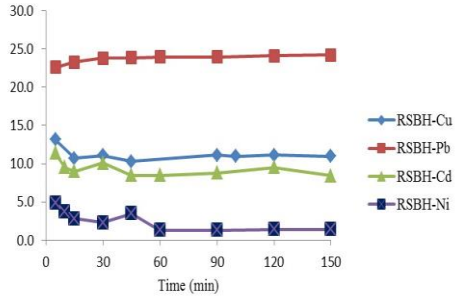

Figure 4.4: Amount Adsorbed of Pb (II), Cu (II), Cd (II) and Ni (II) by RSBH at varying Time (mass of sorbent=0.5 g, V_{sol}=50 ml, agitation speed 200 rpm, concentration 250 mg/L)

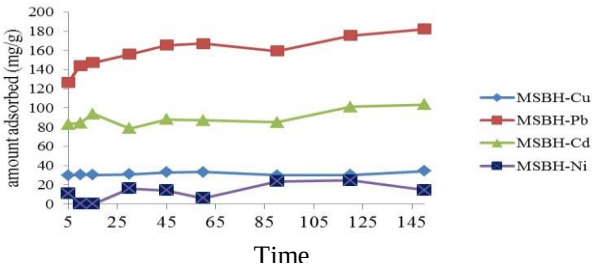

Figure 4.5: Adsorption Capacity of Heavy Metals by MSBH at different time intervals (no of

The amount of Cu (II) ions adsorbed by RSBH was found to be 13.13 mg/g within the first five (5) minutes of **MSBH=40 beads, V_{sol}=50ml, concentration, 250 mg/L)** agitation and these increased for Pb (II) to 22.59 mg/g at same time interval with the initial metal ion concentration kept constant at 250 mg/l. Correspondingly, Cd (II) amount adsorbed by RSBH was 11.40 mg/g with Ni (II) having 4.84 mg/g. (see Figure 4.4). It can be seen that the rate of metal ion removal was found to be very rapid within the first 5 minutes of agitation, thereafter, amount adsorbed becomes almost constant as time increased. No significant change in metal ion removal was observed after 30 minutes. The amount adsorbed for these metals were higher and faster at the beginning firstly because of the strong affinity the adsorbates have for the sorbent. Farinella *et al*. (2008) observed 5 minutes using grape bagasse for Cd (II) and Pb (II) adsorption which corresponded well with this adsorbent used. Secondly, the almost constant value achieved after 30 minutes of contact time with the RSBH was as a result of coverage of the sorptive sites and the impossibility of

the remaining vacant sites to be occupied due to the repulsive force between the adsorbates on the sorbent surface and the one in the bulk solution (Srivastava *et al*., 2006). On attachment of the metal ion onto the sorptive sites there was a gradual exhaustion of the capacity of the adsorbent.

The rapid metal ion removal at smaller time range showed significant economic importance in the scale-up process as this will facilitate the use of smaller quantity of sorbent to ensure maximum efficiency (Villaescusa *et al*., 2004).

The adsorption capacity of MSBH for the metal ions was remarkable. Notably on the plots was the arising of the plateau indicating exhaustion of the vacant sites. The amount adsorbed for all the metals ions was higher than the RSBH with MSBH-Pb having values from 126,41 mg/g at 5 minutes of contact to 175.49 mg/g after two (2) hours of vigorous shaking. These increments were recorded for the other metals too. There was relative stability in the adsorption capacities with increase in time and this may be attributed to the enhanced structure of the sorbent. Studies have shown that modification helped to reduce interference from the organic constituents due to their immobilization with calcium alginate. The alginate itself was porous as illustrated in the SEM analysis and thus improves efficiency of the adsorption process (Khorrambadi *et al*., 2011). Comparing the adsorption capacities amongst the metals, there were pronounced differences in the order Pb (II) > Cu (II)> Cd (II) >Ni (II). Several authors reported this behaviour (Haug 1965 as cited in Papageorgiou *et al*., 2006). These maybe attributed to their electronegativity of which Pb (II) was the highest. Their position was not clearly defined using this as Ni (II) which had the lowest adsorption capacity was more electronegative than Cu (II) and Cd (II). The stereo-chemical effects could also be a factor in the coordination of the oxygen atom surrounding the metal ions. The active sites on the sorbent contain oxygen atoms as indicated on the FT-IR results. These had been referred to as hard base from the Pearson's Hard Soft Acid theory (HSAB) and preferentially, this will react with hard acids (the metals in solution). Ni (II) in solution was not as acidic as compared to Pb (II) which was more acidic (Martînez *et al*., 2006). The important role that can be ascertained through the contribution of the alginate to the sorbent was the rigidity, stability and the conversion of the sorbent to bio-degradable substances because of its biological origin. All this were offered to the sorbent during adsorption (Khoo and Ting, 2001; Mata *et al*., 2009).

4.3 Kinetic studies

Kinetics studies of adsorption of various metals ions on the sorbents was correlated with the Pseudo-first-order, Pseudo-second-order and Weber-Morris equations. The experimental data were used to determine the rate controlling mechanism of the adsorption processes. Their conformity with model-predicted values was expressed by correlation coefficients (R^2) and the root mean square error (RMSE) determined.

4.4 Pseudo-first-order model

Kinetics study of the sorbents with the sorbates at varying time intervals and concentrations of 250 mg/L was varied. The R^2 values were in the range of 0.1526-0.6333 was low for the two sorbents while the RMSE were high in the range of 0.2522-1.6919 (see Table 4.1). The model which was based on diffusion process as the rate limiting sorption step was unable to describe the sorption process in the studied time range. The rate constant, k_1 is extremely low for most of the sorbents-sorbates process. Kosasih *et al*. (2011) stated that higher k_1 values resulted in shorter times for the system to reach equilibrium. As a result of this, calculated amount adsorbed, ($qe_{calc.}$) does not equal the experimental amount adsorbed (qe_{exp}). Studies such as Hansen *et al*. (2010) reported lower correlation coefficient in adsorption of Cu (II) onto agricultural waste; Ibrahim *et al.* (2010) also observed low correlation coefficient of Pb (II) sorption onto modified soda lignin.

Table 4.1: Pseudo-First-order Parameters of RSBH and MSBH

Sorbent	$q_{e(calc.)}$ (mg/g)	$q_{e(exp.)}$ (mg/g)	K (min^{-1})	R^2	RMSE
RSBH-Cu	2.2637	10.9796	-0.0027	0.2594	0.3435
RSBH-Pb	1.7783	23.9576	0.0014	0.1526	0.2522
RSBH-Cd	3.8289	10.0798	0.0023	0.0771	0.4665
RSBH-Ni	2.0177	1.3317	-0.0069	0.4926	0.3415
MSBH-Cu	7.6199	95.5733	-0.0142	0.2519	1.6919
MSBH-Pb	55.0337	182.6202	0.0127	0.6333	0.6643
MSBH-Cd	34.3022	106.8524	0.0153	0.7685	0.4922
MSBH-Ni	6.0142	16.1035	-0.0022	0.0358	0.8303

4.5 Pseudo-second-order model

The pseudo-second-order assumption as proposed by Ho *et al*., (2000) assumeed that biosorption was in two distinct phases; in the first phase reaction was usually very fast while in the second phase it took longer exposure time (Peretz and Cinteza as cited in Khorrambadi, *et al*., 2011). Majority of the sorbent-sorbate interaction followed this assumption with over 80 % having correlation above 0.9. The calculated q_e almost equals the experimental q_e. It was also observed that the initial sorption rate, *h* was higher for the modified sorbents than for the raw sorbents. This may be attributed to the calcium alginate used for entrapping the sorbents. Comparing the initial rate of sorption of each metal to the modified sorbents showed that Pb (II) was the highest (see Figure 4.6 & 4.7) followed by Cd (II) with the lowest to MSBH-Cu (II). Authors that have reported coefficient of correlation greater than 0.9 to mention a few were Wang *et al*., (2011) ; Çolak *et al*., (2011) ; Mahmood *et al*., (2011) on sorption of heavy metals on different adsorbents .

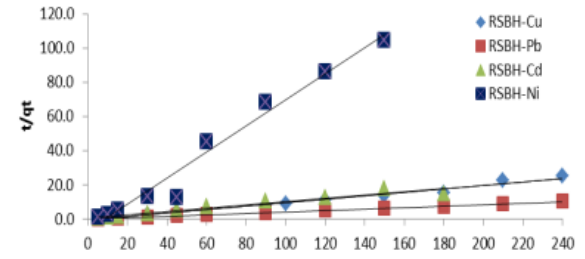

Figure 4.6: Pseudo-second-order plots of Pb (II), Cu (II), Cd (II), and Ni (II) adsorption by RSBH at 250 mg/l.

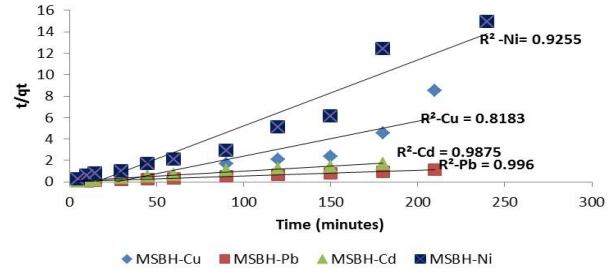

Figure 4.7: Pseudo Second-order Plots of Pb (II), Cu (II), Cd (II), and Ni (II) Adsorption by MSBH at 250 mg/L.

4.6 Weber-Morris Intraparticle Diffusion Model

Kinetic data for Pb (II), Cu (II) Cd (II) and Ni (II) were carried out on all the sorbents to test for this model. The sorption of these metals on MSBH can be seen on Figure 4.8. If the plots qt versus t^0.5 passed through the origin, then the intra-particle diffusion is the rate-limiting step during sorption processes, if it does not pass through the origin, it may be combination of several steps like the film diffusion with the pore diffusion or any of the steps enumerated (Weber, and Morris, 1963). The experimental data exhibited a multiple of linear plots meaning that more than one steps influenced the sorption process. This implied that the process occured in various stages as they all had a distinct y-intercept (Chen *et al*., 2013).

Table 4.2: Pseudo Second-order Parameters of RSBH and MSBH

Sorbent	$q_{e(calc.)}$ (mg/g)	$q_{e(exp.)}$ (mg/g)	k (g/mg.min)	h (mg/g.min)	R^2	RMSE
RSBH-Cu	9.8260	10.9796	-0.0159	-1.5305	0.9803	1.1046
RSBH-Pb	23.7474	23.9576	-0.0740	-41.7143	0.9994	0.0831
RSBH-Cd	10.3409	10.0798	0.0161	1.7215	0.9417	1.4142
RSBH-Ni	1.3132	1.3317	-0.0864	-0.1489	0.9734	6.1134
MSBH-Pb	185.7311	182.6202	0.0010	35.8492	0.9960	0.0236
MSBH-Cd	106.7330	106.8524	0.0013	14.3090	0.9875	0.0620
MSBH-Ni	16.2183	16.1035	-0.0041	-1.0766	0.9255	1.2998

The first portion was the diffusion of the metal ions to the film boundary of the sorbents (Ugurlu *et al*., 2005 as cited by Zulfikar *et al*., 2013). This indicated the thickness of the boundary layer when extrapolated to the y-axis as the intercepts (see the black arrows on the Fig 4.8). Higher intercepts implied higher boundary layer thickness (Laskhmi *et al*., 2009). This can be indicated for example with Pb (II) having the highest intercept of 22.59 while Ni (II) has the lowest of 4.84. The raw sorbents all had lower film diffusion with Ni (II) almost starting at the origin. Contrarily, the film diffusion stage was much higher for the modified sorbents (see Fig 4.9); the second linear portion was the gradual equilibrium stage dominated by intraparticle diffusion as a result of the near saturation of the metal ions on the exterior. The molecular metal ions then entered the pores within the particle and were therefore adsorbed in the interior surface. As the molecular metal

ions diffused into the pores of the sorbents, the diffusion resistance increased and consequently this decreased the diffusion rate (Runping *et al*., 2008); the third portion was the final equilibrium stage where the intra-particle began to slow down.

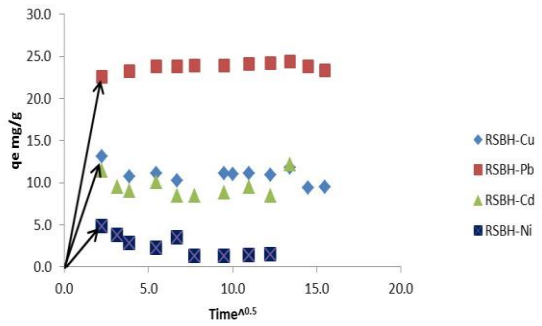

Figure 4.8: Intra-particle diffusion model plot for the adsorption of Cu(II), Pb(II), Cd(II) and Ni(II) on RSBH at concentration of 250 mg/L and 300 K.

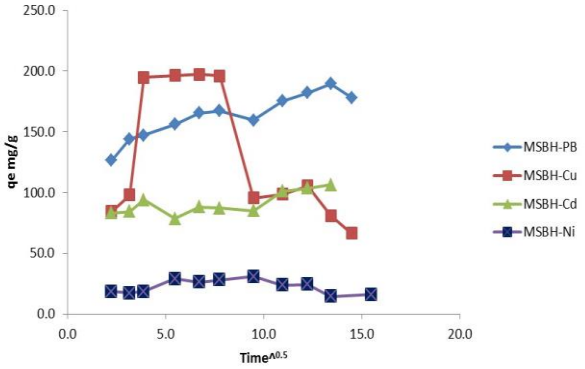

Figure 4.9: Intra-particle diffusion model plot for the adsorption of Cu (II) RSBH and MSBH at concentration of 250 mg/L and 300 K.

4.7 Thermodynamics Study

Table 4.1 showed the thermodynamic parameters of the sorbents onto the metal species at various temperatures. There was a reduction in '*ln K*' which was the adsorption affinity as temperature increased to 323 K before normalizing at higher temperature. This revealed that the reaction may not be favoured by rise in temperature. Although, there was slightly increment in the Gibbs free energy as temperature increased, it showed the spontaneity of the process (Khan *et al*., 2011). Bulgariu and Bulgariu, (2012) in his study of heavy metals removal onto algae waste biomass also observed a decrease in capacity as temperature increased.

The negative free Gibbs energy ΔG^o confirm the spontaneous adsorption of Cu (II) and Ni (II) on RSBH; Cu (II), Pb (II), and Cd (II) on MSBH. The higher negative values of Cu (II) adsorption on RSBH reflected a more energetically favourable adsorption process, (Kosasih *et al*., 2011). Some of the reactions were exothermic as indicated on the negative ΔH^o while some were endothermic. This was as a result of the combination of two processes: desorption of water molecules in the solvent and the adsorption of the adsorbate species (Srivastava *et al*., 2007). It has to be remarked that for both types of reaction very low energy was exchanged with less than 1 kJ mol^{-1} released during sorption for the exothermic and less than 1 kJ mol^{-1} adsorbed for the endothermic reaction.

Table 4.1: Thermodynamic parameters of Pb (II), Cu (II), Cd (II) and Ni (II) sorption

Samples	T(K) 313-333	ΔG (KJ/mol^{-1})	ΔH (KJ/mol^{-1})	ΔS (J/$mol^{-1}K^{-1}$)
RSBH-Pb	313-333	22.16	-0.659	-0.00729
RSBH-Cu	313-333	-80.37	1.635	0.26200
RSBH-Cd	313-333	3.306	-0.115	-0.0106
RSBH-Ni	313-333	-1.146	0.00312	0.00367
MSBH-Pb	313-333	-23.56	0.0684	0.0755
MSBH-Cu	313-333	-32.43	0.0794	0.104
MSBH-Cd	313-333	-0.034	0.00052	0.00011
MSBH-Ni	313-333	1.4951	-0.00729	-0.0048

Oñate (2009) also reported low energy exchange during sorption of Ni (II). Positive value of ΔS^o indicated that there was an increase in disorder at the solid-liquid interphase (Bhaumik *et al*., 2011). It also showed some structural changes in the adsorbate and adsorbent which corresponded to high degree of freedom of the adsorbed species (Lataye *et al*., 2009). Negative values ΔS^o corresponded to decrease in the randomness which revealed the non-spontaneous nature of the reaction. This implied that increase in agitation speed and the addition of stirrer will enhance the spontaneity of reaction. Notably also, was the lower energy associated with the modified sorbent as compared with the raw sorbent. The nonspontaneous reaction was higher for raw sorbent in the order: Ni (II) > Cu (II) > Pb (II) > Cd (II).

5.0 CONCLUSION

The results obtained from the batch adsorption process led to the following conclusions:

(1). The raw sorbents (RSBH) and modified sorbents (MSBH) effectively removed heavy metal ions from a synthesised solution. The FT-IR indicated the presence of functional groups such as; hydroxyl, carboxylic, carbonyls, and phenols groups. The SEM-EDAX revealed the presence of the adsorbed metal species in the sorbents at varying magnifications. The BET test showed that RSBH was highly porous with a surface area of 5.493 m^2/g .

(2). The Batch adsorption time dependent performance was remarkably fast. At 5 minutes of contact time, the adsorption capacities of RSBH and MSBH for Pb (II), which was the metal with highest affinity, were 22.59 mg/g and 126.41 mg/g respectively.

(3). Pseudo Second–order described the kinetics of the sorption process very well. Thus, the calculated amount adsorbed almost equal to experimental amount adsorbed.

(4). The thermodynamic parameters of the metal species adsorption onto the sorbents indicated that most of the reactions were spontaneous and feasible for Cu (II) and Ni (II) adsorption on RSBH; Cu (II), Pb (II), and Cd (II) adsorption on MSBH. The non-spontaneous reactions were for the raw sorbents adsorption of RSBH-Pb (II) and Cd (II) and only MSBH-NI (II).

.

The successful utilisation of these raw and modified shea butter husks for the removal of Pb (II), Cu (II), Cd (II) and Ni (II) in the batch adsorption technique showed a positive impact on the environmental issues in the solid mineral development.

REFERENCES

Abdolali A., Ngo H., Guo W., Lu S., Chen S NguyenN.C., Zhang X., Wang J., and Wu Y (2016). A breakthrough biosorbent in removing heavy metals: Equilibrium, kinetic, thermodynamic and mechanism analyses in a labscale study. *Science of the Total Environment* 542 603–611.

Ahalya, N., Kanamadi, R.D., & Ramachandra, T.V. (2005). Biosorption of chromium (VI) from aqueous solutions by husk of Bengal gram (*Cicer arientinum*). *Electronic journal of Biotechnology*, 8 258-264.

Ahmad, M.F. Haydar, S. (2016). Evaluation of a newly developed biosorbent using packed bed column for possible application in the treatment of industrial effluents for removal of cadmium ions.*Journal of the Taiwan Institut e of Chemical Engineers* http://dx.doi.org/10.1016/j.jtice.2015.12.0321–10

Akhtar, M., Iqbal, S., Kausar, A., Bhanger, M.I., & Shaheen, M.A. (2010). An economically viable method for the removal of selected divalent metal ions from aqueous solutions using activated rice husk. *Colloids and Surfaces B*: *Biointerfaces* 75 149–150.

A Mi rnia, S., Madhumita B. Ray, A.M. (2016). Copper ion removal by Acer saccharum leaves in a regenerable continuous-flow column. *Chemical Engineering Journal* 287 755–764

Ba nsal, M., Singh, D., & Garg, V.K. (2009). A comparative study for the removal of hexavalent chromium from aqueous solution by agriculture wastes carbons. *Journal of Hazardous Materials*, 171 83–92.

Benerjee, K., Ramesh, S.T., Gandhimathi, R., Nidheesh, P.V., Bharathi, K.S. (2012). A novel agricultural waste adsorbent, watermelon shell for the removal of copper from aqueous solutions. *Journal of Environmental Health Science and Engineering*, 3 (2), 143–156.

Bhaumik, R., Mondal, N.K., Das B., Roy P. & Pai, K.C. (2011). Predicting iron adsorption capacity and thermodynamics onto calcerous soil from aqueous solution by linear regression and Neural network modeling, *Journal of Environmental Research and Technology.* 1 (4) 486-499.

Bhausaheb L. Pangarkar, Mukund G. S. & Mahendra G.(2011). Reverse Osmosis and Membrane Distillation for Desalination of Groundwater: A Review. *International Scholarly Research Network ISRN Materials Science.* Volume 2011, Article ID 523124, 9 p

.

Blanesa, P.S, Bordonia, M.E González̈a, J.C, Silvia I. García, A.M. Atria, L.F. Sala, L.F, Sebastián E. Bellú. (2016). Application of soy hull biomass in removal of Cr(VI) from contaminated waters. Kinetic, thermodynamic and continuous sorption studies. *Journal of Environmental Chemical Engineering* 4 (2016) 516–526.

Blázquez, G., Calero, M., Hernáinz, F., Tenorio, G., Martin-Lara, M.A. (2010). Batch and column studies of chromium (III) biosorption by olive stone.

Environmental Progress & Sustainable Energy, 30 (4) 576-585.

Brandhuber, P & Amy, G, (1998). Alternative metods for membrane filtration of arsenic from drinking water. *Desalination,* vol 117, issues 1-3, 1-10.

Bulgariu, D., & Bulgariu L. (2012). Equilibrium and kinetics studies of heavy metal ions biosorption on green algae waste biomass. *Bioresource Techn*ology, 103 489–493.

Chen, J., Cai, Y., Clark, M., & Yu, Y. (2013). Equilibrium and Kinetic Studies of Phosphate Removal from Solution onto a Hydrothermally Modified Oyster Shell Material. *PLoS ONE* 8(4): e60243. doi:10.1371/journal.pone.0060243

Çolak, F., Atarb, N., Yazıcıoğlua, D., Olgun, A. (2011). Biosorption of lead from aqueous solutions by Bacillus strains possessing heavy-metal resistance. *Chemical Engineering Journal*, 173 422– 428.

Daud, W.M.A.W., & Ali, W.S.W., (2004). Comparison on pore development of activated carbon produced from palm shell and coconut shell. *Bioresources Technology.* 93, 63–69.

Escudero, C., Fiol, N., & Villaescusa, I. (2006). Chromium sorption on grape stalks encapsulated in calcium alginate beads**.** *Environmental Chemistry Letter*. 4: 239–242.

Farinella, N.V., Matos, G.D., Lehmann, E.L., & Arruda, M.A.Z. (2008). Grape bagasse as an alternative natural adsorbent of cadmium and lead for effluent treatment. *Journal of Hazardous Material*s, 154 1007-1012.

Fiol, N., Villaescusa, I., Martînez, M., Miralles, N., Poch, J., & Serarols, J. (2006). Sorption of Pb (II), Ni (II), Cu (II) and Cd (II) from aqueous solution by olive stone waste. *Separation and Purification Technology,* 50 132– 140.

Fiol, N., Villaescusa, I., Martînez, M., Miralles, N., Poch, J., & Serarols, J. (2003). Biosorption of Cr (VI) using low cost sorbents, *Environmental Chemistry Letters*, 1 135–139.

Figueiredo, B. R. De Melo, M.M.R, Portugal, I. Ananias, D. Rocha, J. Silva, C.M. (2016). Cs+ removal and optical detection by microporous lanthanide silicate Eu-AV-20 in a fixed-bed column. *Chemical Engineering Journal* 286 48-58

Gilbert, U.A., Emmanuel, I.U., Adebanjo, A.A., & Olalere, G.A. (2011). Biosorptive removal of $Pb^{2+}$and Cd^{2+}onto novel biosorbent: Defatted Carica papaya seeds. *Biomass and bioenergy*, 35 2517-2525.
Grossman, E. (2012). How a Gold Mining Boom Is Killing Children in Nigeria. *Yale Environment,* 360.

Hansen, H.K., Arancibia, F., & Gutiérrez, C. (2010)**.** Adsorption of copper onto agriculture waste materials. *Journal of Hazardous Materials,* 180 442–448.

Ho, Y.S., & McKay, G. (2000). The kinetics of sorption of divalent metal ions onto sphagnum moss flat. *Water Research*, 34, 735–742.

Horsfall, M.S.A., & Abia A.A. (2004). Studies on the influence of mercapoacetic Acid (MAA) modification of cassava (manilot sculenta cranz) waste biomass on the adsorption of $Cu^{2+}$and Cd^{2+} from Aqueous solution. *Bulletin of the Korean Chemical Society*, 969-976.
http://medicalxpress.com/news/2015-05-poisoning-children-central-nigeriagovt.html.Lead poisoning kills 28 children in central Nigeria: Govt (2015, May 14) retrieved 26 September 2016.

Ibrahim, M.N.M., Ngah, W.S.W., Norliyana, M.S., Daud, W.R.W., Rafatullah, M., Sulaiman, O., & Hashim, O. (2010). A novel agricultural waste adsorbent for the removal of lead (II) ions from aqueous solutions. *Journal of Hazardous Materials* 182 377–385.

Johnson, T.A., Jain, N., Joshi, H.C., Prasad, S. (2008). Agricultural and agro-processing wastes as low cost adsorbents for metal removal from wastewater: A review. *Journal of Scientific & Industrial Resesearch,* vol. 67, 647-658

Khoo, K.M. and Ting, Y.P. (2001). Biosorption of Gold by Immobilised Fungal Biomass, *Biochemical Engineering Journal*. 8(1), 51–59.

Khorramabadi, G.S., Soltani, R.D.C., Rezaee, A., Khataee, A.R., and Jafari, A.J. (2011). Utilisation of Immobilised Activated Sludge for the Biosorption of Chromium (VI) *Canadian Journal of Chemical Engineering*, 9999, 1–8,

Kosasih, A.N., Febrianto, J., Sunarso, J., Ju, Y., Indraswati, N., Ismadji, S. (2011). Sequestering of Cu

(II) from aqueous solution cassava peel (Manihotesculenta). *Journal of Hazardous Materials*, 180, 366-374.

Lataye, D.H., I.M. Mishra, I.D. Mall. (2009). Adsorption of α-picoline onto rice husk ash and granular activated carbon from aqueous solution: Equilibrium and thermodynamic study. *Chemcal Engineering Journal*, 147, 139149.

Lugo-Lugo, V., Hernández-López, S., Barrera-DÍaza, C., Ureña-Núñezb, F., & Bryan, B. (2009). A comparative study of natural formaldehyde-treated and copolymer-grafted orange peel for Pb (II) adsorption under batch and continuous mode. *Journal of Hazardous Materials*, 16 The negative free Gibbs energy ΔG^o confirm the spontaneous adsorption of Cu (II) and Ni (II) on RSBH; Cu (II), Pb (II), and Cd (II) on MSBH. The higher negative values of Cu (II) adsorption on RSBH reflect a more energetically favourable adsorption process, (Kosasih *et al*., 2011). Some of the reactions are exothermic as indicated on the negative ΔH^o while some are endothermic. This is as a result of combination of two processes: desorption of water molecule in the solvent and the adsorption of the adsorbate species (Srivastava *et al*., 2007). It has to be remarked that for both types of reaction very low energy is exchanged with less than 1 kJ mol^{-1} released during sorption for the exothermic and less than 1 kJ mol^{-1} adsorbed for the endothermic reaction.1 1255–1264.

Mahmood, N.M., Hayati, B., Arami, M., Lan, C., (2011). Adsorption of textile dyes on

Martînez, M., Miralles, N., Hidalgo, S., Fiol, N., Villaescusa, I,.& Poch, J. (2006). Removal of lead (II) and cadmium (II) from aqueous solutions using grape stalk waste. *Journal of Hazardous Materials*, B133 203–211.

Martín-Lara M.A., Blázquez, G., Calero, M., Almendros, A.I., Ronda, A. (2016). Binary biosorption of copper and lead onto pine cone shell in batch reactors and in fixed bed columns. *International Journal of Mineral Processing* 148 72–82.

Mata, Y.N., Blázquez, M. L., Ballester, A., González, F., & Múnoz, J. A. (2009). Biosorption of cadmium, lead and copper with calcium alginate xerogels and immobilised *Fucusvesiculosus*. *Journal of Hazardous Materials*, 163(2–3), 555–562.

Papageorgiou, S.K., Katsaros, F.K., Kouvelos, E.P., Nolan, J.W., Le Deit, H. & Kanellopoulos, N.K. (2006). Heavy metal sorption by calcium alginate beads from *Laminaria digitata*. *Journal of Hazardous Materials*, 137 (3) 1765-1772

Pine Cone from colored wastewater: kinetic, equilibrium and thermodynamic studies. *Desalination*, 268, 117– 125.

Podder, M.S. Majumder, C.B (2016). Fixed-bed column study for As(III) and As(V) removal and recovery by bacterial cells immobilized on Sawdust/MnFe2O4 composite. *Biochemical Engineering Journal* 105 114– 135

Podder, M.S. Majumder, C.B., (2011). Study of the kinetics of arsenic removal from wastewater using *Bacillus arsenicus* biofilms supported on a Neem leaves/MnFe2O4 composite. *Ecological Engineering* 88 195–216

Runping, H., Pan, H., Zhaohui, C.A., Zhenhui, Z., & Mingsheng, T. (2008). Kinetics and isotherms of Neutral Red adsorption on peanut husk. *Journal of Environmental Sciences*, 20 1035–104.

Srivastava, V.C. Mall, I.D. & Mishra, I.M. (2006). Characterization of mesoporous rice husk ash (RHA) and adsorption kinetics of metal ions from aqueous solution onto RHA. *Journal of Hazardous Materials*, B 134, 257– 267.

Tchounwou, P.B. Yedjou, C. G. Patlolla, A.K. Sutton, D.J. (2014). Heavy metals toxicity and the environment. HHS Public Access doi: 10.1007/978-3-7643-8340-4 6.

Villaescusa, I. Fiol, N. Martînez, M. Miralles,N. Poch, J. & Serarols, J. (2004). Removal of copper and nickel ions from aqueous solutions by grape stalks wastes. *Water Research*, 38 992–1002.

Wang, M., Huang, Z., Liu, G., Kang, F. (2011). Adsorption of dimethyl sulfide from aqueous solution by a costeffective bamboo charcoal. *Journal of Hazardous Materials*, 190 (2011) 1009–1015. Retrieved from http://www.elsevier.com/locate/jhazmat

Yahya, M.D., Mohammed-Dabo, I.A., Ahmed, A.S., & Olawale, A.S (2013). Adsorptive removal of lead from aqueous solution using raw and modified shea butter cake. *Journal of the Nigerian Society of Chemical Engineers*, 28 25-33.

Zulfikar, M.A., Novita, E., Hertadi, R., Djajanti, S.D. (2013). Removal of humic acid from peat water using untreated powdered eggshell as a low cost adsorbent. *International journal of Science and Technology*. 10: 13571366. Doi 10.1007/s13762-013-0204-5.

OPTIMIZATION OF THE ADSORPTION OF ERICHROME BLACK-T FROM AQUEOUS SOLUTION USING NTEJE LOCAL CLAY, ANAMBRA STATE

Nwabanne T Joseph[1] and Onu E Chijioke[2*]
[1,2]Department of Chemical Engineering, Nnamdi Azikiwe University, Awka, Nigeria.
[*]Corresponding author: **onuchijioke894@gmail.com**

ABSTRACT

Response Surface Methodology (RSM) was used to optimize the adsorption of Erichrome Black-T (EBT) dye using a local clay obtained from Nteje, Oyi Local Government Area, Anambra State, as an adsorbent. The elemental and oxides compositions of the clay were determined using Atomic Absorption Spectrometer (AAS) and X-Ray Fluorescence (XRF) respectively. The clay was acid activated using Hydrochloric acid. Central Composite Design (CCD) was used to optimize the adsorption process and evaluate the individual and interactive effects of dosage, contact time, temperature and pH. The quadratic model was seen to best describe the optimization process. The correlation coefficient of 0.9550 obtained showed that 95.50% of the variability in the response can be explained by the model. There was also a good agreement between the experimental and predicted responses of the optimization process, thus confirming the suitability of the proposed quadratic model. The optimization results showed that the maximum adsorption percentage of 95.70% was obtained at a time of 30 minutes, dosage of 0.40g, temperature of 35^{o}C and a pH of 1.17. The results revealed that the local Nteje clay used in this study is a good adsorbent for the removal of Eriochrome Black-T dye from aqueous solution.

KEYWORDS: *Response Surface Methodology, Adsorption, clay, Experimental design, dye*

1.0 INTRODUCTION

Wastewater from some industries such as textile and pulp/paper industries are often rich in colour, containing residues of reactive dyes and chemicals. The discharge of such untreated or inadequately treated coloured waste water into the water bodies, is not only damaging to the aesthetic nature of receiving streams but may also be toxic to the aquatic life (Mumin et al., 2007). Their presence even in very low concentration is highly viable and will affect aquatic life as well as food web (Nwabanne et al, 2010). Furthermore, the dyes make penetration of sunlight to reach the lower layers very difficult thus affecting the efficiency of aquatic plants in performing photosynthesis (Pragnesh et al, 2011) thereby resulting in an imbalance in the ecosystem.

Thus the removal of dyes from coloured effluents, particularly from textile industries, is one of the major environmental concerns these days (Wu *et al*, 2001). Many physical and chemical treatment methods including adsorption, coagulation, precipitation, filtration, electrodialysis, membrane separation and oxidation have been used for the treatment of dye- containing effluents (Robinson et *al*, 2001). Many challenges, however, have been associated with most of the above methods including high cost, low efficiency, generation of toxic products and inability to regenerate the starting materials (Ehssan and Yehia, 2012). Owing to these problems, emphasis has now been shifted to the use of adsorption for the removal of wastewater pollutants, which is now one of the efficient techniques (Sunil *et al*, 2012). Activated carbon which has excellent adsorption efficiency as an adsorbent is usually limited in use due to its high cost.

Therefore, because of the high cost implications and other factors, attempts are being made to get alternate adsorbents which are relatively inexpensive, abundant and also efficient (Onu and Nwabanne, 2014a). These studies include the use of Bagasse pith (Mckay , 1998), Coal (Mohan et al, 2002), Palm-fruit bunch (Nassar, 1997), Fly ash (Nollet et al, 2003; Gupta and Ali, 2004) etc as adsorbent. Clay which is a finely divided muddy material is being investigated for its adsorptive properties. It has high specific area and ability to hold water in the interlayer sites which makes it a potentially excellent adsorbent. Many authors have reported their works on clay. (Ehssan and Yehia, 2012; Djebbar et al, 2012).

The one factor at a time (OFTA) is where only one factor is varied while all the others are kept constant. The disadvantages in using the one factor at a time (OFTA) method in experiments is that it is time consuming, requires large number of experiments to determine optimum levels and most times incapable of reaching the true optimum as interaction among variables is not taken into consideration (Onu and Nwabanne, 2014b; Trinh and Kang, 2010; Ghafari *et a*l, 2009). Moreover, this method neglects the interaction effects of process variables. The experimental design method addresses the main and interaction effects of the process variables which can then be used to provide the appropriate approach in establishing a model correlating the

response variable and the independent variables (Ajemba and Onukwuli, 2012).

The statistical method of Response Surface Methodology (RSM) has been proposed to include the influence of individual factors and the effects of their interactions including the optimum conditions for desirable responses at a lower number of experiments (Ajemba et al, 2013). Central Composite Design is used to carry out statistical analysis and the diagnostic checking test that is used to evaluate the adequacy of the models.

2.0 MATERIALS AND METHODS

2.1 Raw Material Sourcing

The clay was obtained from Nteje, Oyi Local Government Area, Anambra State, Nigeria. The clay was grey in color and was obtained as a dry lumped sample. The Eriochrome Black-T dye and all the chemicals used were of analytical grades. The structure of the malachite green is shown in Figure 1.

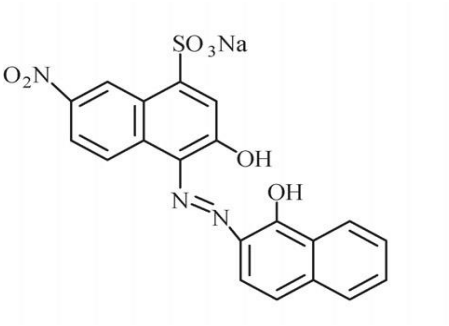

Figure 1: Structure of Eriochrome Black-T

2.2 Preparation of Clay

The clay was prepared for activation by sun drying, ground into fine particles and sieved to a particle size of 300µm. 50g of the clay sample was mixed with 250ml of 2.5M hydrochloric acid. The resulting suspension was heated on a magnetically stirred hot plate at a temperature of 98^{o}C for 2 hours. After cooling, the samples were washed several times with de-ionized water until a pH of 6–7, filtered with Whatman No 1 filter paper and dried in the oven at 110^{o}C for 3 hours. The dried sample was ground again and sieved at different sizes and finally stored in a desiccator ready for use.

2.3 Physical Properties of Clay

The moisture content was determined using ASTM D 2867-91. The pH of the clay was determined using standard test of ASTM D 3838-80 (ASTM, 1996). The surface area of the clay was determined using the Sear's method (Al-Quadah and Shawabkah, 2009; Alzaydian, 2009). The clay was characterized using Atomic Absorption Spectrometer (AAS) and X-Ray Fluorescence (XRF) to respectively determine

the elemental compositions and the component oxides in the clay.

2.4 Batch Adsorption Method

The activated clay was characterized for its adsorption capacity on Eriochrome Black-T dye. The model wastewater was prepared by dissolving 0.1g of the dye in 1000ml of distilled water each to get a solution of 100mg/l. Then appropriate volume of the dye and the clay were mixed and heated on a stirrer at a specified time, temperature and pH. After the adsorption, the solution was centrifuged and the absorbance measured at its wavelength of 520nm.

The percentage of solute adsorbed is calculated using Equation 1 (Djebbar et al, 2012):

$$\text{Percent adsorbed } \% = \left(\frac{C_i - C_e}{C_i}\right) X\ 100 \quad (1)$$

where, C_i and C_e (mg/L) are the liquid – phase concentrations of dye at initial and equilibrium conditions respectively.

2.5 Optimization Using Central Composite Design (CCD)

The Central Composite Design (CCD) was used to study the effects of the variables on their responses and subsequently in the optimization studies.

Batch experiments were carried out in other to determine the combine effects of temperature, dosage, pH and time which were the independent variables. The percentage adsorbed was the dependent variable or the response. The coded values of the process parameters were determined by

$$x_i = \frac{X_i - X_o}{\Delta x} \quad (2)$$

where x_i – coded value of the ith variable,

X_i – uncoded value of the ith test variable and

X_o – uncoded value of the ith test variable at center point.

The regression analysis was performed to estimate the response function as a second order polynomial

$$Y = \beta_o + \sum_{i=1}^{k} \beta_i X_i + \sum_{i=1}^{k} \beta_{ii} X_i^2 + \sum_{i=1}^{k-1} \sum_{j=2}^{k} \beta_{ij} X_i X_j \quad (3)$$

where Y is the predicted response, β_i, β_j, β_{ij} are coefficients estimated from regression. They represent the linear, quadratic and cross products of X_1, X_2 and X_3 on the response.

A statistical program package, Design Expert trial version 8.0.7.1 was used for regression analysis of the data obtained and to estimate the coefficient of the regression equation. The equations were validated using the ANOVA analysis. Using four factor variables and six centre points gave the CCD design of 30 runs (Table 1).

3.0 RESULT AND DISCUSSION

3.1 Physical Properties of the clay

Table 2 shows the result of the physical properties of the clay before and after activation with hydrochloric acid. It is

seen that there was a big increase in the surface area of the clay after the acid activation.

The percentage of moisture content and the oil retention increased slightly after the activation.

Table 1: Factors levels of Independent Variables for EBT Adsorption

Independent Factors	-α	Low level (-)	Medium level (0)	High level (+)	+α
Temp, ^{o}C	27.93	30	35	40	42.07
Time, min	1.72	10	30	50	58.24
Dosage, g	0.117	0.2	0.4	0.6	0.68
pH	1.17	2	4	6	6.83

Table 2: Physical Properties of the Clay

Property	**Un-activated Clay**	**Activated Clay**
Surface area(m^2/g)	55	199
pH	7.1	6.1
Moisture (%)	13.9	14.79
Oil retention (%)	10.40	20.22

The results of the AAS and XRF analyses are given in Tables 3 and 4. The AAS results revealed that the clay contained more of aluminum, iron and sodium though there are traces of zinc, magnesium and copper. The XRF result showed that the clay is mainly silicate in nature.

Table 3: AAS Results of the Clay

Element	**Clay Composition (ppm)**
Al	35.4839
Fe	23.6340
Na	11.5033
K	0.2934
Mn	0.2204
Ca	0.1214
Ni	0.1059
Mg	0.0485
Cu	0.0264
Zn	0.0190

Table 4: XRF Results of the Clay

Chemical Constituents	**Composition (%)**
SiO_2	56.6
Fe_2O_3	19.29
AL_20_3	17.5

TiO_2	2.36	Cr_2O_3	0.09
CaO	1.52	ZnO	0.06
MnO	0.20	NiO	0.04
V_2O_5	0.14	CuO	0.03

3.2 Statistical Analysis of the Optimization of the Adsorption Process

Design Expert was used to analyze the optimization results. In Table 5, the summary of P-values and the Adjusted R-squared value showed that linear and 2FI models were not suggested. The cubic model is always applied because the CCD does not contain enough runs to support a full cubic model. Therefore, only the quadratic model fitted the analysis and hence it was suggested. A significance level of 95% was used implying that all terms whose P-values were less than 0.05 were considered significant. The model summary test presented in Table 6 showed that the quadratic model had standard deviation value of 2.46 and correlation coefficient value of 0.9950.

Table 5. Summary of P-values

Source	Sequential p-value	Lack of Fit p-value	R-Squared	Adjusted R-Squared	Predicted Remark
Linear	< 0.0001	< 0.0001	0.6253	0.5360	Not suggested
2FI	0.4169	< 0.0001	0.6311	0.2446	Not suggested
Quadratic	< 0.0001	< 0.0001	0.9130	0.7249	Suggested
Cubic	0.0001	< 0.0001	0.9944	0.8294	Aliased

Table 6: Model Summary Statistics for EBT Adsorption on NHC Clay

Source	Std. Dev.	Adjusted R-Squared	Predicted R-Squared	PRESS	Remark
Linear	5.11	0.6770	0.6253	0.5360	938.34	Not suggested
2FI	5.07	0.7583	0.6311	0.2446	1527.61	Not suggested
Quadratic	2.46	0.9950	0.9130	0.7249	556.35	Suggested
Cubic	0.62	0.9987	0.9944	0.8294	345.07	Aliased

3.3 Analysis of Variance (ANOVA)

The ANOVA analysis is shown given in Table 7. The F-value of 22.74 observed implied that the model was significant and this was validated by the P-value being less than 0.0001. The P values were used as a tool to check the significance of each of the coefficients, which in turn were

necessary to understand the pattern of the mutual interactions between the test variables (Shrivastava et al, 2008). The larger the magnitude of F-test value and the smaller the magnitude of P-value, the higher the significance of the corresponding coefficient (Alam et al, 2008).

The adequate precision measured the signal to noise ratio and compared the range of the predicted value at the design points to the average prediction error. The adquate predicion ratio above 4 indicated adequate model efficacy (Kumar et al, 2007). Hence, the adequate precision ratios of 21.687

Table 7: ANOVA Analysis of the Quadratic Model

Source	Sum of Squares	df	Mean Square	F Value	P-value Prob > F
Model	1931.30 14	137.95	22.74	< 0.0001	
A-temp	25.51	1	25.51	4.20	0.0582
B-Time	296.56	1	296.56	48.88	< 0.0001
C-Dosage	348.72	1	348.72	57.48	< 0.0001
D-pH	698.28	1	698.28	115.09	< 0.0001
AB	0.052 1	0.052	8.530E-003	0.9276	
AC	3.16 1	3.16	0.52	0.4816	
AD	1.62	1	1.62	0.27	0.6130
BC	94.53	1	94.53	15.58	0.0013
BD	33.96 1	33.96	5.60	0.0319	
CD	31.11	1	31.11	5.13	0.0388
A^2	74.51 1	74.51	12.28	0.0032	
B^2	68.07	1	68.07	11.22	0.0044
C^2	82.64 1	82.64	13.62	0.0022	
D^2	0.59 1	0.59	0.097	0.7603	
Residual	91.01	15	6.07		
Lack of Fit	91.01	10	9.10	1.300E+005	< 0.0001
Pure Error	3.500E-004	5	7.000E-005		
Cor Total	2022.30	29			

Std. Dev. = 2.46; Mean = 82.16; C.V. = 3.00%; PRESS = 556.35

R-Squared = 0.9550; Adj R-Sq = 0.9130; Pred R-Sq = 0.7249; Adeq Precision = 21.687

indicated adequate model efficency. Also, a PRESS value of 556.36 indicated an adequate signal implying that the model can be used to navigate the design space.

The coefficient of regression R^2 was used to validate the fitness of the model equation. The R^2 has a high value of 0.9550 showing that 95.50% of the variability in the response can be explained by the model. This implied that the prediction of experimental data was quite satisfactory. The quadratic model equation obtained for the EBT adsorption was:

$$Y(\%) = 88.0 + 1.13A + 3.85B + 4.18C - 5.91D - 0.057AB - 0.44AC + 0.32AD - 2.43BC + 1.46BD + 1.39BD - 2.83A^2 - 2.70B^2 - 2.98C^2 - 0.25D^2 \quad (4)$$

In a regression equation a positive sign of the independent variable means that an increase in the variable will cause an increase in the response while a negative sign will result in a decrease in the response (Kumur et al, 2008). Hence, a decrease in pH will cause an increase in the percentage adsorbed while an increase in temperature, time, and dosage will cause an increase in the percentage adsorbed. pH had the most significant effect on the response since its coefficient of 5.91 was the highest. Values of P less than 0.05 indicated that the model term is significant. Hence, it was observed that, among the test variables used in the study that B, C, D, BC, BD, CD, A^2, B^2, and C^2 are significant model terms. Therefore, eliminating the insignificant terms, the final model equation was:

$$Y(\%) = 88.0 + 3.85B + 4.18C - 5.91D - 2.43BC + 1.46BD + 1.39CD - 2.83A^2 - 2.70B^2 - 2.98C^2 \quad (5)$$

A combination of the experimental response and the predicted response are given in Table 8. It was observed that there was a close correlation between the experimental response and the predicted response. This close correlation confirmed the effectiveness of the adsorption of EBT dye using the clay. The optimization result showed that the maximum adsorption percentage of 95.70% was obtained at a time of 30 minutes, dosage of 0.40g, temperature of 35°C and a pH of 1.17.

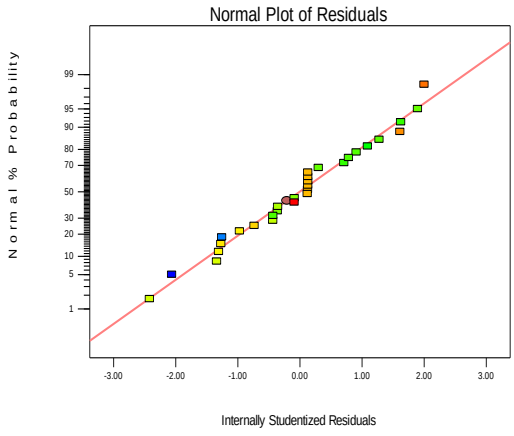

Figure 2: Normal Plot of Residuals for the EBT Adsorption

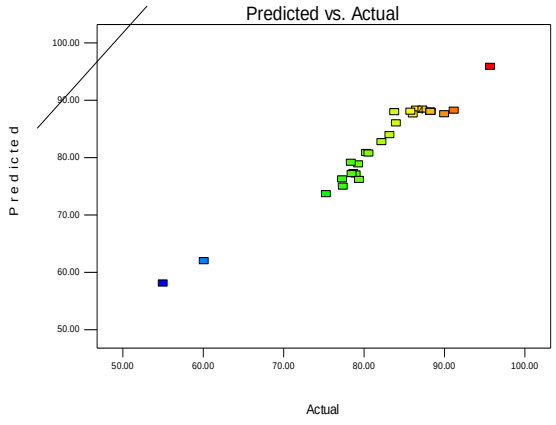

Figure 3: Predicted vs Actual Plot for the EBT Adsorption

The normal plot of residuals and the predicted vs actual plots shown in Figures 2 and 3 were used to check whether the points were linear, and thus followed a normal distribution. The points were linear, thus confirming the good agreement between the experimental values and the predicted values of the response though some small scatter like an "S" shape was observed. These plots equally confirmed that the selected model was adequate in predicting the response variables in the experimental values.

3.4 Three Dimensional (3D) Surface Plots for EBT Adsorption

Response surface plots as a function of two factors at a time, maintaining all other factors at fixed levels are more helpful in understanding both the main and the interaction effects of the two factors. These plots can be easily obtained by calculating from the model, the values taken by one factor where the second varies with constraint of a given Y value. The nature of the response surface curves showed the interaction between the variables. The elliptical shape of the curve is an indication of good interaction between the two variables and the circular shape indicated no interaction between the variables. The elliptical nature of the contours depicted interactions of all the variables (Figures 4 – 8). There was a relative significant interaction between every two variables, and there was a maximum predicted yield as indicated by the surface confined in the smallest ellipse in the contour diagrams. The initial rapid adsorption was due to the initial large availability of the positively charged surface of the adsorbent for the adsorption of the EBT. As seen from the 3D surface plots, dosage played a significant role in the percentage adsorbed. Increase in the percentage adsorbed as a result of increase in dosage was due to mainly the higher surface area availability, which led to higher adsorption of malachite green. Temperature also increased the percentage adsorbed because the rate of diffusion of adsorbate molecules across the external boundary layer increased.

Table 8: Actual and Predicted Values of the Adsorption of EBT

Std	A = Temp	B = Time	C = Dosage	D = pH	Experimental Percentage Removed (%)	Predicted Percentage Removed (%)
1	30.00	10.00	0.20	2.00	77.30	76.24
2	40.00	10.00	0.20	2.00	79.31	78.86
3	30.00	50.00	0.20	2.00	84.00	86.00
4	40.00	50.00	0.20	2.00	86.50	88.40
5	30.00	10.00	0.60	2.00	86.10	87.55
6	40.00	10.00	0.60	2.00	87.30	88.40

7	30.00	50.00	0.60	2.00	90.00	87.59
8	40.00	50.00	0.60	2.00	91.20	88.21
9	30.00	10.00	0.20	6.00	55.00	58.08
10	40.00	10.00	0.20	6.00	60.10	61.98
11	30.00	50.00	0.20	6.00	75.30	73.67
12	40.00	50.00	0.20	6.00	78.70	77.34
13	30.00	10.00	0.60	6.00	77.40	74.97
14	40.00	10.00	0.60	6.00	79.00	77.09
15	30.00	50.00	0.60	6.00	80.30	80.84
16	40.00	50.00	0.60	6.00	82.20	82.73
17	27.93	30.00	0.40	4.00	80.60	80.75
18	42.07	30.00	0.40	4.00	83.20	83.94
19	35.00	1.72	0.40	4.00	78.50	77.15
20	35.00	58.28	0.40	4.00	85.80	88.04
21	35.00	30.00	0.12	4.00	79.40	76.14
22	35.00	30.00	0.68	4.00	83.80	87.95
23	35.00	30.00	0.40	1.17	95.70	95.85
24	35.00	30.00	0.40	6.83	78.40	79.14
25	35.00	30.00	0.40	4.00	88.29	88.00
26	35.00	30.00	0.40	4.00	88.30	88.00
27	35.00	30.00	0.40	4.00	88.30	88.00
28	35.00	30.00	0.40	4.00	88.28	88.00
29	35.00	30.00	0.40	4.00	88.30	88.00
30	35.00	30.00	0.40	4.00	88.30	88.00

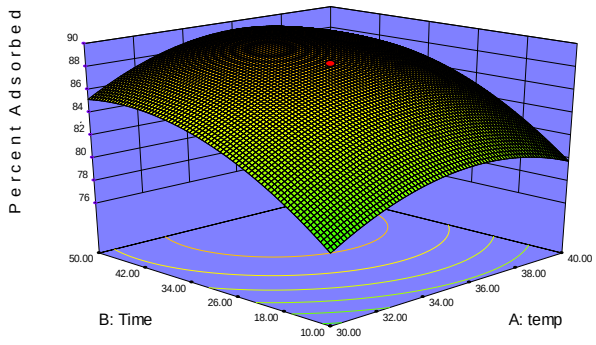

Fig 4: 3D Surface Plot for EBT Adsorption on NHC showing Combined Effects of Time and Temperature

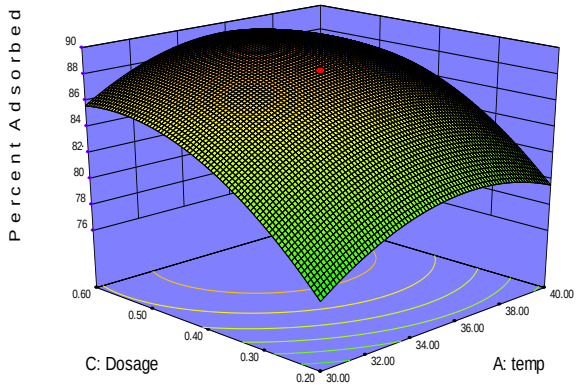

Fig 5: 3D Surface Plot for EBT Adsorption on NHC showing Combined Effects of Dosage and Temperature

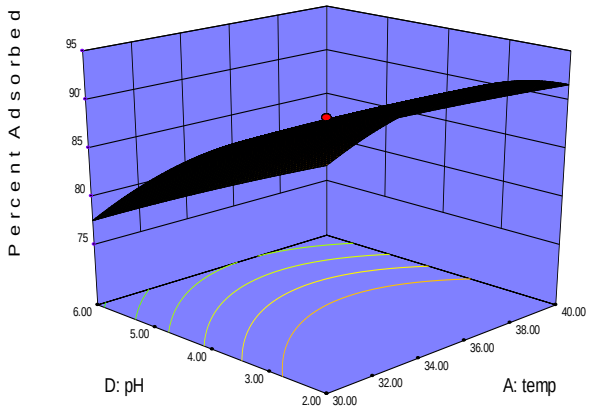

Fig 6: 3D Surface Plot for EBT Adsorption on NHC showing Combined Effects of pH and Temperature

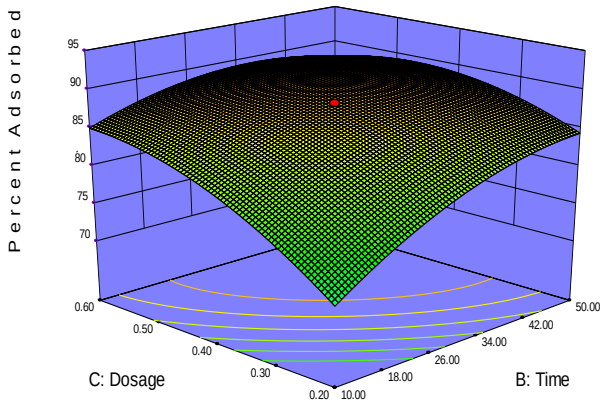

Fig 7: 3D Surface plot for EBT Adsorption on NHC showing Combined Effects of Dosage, pH and Time

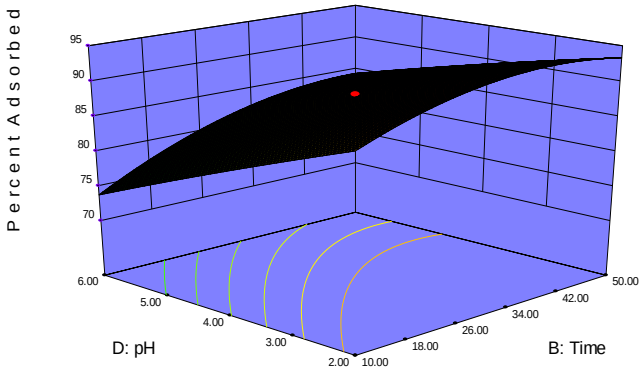

Fig 8: 3D Surface Plot for EBT Adsorption on NHC showing Combined pH and Time.

4.0 CONCLUSION

Readily available clay from Nteje was activated and used to adsorb Eriochrome Black-T from solution. The AAS showed that the major elements in the clay were Aluminum, Iron and Sodium. While the XRF showed that silicon oxide is the major oxide in the clay. The surface area increased with acid activation and pH was observed to have the greatest effect on the optimization process. The quadratic model was found to be the best model for the statistical analysis, while the close agreement between the experimental and predicted responses confirmed the suitability of the quadratic model. The optimum conditions were obtained at a time of 30 minutes, dosage of 0.40g, temperature of 35^{o}C and a pH of 1.17 which gave a maximum adsorption percentage of 95.70%. The results obtained showed conclusively that the Local Nteje Clay, OYI LGA, Anambra State, is a good

adsorbent for the removal of Erichrome Black-T from aqueous solution.

ACKNOWLEDGEMENT

The financial assistance extended by Mobil Producing (Exxon Mobil) Nigeria in carrying out this research work is highly appreciated.

REFERENCES

Ajemba, R. O. and Onukwuli, O. D. (2012) 'Response Surface Optimization of Palm Oil
Bleaching using Hydrochloric Acid Activated Ukpor Clay', *European Journal of Scientific Research,* Vol. 82, No. 3, pp. 325-339.

Ajemba, R. O., Igbokwe, P. K. and Onukwuli, O. D. (2013) 'Optimization of Color Pigments Removal from Palm Oil by Activated Ukpor Clay Using Response Surface Methodology', *Research Journal of Applied Sciences, Engineering and Technology* Vol. 6, No. 3, pp. 423 – 432.

Alam, Z., Muyibi, S. A. and Kamsldin, N. (2008) 'Production of activated carbon from oil palm empty fruit bunches for removal of zinc. Proceedings of Twelfth International Water Technology Conference, Aixeandria Egypt, pp. 373-382.

Djebbar, M., Djafri, F. and Bouchekara, D. A. (2012) 'Adsorption of phenol on natural clay',
Applied Water Science, Vol. 2, pp. 77-86.

Ehssan, N. and Yehia, E. (2012) 'Adsorption of Phenol from Aqueous Solution by Local Egyptian Bentonite'. *Journal of American Science* Vol. 8, No. 8, pp. 1-9.

Ghafari, S., Aziz, H. A., Isa, M. H. and Zinatizadeh, A. K. (2009) 'Application of response surface methodology(RSM) to optimize coagulation-flocculation treatment of leachate using polyaluminium chloride(PAC) and alum', *Journal of Hazardous Materials*, Vol. 163, pp. 650-656.

Gupta, V. K., and Ali, I. (2004) 'Removal of Lead and Chromium from wastewater using bagasse fly ash-sugar industry waste', *Journal of Colloid Interface Science*, Vol. 271, No. 2, pp. 321- 329.

Krumar, A., Prasad, B. and Mishra, I. M. (2007) 'Process parametric study of ethane carboxylic acid removal onto power activated carbon using Box-Behnken design', *Chemical Engineering Technology*, Vol. 30, No. 7, pp. 932-937.

Krumar, A., Prasad, B. and Mishra, I. M. (2008) 'Adsorption removal of acrylonitrile using powered activated carbon', *Journal of Environmental protection Science*, Vol. 2, pp. 54-62.

Mckay, G. (1998) 'Application of surface diffusion model to the adsorption of dyes on bagesse pith', *Adsorption*, Vol. 4, pp. 361- 372.

Mohan, S. V., Rao, N. C. and Karthikeyan, J. (2002) 'Adsorption removal of direct azo dye from aqueous phase onto coal based sorbents: a kinetic and mechanistic study', *Journal of Hazard Mater*, Vol. 90, pp. 189-204.

Mumin, M. A., Khan, M. M. R., Akhter, K. F. and Uddin, M. J. (2007) 'Potentiality of open burnt clay as an adsorbent for the removal of Congo red from aqueous solution, *International Journal Environmental Science Technology*, Vol. 4, No. 4, pp. 525-532.

Nassar, M. M. (1997) 'The kinetics of basic dye removal using palm-fruit bunch', *Adsorption. Science Technology*, Vol. 15, pp. 609-617.

Nollet, H., Roels, M., Lutgen, P., Meeren, P. V. and Verstraete, W. (2003) 'Removal of PCBs from wastewater using fly ash' *Chemosphere*, Vol. 53, pp. 655-665.

Nwabanne, J. T., Asomugha, V. N. and N. Onyemelukwe. (2010). 'Equilibrium and kinetic modeling of adsorption of methyl orange dye on palmyra palm nut', *Journal of Engineering and Applied Sciences*. Vol. 6, pp. 11-16.

Onu, C. E. and Nwabanne, J. T. (2014a) 'Adsorption Kinetics for Malachite Green Removal from Aqueous Solution Using Nteje Clay', *Journal Of Environment And Human*, Vol. 1, No. 2, pp. 133 – 150.

Onu, C. E. and Nwabanne, J. T. (2014b) 'Application of Response Surface Methodology in Malachite Green Adsorption Using Nteje Clay', *Open Journal Of Chemical Engineering And Science*, Vol. 1, No. 2, pp. 19 – 33.

Pragnesh, N. D., Satindar, K. and Ekta, K. (2011) 'Removal of eriochrome black –T by adsorption onto eucalyptus bark using green technology', *Indian Journal of Chemical Technology*. Vol. 18, pp. 53-60.

Robinson, T., McMullan, G., Marchant, R. and Nigam, P. (2001) 'Remediation of dyes in textile effluent: a critical review on current treatment technologies with a proposed alternative' *Bioresource Technology*, Vol. 77, pp. 247–255.

Shrivastsvs, A., Sandagar, P., Baja, I. and Singhal, R. (2008) 'Media optimization for the production of U-linolenic acid by cunninghamella echinulata varielegans MTCC 522 using response surface methodology', *International journal of food Engineering*, Vol. 4, No. 2, pp. 1-32.

Sunil, K., Gunasekar, V. and Ponnusami, V. (2012) 'Removal of methylene blue from aqueous effluent using fixed bed of groundnut shell powder', *Hindawi Publishing Corporation Journal of Chemistry*, Vol. 1, pp. 1-5.

Trinh, T. K. and Kang L.S. (2010) 'Application of response surface method as an experimental design to optimize coagulation test', *Environmental Engineering Research*, Vol. 15, No. 2, pp. 063-070.

Wu, F. C., Tseng, R. L. and Juang, R. S. (2001) 'Adsorption of dyes and phenols from water on the activated carbons prepared from corncob wastes', *Environmental technology*, Vol. 22, pp. 205 – 13.

.

STUDY OF DRYING CHARACTERISTICS OF CASSAVA (*MANIHOT ESCULENTA*) USING A REFRACTANCE™ WINDOW DRYER

Akinjide A. Akinola* and Stanley N. Ezeorah
Department of Chemical and Petroleum Engineering, University of Lagos, Lagos, Nigeria
Email: akinjideakinola@gmail.com, aaakinola@unilag.edu.ng

ABSTRACT

The drying characteristics of 3 mm thick cassava slices using a Refractance™ Window dryer is presented in this study. The dryer was constructed by modifying a laboratory water bath. The cassava slices were dried on the Refractance Window™, and the moisture contents of the slices were measured as the drying progressed. A water temperature of between 75°C – 80°C was maintained beneath the transparent Polyethylene terephthalate (PET) plastic film. Drying curves were obtained from the drying data and the thin layer model that best fits the drying data determined. The bulk density and rehydration ratio of the dried cassava were determined. Regression analysis results showed that the Haghi and Ghanadzadeh thin layer model gave the best agreement with the drying data for 3 mm sized slices. The Mean Bias Error (MBE), the coefficient of determination (R^2), the Root Mean Square Error (RMSE), and the Chi-square ($\chi 2$) values were -8.83x10^{-6}, 0.998434, 0.00420 and 0.000441 respectively. Observations indicated that the Cassava slices dried to about 5% after in about 210 minutes and the bulk density was determined to be 0.62 g/cc. The steady Rehydration Ratio of about 3.2 was maintained after a rehydration time of 120 minutes. The effective moisture diffusivity of the yam slices was found to be 4.94673 x 10^{-6} m^2/s.

Keyword: Cassava, Refractance Window™ Drying, Thin Layer drying, Drying Kinetics

1.0 INTRODUCTION

Cassava (*Manihot esculenta*) tubers are processed into flour and "garri" which are then used in the preparation of many Nigerian Cuisines. Cassava peels have also been used as a source of animal feed. Cassava tubers and its products are excellent sources of dietary energy (Ayankunbi *et al.*, 1991; Tunde-Akintunde and Afon, 2010). The roots contain about 32% starch, 65% moisture, 0.8–1% protein on a wet weight basis; the roots also contains 92.5% Carbohydrate and 3.2% on a dry basis (Cock, 1985). Over 200 million people worldwide rely on cassava products as a major source of dietary calories. By supplying up to 250 kilocalories/ha (Cock, 1985), cassava tubers are the most efficient calories producers of all food crops.

The Cassava flour and "garri" preparation process involves peeling, slicing, cleaning and drying the tuber. The dried cassava tuber is then grinded into fine powder to make "elubo" or grated to make "garri". The preparation process is laborious and time-consuming (Lancester *et al.*, 1982) and the quality of the cassava flour or "garri" produced is determined mainly in the drying stage. Natural sun drying is the most common method of drying of cassava tubers in regions where they are grown (Mlingi, 1995). However, this process is slow as it depends on the ambient temperature in those regions. Also, natural sun drying can only be done properly in the dry season months. When drying times exceed three days, the quality of the product may degrade. If the drying process is fast enough, and the final product is dry enough, this degradation can be prevented (Marsh, 2002). There is, therefore, a need to find for faster drying methods of reducing significantly, the time to dry cassava tubers. The Refractance Window™ Drying technique is a new method of drying. The method has typically been used to convert liquid foods and related biomaterials into flakes, powders and sheets. Nindo and Tang (2007), studies indicated using the Refractance Window™ Drying technique, purees and juices prepared from fruits, vegetables, or herbs could be dried in short times, typically 3 – 5 min. In this study, the drying of cassava slices using the Refractance Window™ Drying technique is investigated.

2.0 MATERIALS AND METHODS

2.1 Equipment

A picture of the equipment used is shown in Fig. 1. The equipment is a Refractance Window™ type dryer constructed by modifying an thermostatically heated water bath. The bath's metal cover was replaced with a transparent Polyethylene terephthalate (PET) plastic film which was secured in place so that the plastic film is always in contact with the water. The plastic film had

a thickness of 0.15 mm. The water in the bath was heated with a 2.5kW electric emersion heater. The apparatus consists of a Refractance Window™ (A), Type K thermocouples (B1, B2 and B3) used to measure the temperature of the water bath, top of plastic film and the temperature of a cassava slice. The thermocouples were connected to a Measurement Computing's USB-5100 Series Multi-Channel data logger (C); the data-logger was connected to the personal Computer (D). The air-vapour mixture above the dryer was removed by the stream of air blown by a fan (E). The fan rotated at 1300/1800 rpm and was placed beside the Refractance Window™ dryer.

.

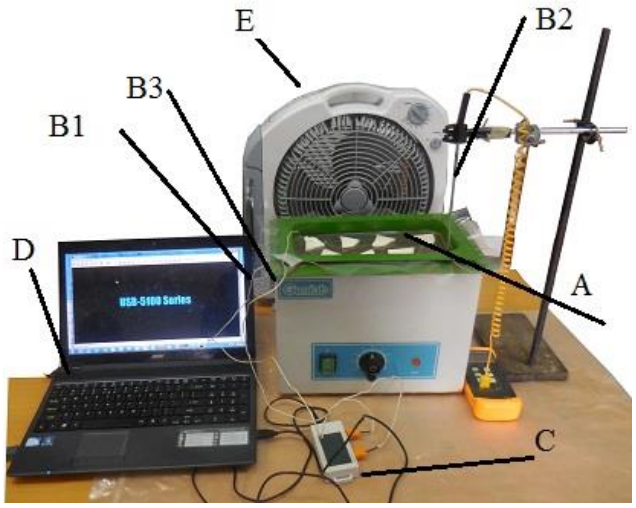

Fig. 1 Set up of the Apparatus Used

2.2 Experimental Method

With the plastic film secured in place, the water in the bath was heated to a temperature of 75 ^{o}C - 80 ^{o}C and this temperature range was maintained throughout the experiment. The cassava slices were then placed on the plastic film to dry. As the experiment progressed, at specific times, some cassava slices were removed and the moisture content determined, using a moisture analyzer. The drying process was stopped when the moisture content of the sample reached about 5 % (w.b). The drying experiments were replicated three times for each drying period and the average moisture content values taken.

Preparation of Cassava Slices

The cassava tubers used in this study were obtained from a local farm. The tubers were washed, peeled and cut into 3 mm thick slices using a Benriner Japanese Mandolin type slicer manufactured by Benriner Co. Ltd., Iwakuni-City, Japan. The cassava slices were soaked in water whose initial temperature was 70 ^{o}C. The soaking process was performed to detoxify the tuber through the removal of free cyanide in the fresh root. After 72 hours the cassava slices were placed on an absorbent to remove the unbound water. The slices were then dried on the transparent PET plastic film on the dryer.

Measurements

The moisture content and weight of the cassava slices, both before and after the drying operation were measured using a MB45 OHAUS Moisture Analyser (OHAUS, 2011). The OHAUS moisture analyser resulted in mass and % moisture contents readings to an accuracy of 0.01g and 0.01% respectively. The thickness of the cassava slices was measured with a digital Vernier caliper.

3.0 ANALYSIS OF EXPERIMENTAL DATA

The Moisture Ratio

The Moisture Ratio (MR) also called Dimensionless Moisture Content is an important property of drying materials when considering Drying Kinetics. It was determined from the experimental data using Equation 1.

$$MR = \frac{MC_t - MC_e}{MC_i - MC_e} \quad (1)$$

where MC_t is the moisture content of cassava after drying for time t; MC_e is the equilibrium moisture content of dried cassava and MC_i is the initial moisture content of fresh cassava all in the unit of g of water removed/g of solids.

Bulk Density (ρ_b) Determination

The bulk density of the dried cassava was determined after tapping 10g of dried cassava powder in a 25cc measuring cylinder for 5 minutes and noting the final volume using the method described by Yusuf, (2004). The bulk density will then be calculated using equation 2.

$$\rho_b = \frac{M_s}{V_s} \quad (2)$$

where ρ_b is bulk density, M_s is mass of sample used in grams and V_s is volume in ml occupied by the sample in the measuring cylinder.

Rehydration Ratio (RR) Determination

The ability of the dried product to rehydration is an important quality. The rehydration ratio was determined

by soaking the dried cassava in water with a weight ratio greater the 1 to 6 as recommended by Baron Spices and Seasonings (2014). The experiments were repeated by increasing the soaking time. In each instance the mass of the rehydrated solid was then measured and the rehydration ratio determined using equation 3.

$$RR = \frac{M_r}{M_d} \qquad (3)$$

where, M_r is the mass of the rehydrated solid and M_d is the mass of the dry sample.

Graphical Presentation

The drying curve, the drying rate curve, the Krischer curve, the experimental vs. predicted moisture content plot, the rehydration data curve, the effective moisture diffusivity plot will be all be graphical presented from the experimental data.

Determination of the Best Drying Models

The drying models were evaluated by performing Regression analysis using the drying data and the models listed in Table 1. The model were chosen to be the best if the value of the Coefficient of determination (R^2) was close to unity and Mean Bias Error (MBE), Chi-square ($\chi 2$), Root Mean Square Error (RMSE) values are minimum (Akpinar, 2010; Tunde-Akintunde and Afon, 2010; Gikuru and EL-Mesery, 2014; John *et al.,* 2014). The value of correlation coefficient (R^2) was determined using equation 4

$$R^2 = \frac{\sum_{i-1}^{N}(MR_i - MR_{prev,i}).\sum_{i=1}^{N}(MR_i - MR_{\exp,i})}{\sqrt{\left[\sum_{i-1}^{N}(MR_i - MR_{pre,i}{}^2)\right]\left[\sum (MR_i - MR_{\exp,i}{}^2)\right]}} \quad 4$$

The Root Mean Square Error (RMSE) was determined using equation 5

$$RMSE = \left[\frac{1}{N}\sum_{i=1}^{N}(MR_{pre,i} - MR_{\exp,i})^2\right]^{1/2} \quad 5$$

Chi-square ($\chi 2$) was determined using equation 6

$$\chi 2 = \frac{\sum_{i=1}^{N}(MR_{\exp,i} - MR_{pre,i})^2}{N - n} \qquad (6)$$

Mean Bias Error (MBE) was determined using equation 7

$$MBE = \left[\frac{1}{N}\sum_{i=1}^{N}(MR_{pre,i} - MR_{\exp,i})\right] \qquad (7)$$

where, N is the total number of observations, n is the number of model parameters, MR denotes the moisture ratio; $MR_{pre,i}$ and $MR_{\exp,i}$ is the predicted and experimental moisture ratio at *i*th observation respectively.

The thin-layer drying models to which the drying data were fitted are presented in Table. 1. The parametric coefficients of each model were determined using the using a Datafit 9.1 data regression software developed by Oakdale Engineering, Oakdale, (2014) PA USA. The software used the Levenberg-Marquardt Method for Nonlinear Least Square Problems in determining its solution, (Gavin, 2013). Table 2 presents the parametric constants, the Mean Bias Error (MBE), the coefficient of determination (R^2), the Root Mean Square Error (RMSE), and the Chi-square ($\chi 2$) values for each model.

Table 1: Thin Layer Drying Models

S/N	Model
1	MR = exp (-k.t) Newton Model (Ayensu, 1997)
2	MR =exp ($-$k.t^n) Page Model (Page, 1949)
3	MR = exp ($-$(k.t)^n) Modified Page Model (Ozdemir and Devres,1999)
.l4	MR =a.exp (-k.t) Henderson and Pabis Model (Henderson and Pabis, 1961)
5	MR =a.exp (-k.t)+ b.exp (-g.t)+c.exp (-h.t) Modified Henderson and Pabis Model (Karathanos,1999)
6	MR =a.exp (-k.t) + c Logarithmic Model (Togrul and Pehlivan, 2003)
7	MR =a.exp ($-$k$_0$.t) + b exp ($-$k$_1$.t) Two term Model (Madamba, 1996)
8	MR =a.exp (-k.t) + (1-a) exp (-k.a.t) Two term exponential Model (Sharaf-Elden *et al.*,1980)
9	MR = 1+ a.t + b.t^2 Wang and Singh Model (Wang and Singh, 1978)
10	MR = a.exp (-k.t) + (1-a).exp (-k.b.t) Diffusion Approach Model (Demir *et al.*, 2007)
11	MR = a.exp (-k.t) + (1-a).exp (-g.t) Verma *et al*. Model (Verma *et al*., 1985)
12	MR = exp (-k$_1$.t/1+k$_2$.t) Aghbashlo *et al*. Model (Aghbashlo *et al*., 2009)
13	MR = a.exp ($-$k.t^n) + b.t Midilli *et al*. Model (Midilli *et al*., 2002)
14	MR = a.exp (-b.t^c) + d.t^2 + e.t + f Haghi and Ghanadzadeh Model (Haghi and Ghanadzadeh, 2005)

Table 1: Thin Layer Drying Models

15	MR = a.exp[-ct/L^2] Simplified Fick's diffusion (SFFD) equation (Diamante and Munro, 1991)
16	MR = exp[-k(t/L^2)^n] Modified Page equation –II (Diamante and Munro, 1993)
17	MR = exp(-(t/a)^b) Weibull (Corzo *et al*., 2008)

Effective Moisture Diffusivity Determination

Fick's second equation of diffusion is used to estimate the Effective Moisture Diffusivity, D_{eff} ; the equation as presented by Crank is given in Equation 8 (Crank, 1975). Crank (1975) considered the slices to be of constant moisture diffusivity, infinite slab geometry, and a uniform initial moisture distribution. The Crank equation, Equation 8, for slabs involved a series of exponents that can be simplified to Equation 9 because the first term was used for long drying times (Lopez *et al.*, 2000). Further detailed discussions are available in literature (Jena and Das, 2007; Taheri-Garavand *et al*., 2011).

$$MR = \frac{8}{\pi^2}\sum_{n=1}^{\infty}\frac{1}{(2n-1)^2}\exp\left(-\frac{(2n-1)^2\pi^2 D_{eff}\,t}{4L^2}\right) \quad 8$$

$$MR = \frac{8}{\pi^2}\exp\left(-\frac{\pi^2 D_{eff}\,t}{4L^2}\right) \quad 9$$

Where,

MR is the moisture ratio, D_{eff} (m^2s^{-1}) is the effective moisture diffusivity, *L* (m) is the sample thickness and *t* is the drying time (s).

A plot of $\ln(MR)$ against time gave a slope k_d from which D_{eff} was obtained according to the equation 10

$$k_d = \frac{\pi^2 D_{eff}}{4L^2} \quad 10$$

4.0 RESULTS AND DISCUSSION

The initial moisture content of the cassava slices was found to be around 65% on a dry basis (db). The experimental data of the drying process were fitted to 17 thin layer mathematical drying models frequently used in food drying (see Table 1). The regression results presented in Table 2 showed that the Haghi and Ghanadzadeh (2005) thin layer drying model gave the lowest value of Mean Bias Error (MBE), Chi-square (χ2), Root Mean Square Error (RMSE) values compared to the other 16 models; it also had the highest coefficient of determination (R^2) value. The values where R^2, MBE, RMSE, and χ^2 values determined, were 0.998434, -8.83x10^{-6}, 0.00420 and 0.000441 respectively. The Haghi and Ghanadzadeh (2005) thin layer drying model's fitness was further validated by plotting the experimental moisture content values against the predicted moisture content values as presented in Fig. 2. The experimental and predicted moisture content values varied around a straight line with a slope of approximately one and intercept of almost zero.

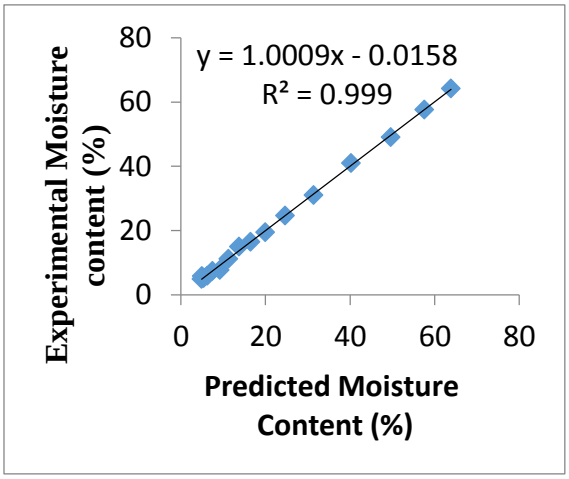

Fig. 2 Haghi and Ghanadzadeh model Fitness of experimental moisture content values *vs.* the predicted moisture content

This clearly demonstrated that the Haghi and Ghanadzadeh (2005) model could be used to explain the thin layer drying behaviour of cassava slices. Inspection of the Moisture content *vs* Drying time plot also showed that the moisture content of the cassava slices decreased with increase in drying time to about 5% (db) after a drying time of 210 minutes (Fig. 3).

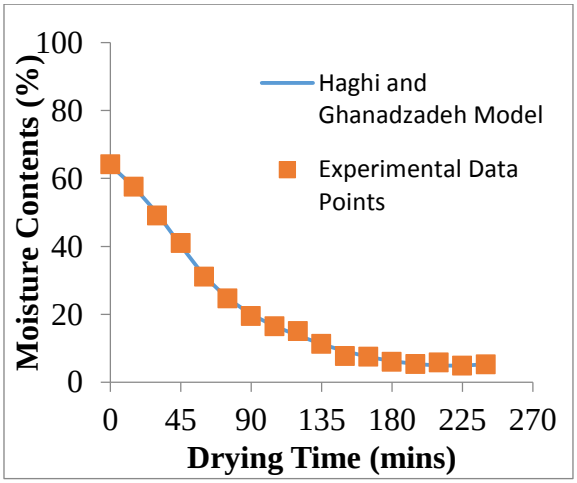

Fig. 3 Drying curve: Moisture content *vs.* Drying time

The drying rate *vs.* drying time plot was also obtained (Fig. 4). The drying rate data was obtained by

differentiating the Haghi and Ghanadzadeh model equation obtained from the experimentally data points. Fig. 4 showed first an increasing drying rate drying period, in which there was an initial rapid increase in the drying rate. The rate increased from about 0.4 kg/kg/min to a peak value of 0.6 kg/kg/min in about 60 minutes. The peak drying rate was only or a few minutes after which the drying rate fell, the falling rate period. The falling rate drying period occurs in two stages. First is the unsaturated drying period where the surface was drying out and then the saturated drying period where moisture has to move through the aggregate before being released; this saturated drying period is slower.

The Krischer curve, i.e. the drying rate *vs* moisture content plot for the cassava slices is shown in Fig. 5. The plot is a combination of the Drying curve and the Drying rate curve. Fig. 5 shows that the drying rate (right to left) increases from its initial value when the cassava slice is fresh, it reaches a peak value (constant rate period) and then falls (falling rate period). As illustrated, the constant rate period is just for a few minutes.

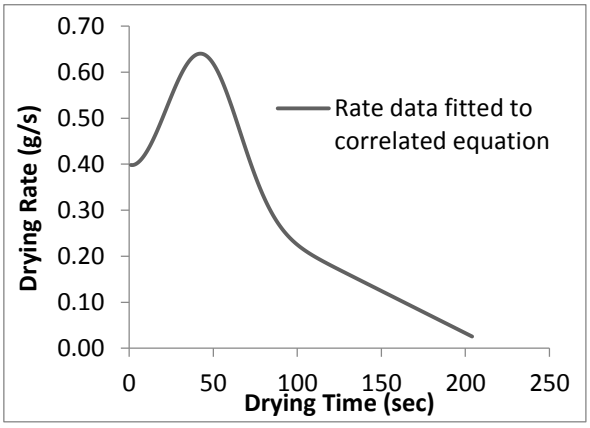

Fig. 4 Drying Rate curve: Drying rate - Drying time

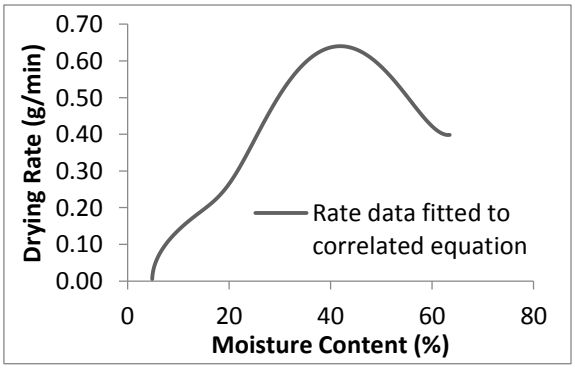

Fig 5. Krischer curve: Drying rate – Moisture Content

The rehydration ratio of the cassava taken at different time interval is shown in Fig. 6. The Rehydration Ratio increased to about 3.10 in the first 60 minutes, the slightly increases to a steady value of 3.22 after about 120 minutes.

The bulk density was determined to be 0.62 g/cc. This is consistent with values obtained in literature (Okolie et al., 2012; Ekwu, 2011). A plot of $-\ln(MR)$ *vs* drying time is shown in Fig. 7. The line and the linear relationship that best fitted the data ere also shown on the figure. From the slope, k_d of the line, the effective moisture diffusivity D_{eff} was obtained, according to equation 11. For 3 mm thick cassava slices, a value of 4.94673x 10^{-6} m^2/s is obtained as the effective moisture diffusivity.

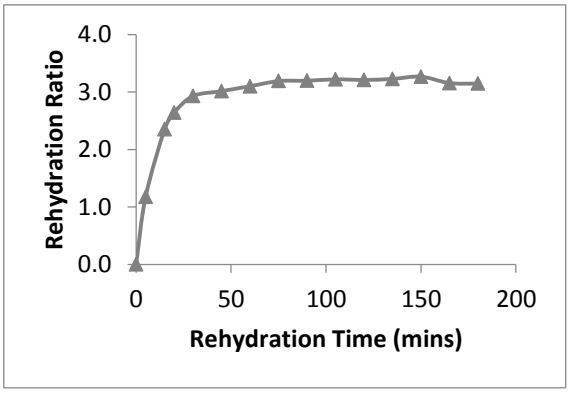

Fig. 6 Rehydration Ratio vs Rehydration Time

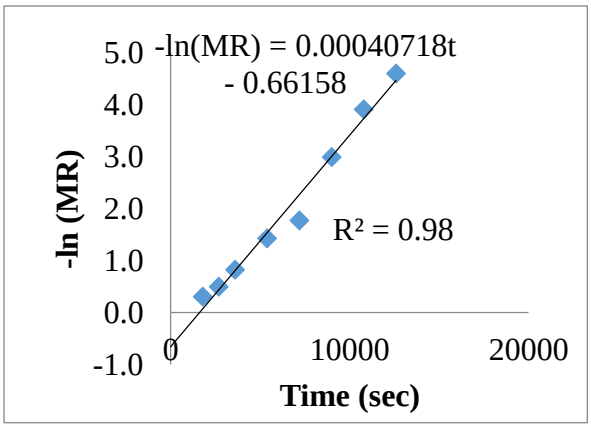

Fig. 7 – $\ln(MR)$ *vs* time plot - Estimation of Moisture Diffusivity Coefficient

5.0 CONCLUSION

The freshly prepared Cassava slices 3 mm thick had a moisture content of approximately 65% (dry basis). The Haghi and Ghanadzadeh thin layer drying model with a coefficient of determination R^2 value of 0.998 best predicted the drying kinetics among the 17 models tested. The drying rate for the cassava slices reached a maximum value after about 50 minutes after drying began. The Rehydration Ratio increased to a steady value of about 3.22 after about 120 minutes. The bulk density was determined to be 0.62 g/cc. The effective

moisture diffusivity was found to be 4.94673 x 10^{-6} m^2/s. Experimental data established that the cassava slices could be dried to moisture content of below 5% within 210 minutes. This time is significantly less than the 3 to 5 days required by the traditional sun drying methods.

Table 2: Constant and Coefficient Obtained by Fitting Data to the Various Thin Layer Models

No.	Model Name	Polymath Constants		R^2	MBE	$\chi 2$	RMSE
1	Newton	k = 0.01419		0.9761085	0.007008	0.002992	0.0164088
2	Page	k = 0.00274	n = 1.37990	0.9976221	0.000845264	0.000334973	0.0051767
3	Modified Page	k = 0.01391	n = 1.379611	0.9976221	0.000849	0.000334972	0.0051767
4	Henderson and Pabis	a = 1.05820	k = 0.01497	0.9800387	0.013378	0.002811942	0.0149985
5	Modified Henderson and Pabis	a = 0.35697 g = 0.01497 b = 0.35697	c = 0.34425 h = 0.01496 k = 0.01496	0.9800387	0.01337745	0.005623884	0.0149985
6	Logarithmic / Yagcioglu *et al.*	a = 1.13115 c = -0.09563	k = 0.01207	0.9899756	-1.10131E-06	0.00161388	0.0106288
7	Two term	a = 0.89604 b = 0.16216	k = 0.01497	0.9800387	0.013372	0.003749256	0.0149985
8	Two term exponential	a = 1.964319	k = 0.0220851	0.9974359	0.002954	0.0003612	0.0053755
9	Wang and Singh	a = -0.01020	b = 2.566E-05	0.9933824	0.000386	0.000932225	0.0086358
10	Diffusion Approach	a = -3.24477 b = 0.78729	k = 0.03243	0.9975813	0.002052	0.000389399	0.0052209
11	Verma *et al.*	a = -0.06132 k = 0.74118	g = 0.01490	0.9833247	0.009363	0.00268462	0.0137085
12	Aghbashlo *et al.*	k1 = 0.01021	k = -0.00318	0.9958626	-0.00305	0.00058284	0.0068284
13	Midilli *et al.*	k = 0.00295 n = 1.3612	a = 1.00188 b = -2.74E-05	0.997683	-4.96205E-05	0.0004352	0.00511
14	Haghi and Ghanadzadeh	a = 0.26440 c = 2.70342 e = -0.00674	b = 2.23E-05 d = 1.55E-05 f = 0.73030	0.998434	-8.82891E-06	0.000441201	0.004201
15	Simplified Fick's diffusion (SFFD) eqn.	a = 1.058199	c = 0.13469	0.9800387	0.013378	0.002811942	0.0149985
16	Modified Page equation -II	k = 0.05690	n = 1.37967	0.9976221	0.000848	0.000334972	0.0051767
17	Weibull	a = 71.8679	b = 1.37961	0.9976221	0.000849	0.000334972	0.0051767

REFERENCES

Aghbashlo, M., Kianmehr, M. H., Khani, S, and Ghasemi, M., (2009), Mathematical Modelling of Thin-Layer Drying of Carrot, *Int. Agrophysics*, Vol. 23, pp 313-317.

Akpinar, E. K., (2010), Drying of Mint Leaves in a Solar Dryer and Under Open Sun: Modelling, Performance Analyses, Energy Conversion and Management, Vol. 51, Iss. 12, p 2407–2418, 2010. DOI: 10.1016/j.enconman.2010.05.005.

Ayankunbi, M., Keshinro, O. and Egele, P., (1991), Effects of Method of Preparation on Nutrients Composition of Some Cassava Food Products: Gari (Eba), Lafun and Fufu, Food Chemistry, 41: 349-354.

Ayensu, A., (1997), Dehydration of Food Crops Using a Solar Dryer With Convective Heat Flow, Solar Energy, Vol. 59, No. 4, pp 121-126.

Baron Spices and Seasoning, (2015), Dehydrated Onion and Garlic Products-Rehydration, Retrieved 29-09-2015 from http://www.baronspices.com/spice_handbook/rehydration.html

Cock, J. H., (1982), Cassava: A Basic Energy Source in the Tropics Science, Science 19 November 1982, Vol. 218, No. 4574, pp. 755-762.

Cock, J. H., (1985), Cassava: New Potential for a Neglected Crop, Westview Press, Boulder, CO, USA. 191 p. (IADS Development-Oriented Literature Series).

Corzo, O., Bracho, N., Pereira, A., and Vasquez, A., (2008), Weibull Distribution for Modeling Air Drying of Coroba Slices, LWT - Food Sci. Technol., Vol. 41, pp 2023-2028.

Crank J., (1975), *The Mathematics of Diffusion*, 2nd ed., Oxford University Press, Oxford, 104 - 106.

Demir, V., Gunhan, T., and Yagcioglu, A. K., (2007), Mathematical Modelling of Convection Drying of Green Table Olives, Biosystems Eng., 98, 47-53.

Diamante, L. M., and Munro, P. A., (1991), Mathematical Modelling of Hot Air Drying of Sweet Potato Slices, International Journal of Food Science and Technology, Vo. 26, No. 1, pp 99-109.

Diamante, L. M., and Munro, P. A., (1993), Mathematical Modelling of the Thin Layer Solar Drying Of Sweet Potato Slices, Solar Energy, Vol. 5 , No. 4, pp 271-276.

Ekwu, F. C., Ngoddy P. O. and Uvere P. O., (2011), Functional And Rheological Properties Of Cassava Flour Processed By Adaptation Of Traditional 'Abacha' Processing Technology, ISSN: 1597 JORMAR 6(1) 2011, 17 - 30 - 3204

Gavin, H., (2013), The Levenberg-Marquardt Method for Nonlinear Least Squares Curve-Fitting Problems, Department of Civil and Environmental Engineering, Duke University, Durham, NC, 27708, USA. Retrieved January 08, 2015 from http://people.duke.edu/~hpgavin/ce281/lm.pdf

Gikuru, M., and EL-Mesery, H. S., (2014), Mathematical Modelling of Thin Layer Drying Kinetics of Onion Slices Hot-air Convection, Infrared Radiation and Combined Infrared-Convection Drying, Advances in Environmental Biology, Vol. 8, No. 20, Special 2014, Pp 1-19.

Haghi, A. K. and Ghanadzadeh, H., (2005), A Study of Thermal Drying Process. Indian Journal of Chemical Technology, Vol. 12, November 2005, pp. 654-663.

Henderson, S. M. and Pabis, S., (1969), Grain Drying Theory I. Temperature Effect on Drying Coefficient, Journal of Agriculture Engineering Research, Vol. 6, Iss. 3, pp 169–174.

Jena, S. and Das H., (2007). Modelling for Vacuum Drying Characteristics of Coconut Presscake, *Journal of Food Engineering*, 79, 92-99.

John, S. G., Sangamithra, A., Veerapandian, C., Sasikala, S. and Sanju, V., (2014), Mathematical Modelling of the Thin Layer Drying of Banana Blossoms, J Nutr. Health Food Eng, 1(2), 00008.

Karathanos, V. T., (1999), Determination of Water Content of Dried Fruits by Drying Kinetics, J. Food Eng., 39, 337-344.

Lancaster, P. A., Ingram, J. S., Lim, M. Y., & Coursey, D. G., (1982), Traditional cassava-based foods: survey of processing techniques, Economic Botany, 36(1), 12-45

Lopez A., Iguaz A., Esnoz A., Virseda P., (2000), Thin-layer drying behaviour of vegetable waste from wholesale market, *Drying Technology* 18: 995–1006.

Nindo, C. I., and Tang, J., (2007), Refractance Window™ Dehydration Technology: A Novel Contact Drying Method, Drying Technology, 25: 37–48

Madamba, P. S., Driscoll, R. H. and Buckle, K. A., (1996), The Thin Layer Drying Characteristics of Garlic Slices, Journal of Food Engineering, 29: 75-97.

Marsh, K. S., (2002), How to Reduce Food Degradation with Appropriate Processing, Transportation and Packaging, International Trade Centre UNCTAD/WTO, Export Packaging Bulletin No. 2 Retrieved 30-August, 2015 from http://www.drkenmarsh.com/documents/EPB02_Reduce-Food-Degrad.pdf.

Mlingi, N. L. V., (1995), Cassava Processing and Dietary Cyanide Exposure inTanzania, Ph.D., Thesis, Faculty of Medicine, University of Uppsala, Sweeden.

Midilli, A., Kucuk, H., and Yapar, Z., (2002), A new model for single-layer drying, Drying Technol., 20(7), 1503-1513.

Oakdale Engineering, (2014), Datafit 9.1 Software (Build 9.1.32) Developed by Oakdale Engineering, 23 Tomey Road Oakdale, PA 15071 USA.

OHAUS, (2011), OHAUS Instruction Manual MB45 Moisture Analyzer, Ohaus Corporation, 7 Campus Drive, Suite 310, Parsippany, NJ 07054 USA.

Okolie, N. P.. Brai, M. N and Atoyebi, O. M., (2012), *Journal of Food Studies*, ISSN 2166-1073 2012, Vol. 1, No. 1.

Ozdemir, M., and Devres, Y. O., (1999), Thin Layer Drying Characteristics of Hazelnuts During Roasting, Journal of Food Engineering, 42: 225-233.

Page G. E., (1949), Factors Influencing the Maximum Rates of Air Drying of Shelled Corn in Thin Layer, M.Sc. Thesis, Purdue University, Lafayette, IN, USA.

Sharaf-Elden, Y. I., Blaisdell, J. L., and Hamdy, M. Y., (1980), A Model for Ear Corn Drying. Trans. ASAE, 23, 1261-1265.

Taheri-Garavand, A., Rafiee, S., & Keyhani, A. (2011).Effective moisture diffusivity and activation energy of tomato in thin layer dryer during hot air drying. *International Transaction Journal of Engineering, Management, & Applied Sciences & Technologies*, 2(2), 239-248

Thomson, T. L., Peart, P. M., and Foster, G. H., (1968), Mathematical Simulation of Corn Drying: A New Model, Transactions of the ASAE; Vol. 11, Iss. 4, pp 582-586.

Togrul, I. T. and Pehlivan, D., (2003), Modelling of Drying Kinetics of Single Apricot, J. Food Eng., Vol. 58, pp 23-32.

Tunde-Akintunde, T. Y., and Afon, A. A., (2010), Modeling of Hot-Air Drying of Pretreated Cassava Chips, *Agric Eng Int: CIGR Journal*, 2010, Vol. 12, Iss. 2, pp 34－41.

Verma, L. R., Bucklin, R. A., Endan, J. B., and Wratten, F. T., (1985), Effects of Drying Air Parameters on Rice Drying Models, *Trans. ASAE, Vol. 28, pp 296-301*.

Wang, C. Y. and Singh, R. P., (1978), A Single Layer Drying Equation for Rough Rice, ASAE paper No. 78-3001, MI, USA: St. Joseph.

Yusuf, A. B., (2004), Laboratory Manual on Food Technology, Nutrition and Dietetics for School and Industries, Department of Food Technology, College of Science and Technology, Kaduna Polytechnic, Kaduna, Kaduna State, pp. 73-79.

TRANS-ESTERIFICATION OF TOBACCO SEED OIL USING SOME AGRICULTURAL WASTES AS CATALYSTS

O. Motojesi [1], T.E. Odetoye[2]*, D.S. Ogunniyi [2]

[1] Department of Chemistry, University of Ilorin, Ilorin, Kwara State, Nigeria.

[2] Department of Chemical Engineering, University of Ilorin, Ilorin, Kwara State, Nigeria.

ABSTRACT

Fatty acid methyl esters were produced from tobacco seed oil having high free fatty acid (FFA) content (13.02%). The high FFA content of tobacco seed oil was reduced to less than 2% in a 1 hour reaction by a two-step process. The first step was acid-catalyzed esterification reaction conducted at 50 ^oC using 1% w/w H_2SO_4, 18:1 molar ratio methanol with respect to the high FFA tobacco seed oil to produce methyl ester by lowering the acid value. The second step was trans-esterification of the treated oil obtained using 6:1 methanol to oil ratio. The following catalysts: 1%w/w KOH, 2%w/w cocoa pod ash and 2%w/w rice husk ash were employed to produce fatty acids methyl esters at 65^oC. The yields for fatty acids methyl esters obtained were 96%, 94.6% and 82% in 2h for KOH, cocoa pod ash and rice husk ash catalysts respectively.

***Keywords**: Biodiesel, tobacco seed oil, trans-esterification,; cocoa pod ash; rice husk ash*

** Corresponding author. Tel: + 234-07064356000, E-mail: todetoye@yahoo.com*

1.0 INTRODUCTION

Increasing environmental consciousness has led many researchers to produce alternative fuels from renewable resources that are environmentally acceptable (Ajala *et al.,* 2015). Biodiesel is an interesting alternative fuel for diesel engines because it burns with a reduction in the emission of greenhouse gases such as CO_2 and unburned hydrocarbons when compared with fossil fuels (Balat, 2011). Biodiesel is a mixture of fatty acid methyl esters of low alkyl chain alcohol and it is normally produced by a catalytic trans-esterification reaction of vegetable oils with short chain alcohols, while producing glycerol as a by-product. Biodiesel production is well studied, especially in the use of acids or alkyl catalysts, like alkyl metal hydroxides or alkoxides and sulphuric acid (Aladetuyi *et al.,* 2014; Amos *et al.,* 2016). As a future prospective fuel, biodiesel has to compete economically with petroleum diesel fuels. One way of reducing the costs

is to use the less expensive feedstock containing fatty acids such as non-edible oils, animal fats, waste food oil and by-products of the refining vegetable oil (Balat, 2011).

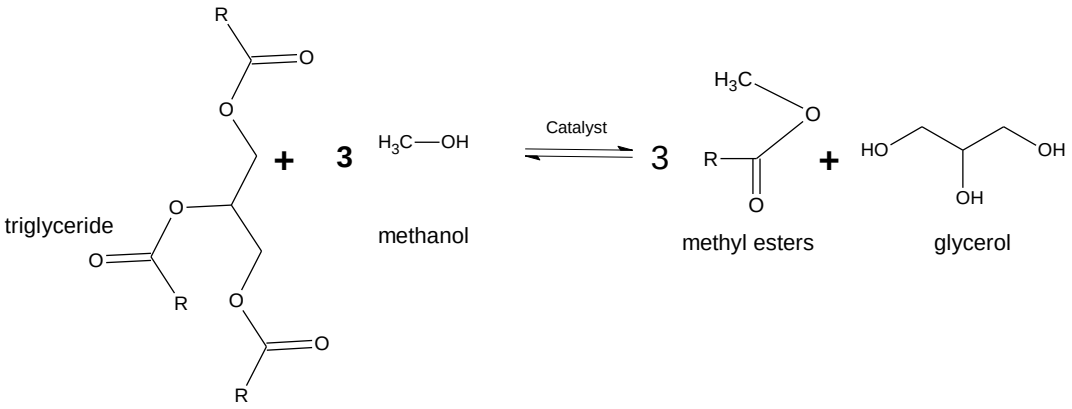

Figure 1: Trans-esterification of Vegetable Oil (Wikipedia,2016).

Tobacco seed oil is extracted from tobacco seeds which are grown in the tropical climates across the world. Oil contents, physico-chemical properties, fatty acids composition, energy values of tobacco oil have been investigated (Bekele, 2000; Giannelos *et al.*, 2002; Ogunniyi and Odetoye, 2008; Awolola *et al.*, 2010). In many cases, tobacco seed oil quality deteriorates gradually due to improper handling and inappropriate storage condition. Exposing the oil to open air and sunlight for a long period would increase the concentration of FFA significantly to relatively high level, above 1%. The presence of high FFA makes reaction difficult because of formation of soap with alkaline catalyst (Azad *et al.*, 2016). Therefore, an alternative process such as acid-catalyzed esterification followed by base trans-esterification was adopted for biodiesel production from high FFA vegetable oils such as tobacco seed oil (Giannelos *et al*,2002; Veljković *et al*, 2006; Sharma *et al*,2015; Hariram and Gowtham, 2016).

Another way of making biodiesel to compete economically with fossil fuel is by utilizing agro-waste ashes such as cocoa pod ash and rice husk ash as catalyst for trans-esterification instead of employing high cost conventional alkaline catalysts (KOH, NaOH). Chemical analysis of liquid extract from the ashes indicated that cocoa pod ash contains 56.37wt% of potassium compound as the main ingredient (Kalderis *et al*, 2008; Amos *et al.*, 2016) while, rice husk ash contains 88.4wt% of silica as the main ingredient (Taiwo and Osinowo, 2000).

The aim of this research work is to produce biodiesel from tobacco seed oil having relatively high FFA

(13.02%). First, the acid-catalyzed esterification process (pretreatment process) for reducing the FFA content of tobacco seed oil to below 2% was carried out and second, attention was focused on optimizing the reaction conditions for weight ratio of each catalyst (cocoa pod ash, rice husk ash and KOH) to oil as catalysts for trans-esterification at 65^{o}C.

2.0 MATERIALS AND METHODS

2.1 MATERIALS

Reagent grade potassium hydroxide, n-hexane, methanol, sulphuric acid were obtained from commercial sources. The n-hexane and methanol were distilled before use. The tobacco seed oil was extracted using Soxhlet extractor and hexane as solvent for 4h and the extract was concentrated using rotary vacuum evaporator, dried

2.2 METHODS

2.2.1 Analysis of Tobacco Seed Oil

The fatty acid composition of tobacco seed oil was determined by Agilent 6890N gas chromatograph with a mass selective 5973 series detector. The tobacco seed oil was also analyzed for physical and chemical properties using ASTM standard methods. The properties determined were density, specific gravity, viscosity, acid value, iodine value and saponification value.

2.2.2 Catalyst Preparation

Cocoa pod was dried and charred. The char was ashed in muffle furnace at 600^{o}C for 35 minutes. This step was repeated until a constant weight was obtained in accordance with instruction in ASTM D482-80, 1983. Rice husk ash (RHA) was prepared following the same procedures as in the case of cocoa pod ash (CPA). The ashes were sieved to 0.8mm particle sizes and analyzed using Atomic Absorption Spectrometer (AAS Bulk 200). These ashes were used as catalysts in the trans-esterification processes.

2.2.3 Catalytic Experiment

Pre-treatment of High FFA Tobacco Seed Oil with Acid-catalyzed Esterification.

The objective of this step was to reduce the FFA contents of the crude tobacco seed oil to barest minimum (<4%FFA) for biodiesel production via acid catalyzed esterification. 5g (0.0058 moles) of crude tobacco seed oil (CTSO) was poured into 25ml quick fit round bottom flask and heated to 50^{o}C. 0.05g concentrated H_2SO_4 acid was mixed with 0.56 g (0.0175 moles) of methanol and heated to 50^{o}C in a beaker. The methanol/ H_2SO_4 (3:1) mixture was added to the heated oil and the reaction was allowed to proceed for 1 h with occasional shaking. After 1 h of reaction, the mixture was allowed to settle for 2 h and the upper layer (which contains methanol-water and gums) was removed. The acid value of the

bottom layer (oil) was determined and from it, the %FFA was calculated. The above procedures were repeated by varying the methanol to oil ratios (namely 6:1, 9:1, 12:1, 15:1, 18:1 and 21:1). Optimum conditions having the lowest acid value was used for the main trans-esterification.

Trans-esterification Process

5g (0.0058moles) of pretreated oil obtained from acid-catalyzed esterification was poured into 25ml quick fits round bottom flask (reaction vessel) and heated to 50^{o}C. 0.05g of KOH catalyst (1%w/w of oil) was dissolved in 1.12g (0.035moles) of methanol. The mixture of methanol and catalyst was heated to 50^{o}C prior to addition and then added to the heated oil. The reaction mixture (methanol/catalyst/oil) was stirred and heated at 65^{o}C for 2h with azeotropic removal of water formed during the reaction using Dean and Stark apparatus. The mixture was allowed to settle overnight for the glycerol layer (bottom layer) to separate from the methyl esters layer of fatty acids (upper layer) using separating funnel. The fatty acid methyl ester was washed with warm distilled water to remove the excess methanol, catalyst and traces of glycerol. The above procedures were repeated by varying the catalyst concentrations (1-4% KOH, cocoa pod ash, rice husk ash) to determine the optimum conditions for the production of methyl ester

Analysis of Biodiesel

The ester content of tobacco seed methyl esters produced were analyzed on 6890N Agilent Gas Chromatograph with a Mass Selective Detector 5973 series, following the conditions stated in section 2.2 and the fuel-related properties were determined according to ASTM D6751 standards.

3.0 RESULTS AND DISCUSSION

3.1 Analysis of Tobacco Seed Oil

The yield of tobacco seed oil obtained using Soxhlet extractor and hexane as solvent was 33.16%. The value falls within the range (33-40%) obtained in literature (Stanisavljević *et al.,* 2009). Figure 1 presents the GC chromatogram of tobacco seed oil while the fatty acid composition is as shown in Table 1. The results obtained were similar to literature values (Bekele, 2000; Giannelos *et al*., 2002) which indicated that the oil was unsaturated.

Linoleic (18:2) and oleic (18:1) were the two most abundant unsaturated fatty acids (74.75 and 13.34wt% respectively) as they constitute 87.88% of tobacco seed oil by weight. Hence, the seed oil is classified as linoleic oil, and also classified as semi-drying oil. The high degree of unsaturation of tobacco seed oil could render the oil susceptible to autoxidation, resulting in degradation of the oil (Stanisavljević *et al.,* 2009). Autoxidation is due to the reaction of double bonds present in the chains of unsaturated fatty acid compounds with oxygen. It was reported that degradation of unsaturated vegetable oils resulted in relatively higher concentration of %FFA compared to saturated vegetable oils (Hanny and Shizuko, 2007).

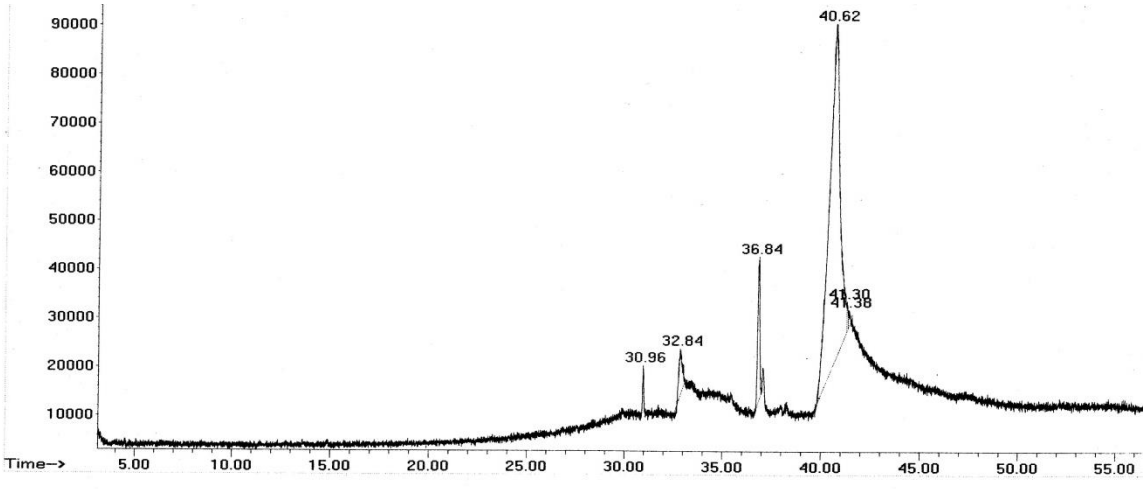

Figure 1: GC Chromatogram of Tobacco Seed Oil

Table 1: Fatty Acid Composition of Tobacco Seed Oil

Fatty acid	Formula	Systemic name	Structure	Giannelos *et al*, 2002	Result obtained wt %
Palmitic	$C_{16}H_{32}O_2$	Hexadecanoic	16:0	10.96	9.26
Stearic	$C_{18}H_{36}O_2$	Octadecanoic	18:0	3.34	2.85
Oleic	$C_{18}H_{34}O_2$	Cis-9-Octadecenoic	18:1	14.54	13.13
Linoleic	$C_{18}H_{32}O_2$	Cis-9,cis-12-Octadecedienoic	18:2	69.49	74.75

The summary of physico-chemical properties of tobacco seed oil were listed in Table 2. Most of the values obtained were slightly different from the literature values which indicated that differences for

the same raw material may exist in different geographical regions. The high free fatty acid content of tobacco seed oil may be due to previous storage process which may facilitate various chemical reactions such as hydrolysis and oxidation.

Table 2: Physico-Chemical Properties of Tobacco Seed Oil

Properties	Literature values			Result obtained
	Akehurst (1981)	Giannelos et al. (2002)	Odetoye (2003)	
Density (g/cm^3) 32^{o}C	NR	NR	0.9083	0.9017
Kinematic viscosity (cS) at 40^{o}C	NR	27.70	NR	32.48
Specific gravity 32^{o}C	0.945-0.950	0.9175	NR	0.9124
Acid value (mg KOH/g)	25.95	NR	26.37	26.09
Saponification value (mg KOH/g)	228.60	193	212.06	204.30
Iodine value (gI/100g)	170-180	135	161.94	152.37
Free fatty acid (%)	NR	NR	NR	13.02

NR = recorded

3.2 Chemical Analysis of the Cocoa Pod and Rice Husk Ash

The metal compositions (ppm) of CPA and RHA determined by AAS Bulk 200 were presented in Table 3. These were in agreement with the results of Taiwo and Osinowo (2000) and Kalderis *et al*. (2008) and Amos *et al*. (2016).

Table 3: Concentration (ppm) of Metals Present in Cocoa Pod and Rice Husk Ash.

Metal	Cocoa pod ash		Rice husk ash	
	This Study	Literature Value (Taiwo and Osinowo, 2001)	This Study	Literature Value (Kalderis et al,, 2008)
Potassium (K)	13.05	20.50	3.240	2.51
Sodium (Na)	6.65	8.00	1.748	1.75
Iron (Fe)	ND	NR	0.053	0.2
Magnesium (Mg)	ND	NR	1.175	0.12-1.96
Calcium (Ca)	ND	NR	2.325	2.61
Aluminium (Al)	ND	NR	0.009	0.36

ND =Not determined, NR = Not reported

3.3 Catalytic Experiment

3.3.1 Two-step Process.

Pretreatment of high FFA tobacco seed oil with acid-catalyzed esterification

The effect of methanol/oil ratios on acid values and FFA of the mixtures after one hour reaction is shown in Table 4. The Table indicated that the FFA concentration was influenced by the quantity of methanol. The FFA concentration reduced from 13.02 to 1.67 using 3.36g of methanol (corresponding to 18:1 molar ratio of methanol to oil). Increasing the methanol amount beyond 3.36g has no significant effect on the FFA concentration reduction. The optimum methanol-to-oil ratio was 18:1 or 67.2%w/w and the FFA concentration was less than 2% and acid value was 3.36mg KOH/g. The overall process showed that the acid pretreatment step resulted in significant reduction of the acid value and % FFA in the oil.

Table 4: Influence of Methanol on Acid Value and FFA of Tobacco Seed Oil in Acid-Catalyzed Pretreatment Stage.

Methanol/Oil	Acid values mg KOH/g	% FFA
3:1	21.24	10.62
6:1	9.62	4.80
9:1	6.22	3.11
12:1	4.16	2.07
15:1	3.46	1.72
18:1	3.36	1.67
P	3.36	1.67

3.3.2 Trans-esterification Process

Experiments in which 2% CPA, RHA and 1% KOH were used as catalysts gave the best phase separations and the methyl ester obtained in each case was weighed to determine the percentage yield. The qualities of biodiesels produced were also analyzed using GC-MS. The yield obtained is shown in Table 5.

Table 5: Calculated Percentage Yields of Methyl Esters from Different Catalysts.

Catalyst	**Yield (%)***
Cocoa pod ash	94.6
Rice husk ash	82.0
KOH	96.0

*Percentage of the recovered methyl esters after 2 h of trans-esterification per initial weight of tobacco seed oil.

Figures 2, 3 and 4 showed the GC chromatograms of biodiesel from 2% CPA, 2%RHA and 1% KOH respectively. Figures 2 and 4 were similar and thus, showing the similarity in the quality of the biodiesels produced in both cases. RHA incorporated impurities into the final biodiesel as indicated in Figure 3.

3.3.3 Fuel-Related Properties of Tobacco Biodiesel

The properties of tobacco seed oil methyl ester (TME) were presented in Table 7.

Table 7: Fuel-Related Properties of Tobacco Seed Oil Methyl Esters (TME) from different Catalysts.

Property	Cocoa Pod Ash TME	Rice Husk Ash TME	KOH TME	ASTM Standard	Test Method
Acid value (mgKOH/g)	0.68	0.89	0.68	0.80 max	ASTM D974
Flash point (^{o}C)	178	198	174	100 min	ASTM D93
Ash content (wt%)	0.0017	0.0063	0.0011	0.020 max	ASTM D874
Kinematic viscosity (cS) 40^{o}C	5.63	8.27	4.86	1.9-6.0	ASTM D445

Most of the fuel related properties determined fell within ASTM specification for biodiesel, except the acid and viscosity values of the rice husk ash TME which were higher than the standard. The relatively higher acid and viscosity values may be attributed to the presence of impurities incorporated by the catalyst into the final biodiesel. However, the flash points of all the methyl esters produced fell within biodiesel standards, the flash point values which were also higher than that of conventional diesel confirmed that the biodiesel as a safe fuel.

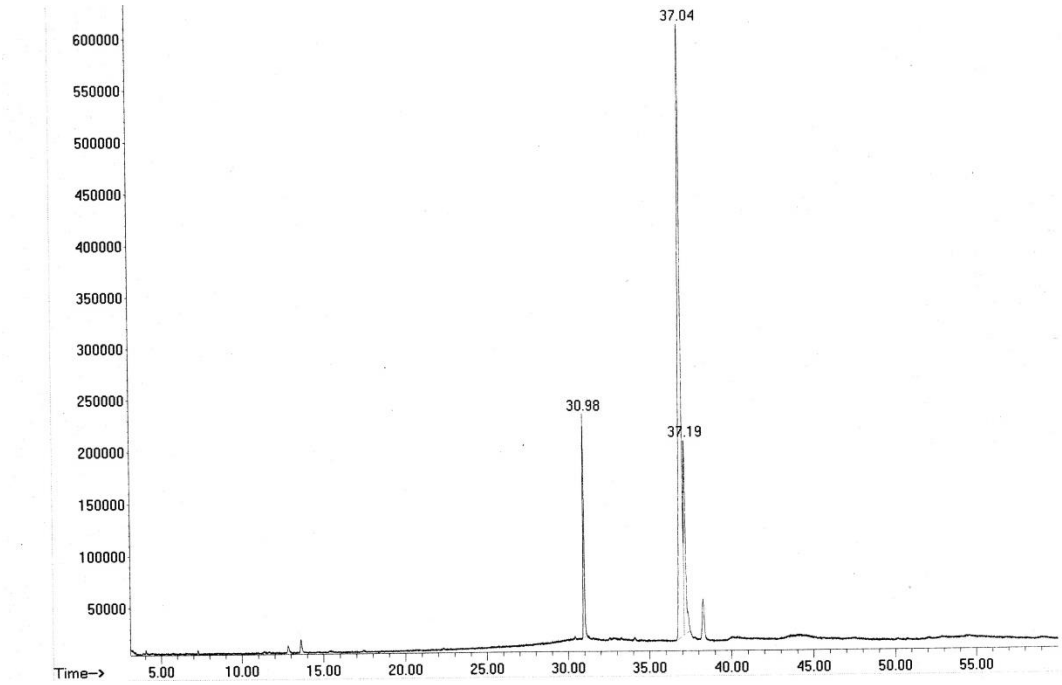

Figure 2: GC Chromatogram of 2% Cocoa Pod Ash (CPA) Biodiesel

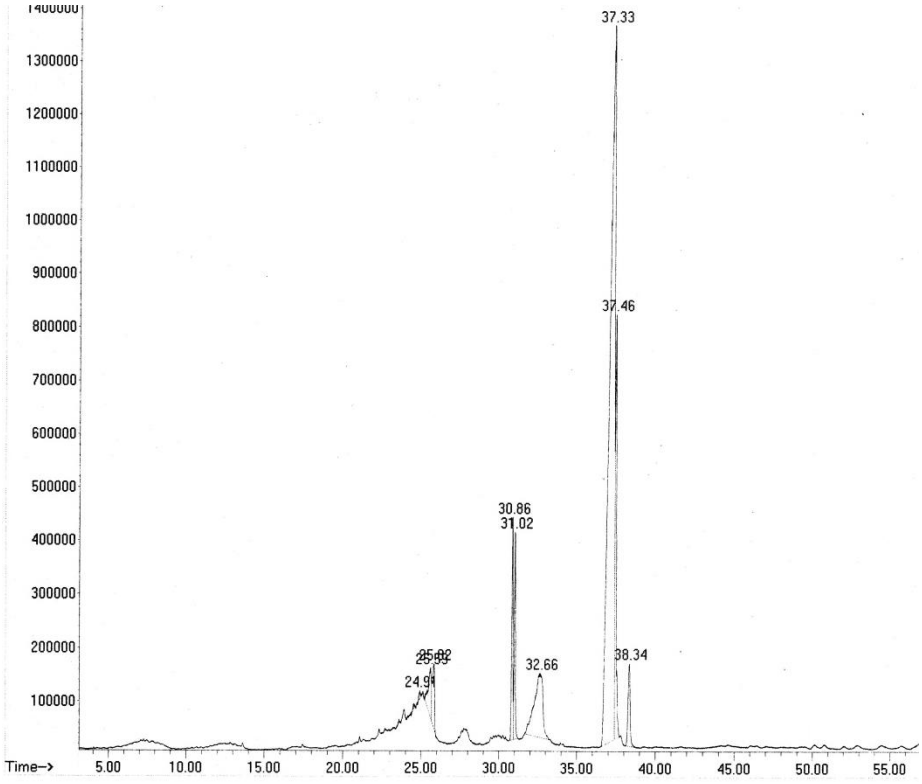

Figure 3: GC Chromatogram of 2% Rice Husk Ash (RHA) Biodiesel

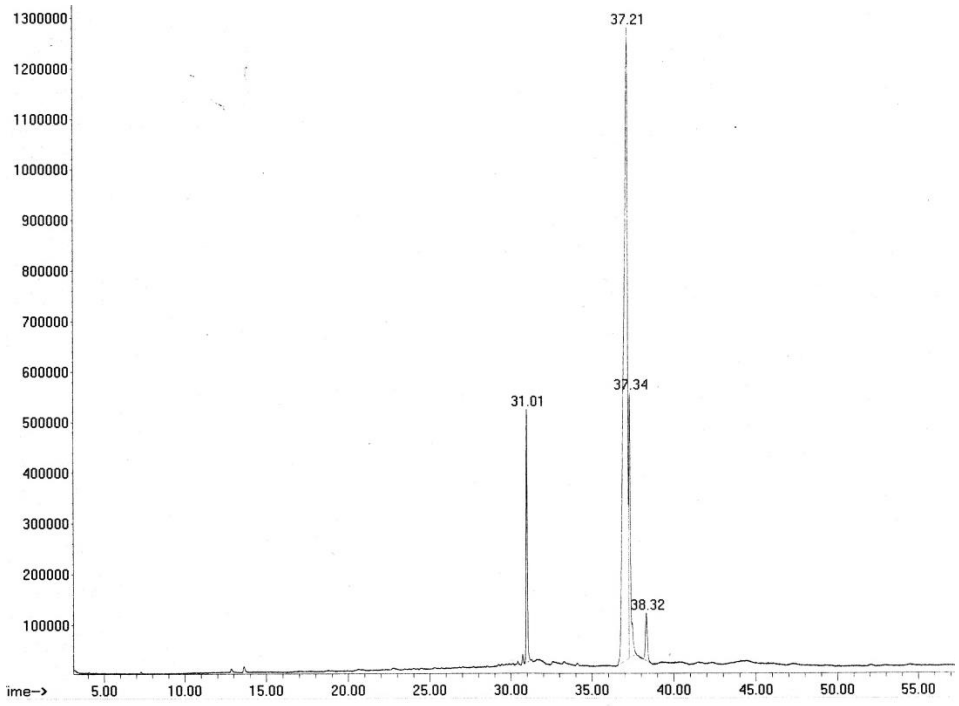

Figure 4: GC Chromatogram of 1% Potassium Hydroxide (KOH) Biodiesel

4.0 CONCLUSION

Cocoa pod ash, when used as a catalyst at 2% w/w produced methyl ester yield of 94.6% which was comparable to the yield (96%) obtained using 1%w/w KOH conventional catalyst. Rice husk ash-based catalyst gave the lowest methyl ester yield of 82%. Cocoa pod ash-based catalyst was found to produce neater biodiesel compared to the rice husk ash-based catalyst. Therefore, cocoa pod ash (with a relatively high content of potassium) is suitable as a direct substitute for conventional KOH catalyst in industrial production of neat biodiesel. The properties of biodiesel produced from cocoa pod ash and KOH in this study were similar to that of the ASTM standard and thus, suggesting their usefulness. Tobacco seeds, rich in oil, are potential valuable renewable raw material for biodiesel production. Ashes of agricultural residues such as cocoa pod ash can be utilized as cheap, bio-based alternative to conventional catalyst like KOH.

REFERENCES

1. Aladetuyi A, Olatunji G.A., Ogunniyi D.S., Odetoye T.E., Oguntoye S.O.(2014) Production and characterization of biodiesel using palm kernel oil, fresh and recovered from spent bleaching earth, *Biofuel Research Journal* 1(4): 134 -138.
2. Ajala O.E., Aberuagba F., Odetoye T.E. and Ajala, A.M. (2015) Biodiesel : Sustainable energy replacement for petroleum based diesel fuel - A review, ChemBioEng Reviews, 2(1): 1-13.
3. Amos O, Ogunniyi, D.S. and Odetoye T.E. (2016) Production of Biodiesel from *Parinari polyandra* B. Seed Oil using Bio-Based Catalysts, Nigerian journal of Technological Development, 13 (1), 26-30.
4. ASTM 1983: "Petroleum Products, Lubricants and Fossil Fuels", Annual Book of ASTM Standards, Vol.05.01, pp 277-279.
5. Balat, M (2011). Potential alternatives to edible oils for biodiesel production - A review of current work. Energy Conservation Management. 52(2), 1479-1492
6. Awolola V.G, Ogunniyi D.S, Oluwaniyi O.O. (2010). Refining, modification and characterization of tobacco seed oil for improved potentials for industrial use. Nig. J. Pure & App.Sci.Vo:2168-2174
7. Azad A.K., Rasul MG, Khan M.M.K., Sharma F.C., Mofijur M., Bhuiya, M.M.K. (2016)Prospects, feedstock and challenges of biodiesel production from beauty leaf oil and castor oil: Non –edible oil sources in Australia , Renewable and sustainable energy Reviews,302-318.
8. Bekele,E "Nicotiana tabacum L. Seed Oil" http://plantbreeding.boku.ac.at/oilcrops/eshetu.html; 15th August, 2016.
9. Giannelos P.N., Zannikos, S., Stournas S., Lois, E., Anastopoulus, G.(2002) Tobacco seed oil as an alternative fuel properties: Physical and Chemical properties. Industrial crops and products, 16; 1-9.
10. Hanny, J and Shizuko, H. (2007) Biodiesel Production from Crude *Jatropha Curcas L* Seed Oil with High content of Free Fatty Acids Bioresource Technology 99, 1716-1721
11. Hariram V and Gowtham R. A. (2016) Extraction of Tobacco (Nicotiana tabacum L.) seed oil and Biodiesel preparation through two stage transesterification, Research Journal of Pharmaceutical, Biological and Chemical Sciences , 7(2), 978-983.
12. Kalderis D; Bethanis S.; Paraskeva P. and Diamadopoulos E., (2008). Production of activated carbon from bagasses and rice husk by a single stage chemical activation method at low retention times. Bioresour. Technol., 99, 6809- 6816.
13. Ogunniyi, D.S. and Odetoye, T.E (2008) Preparation and Evaluation of Tobacco Seed Oil-Modified Alkyd Resins, *Bioresource Technology*, 99, 1300-1304.
14. Stanisavljević I, Veličković D, Todorović Z, Lazić M, Veljković V (2009). Comparison of techniques for extraction of tobacco seed oil. European Journal of Lipid Science and Technology.Vol.111. Issue 5: 513-518
15. Taiwo E.O and Osinowo F.A.O (2001) "Evaluation of Various Agro-wastes for Traditional Black Soap Production" Bioresource Technology 79, Pp 95-97
16. Veljković V.B., Lakićević S.H., Lazic M.L. , Stamenković O.S. (2006) Biodiesel production from tobacco seed oil with a high content of free fatty acid, Fuel, 85, 2671 – 2675
17. Wikipedia. (2016) "Biodiesel production" https://en.wikipedia.org/wiki/Biodiesel_production accessed on 15th August, 2016

METH-ETHANOLYSIS OF CASTOR OILTO PRODUCE BIODIESEL AND ITS BLENDS WITH PETROLEUM DIESEL

L.O. Oyekunle[1], A. Jaiyeola[2] and Idowu Adeyinka Adegbite[3]

[1]Department of Petroleum Engineering, Covenant University, Canaanland, Ota, Ogun State, Nigeria
[2]Department of Chemical and Petroleum Engineering, University of Lagos, Akoka - Yaba, Lagos, Nigeria.
[3]Bioresources Development Centre, National Biotechnology Development Agency, Owode-Yewa, Ogun State, Nigeria

ABSTRACT

Biodiesel is an alternative fuel derived from the conversion of vegetable oils or animal fats and a simple alcohol such as methanol and ethanol. It is an alkyl ester of fatty acid made from renewable edible and non-edible biological resources. Biodiesel fuel is a proven alternative to petro- based diesel because it reduces lifecycle greenhouse emissions.
Biodiesel was produced by the trans-esterification of castor oil using mixtures of methanol and ethanol in molar percentages and potassium hydroxide (KOH) as catalyst. The optimum reaction conditions were 65^{0}C, 1.5w/w% KOH and 120 mins with a maximum yield of 89% biodiesel at 95% methanol. The spectrum displayed by the biodiesel using Shimadzu Fourier Transform Infra-Red Spectrometer – 8400S conformed to the ASTM standard. The biodiesel was blended with petro-diesel to produce B5 – B20 biofuels. The fuel properties: specific gravity at 15^{0}C, kinematic viscosity at 40^{0}C, flash points and gross calorific values were within the ASTM D 6751 standard. This study showed that ethanol/methanol blend can be successfully used to produce castor oil biodiesel and since ethanol is obtainable from biological sources, the esterification process becomes sustainable than making use of only methanol.
Key words: *Castor oil, Meth-ethanolysis, Biodiesel blends, Petro-diesel, Sustainability.*

1.0 INTRODUCTION

The growing concern related to the depletion of natural fossil fuel reserves caused by extensive usage necessitates the search for renewable energy. The depletion of the ozone layer and the consequent global warming heighten the importance of discovering and developing alternative energy and fuel sources. Currently, approximately 80% of the energy consumed worldwide is from fossil sources and 58% of that energy is used for transportation (Escobar et al., 2009). The most highly used sources of energy throughout the world are crude oil and coals, which are also used to produce various petroleum products. The projected increase of petroleum demand in 2025 is 40% (Holloway and Johnson, 2007). Furthermore, the energy used by the transportation industry in Europe increased by 22% from 1990 to 2000 (Karagiannidis et al., 2008). This level of energy use requires extensive extraction that in order to cope with future demands, suitable alternatives to fossil fuels in the form of biofuels are being investigated by researchers around the globe.

Castor oil (*Ricinus communis*) is a colourless or pale yellowish oil extracted from the seeds of the castor oil plant, it is cultivated around the world because of the commercial importance of its oil which is used in the manufacture of a number of industrial chemicals like

surfactants, greases and lubricants, specialty soaps, surface coatings, cosmetics and personal care products, pharmaceuticals, etc. India is the world's largest producer and exporter of castor oil (Hemant et al., 2011). It is currently cultivated on about 700,000 hectares mostly in Gujarat and Andhra Pradesh under rain fed conditions. The Indian variety of castor seed has an oil content of 42% and 48%. The residual oil cake, which contains about 5.5 % Nitrogen, 1.8-1.9 % Phosphorus and 1.1% Potassium, is used as organic manure. Castor grows well under hot and humid tropical conditions and has a growing period of 4 to 5 months. The average yield of seed and oil is 1250 kg/hectare and 550 lit/hectare respectively. The yield in terms of oil varies from 350-650 kg of oil per hectare when no maintenance is applied to the crop *i.e.* fertilizers etc. The comparative advantage of Castor is that its growing period is much shorter than that of Jatropha and being an annual crop it gives the farmers the ability to rotate or shift away easily depending on market conditions. However, among vegetable oils, castor oil is distinguished by its high content (over 85%) of ricinoleic acid (Hemant, et al., 2011).

Biodiesel production from castor oil has been reported in the literature (Aldo and Abraham, 2013; Berman et al., 2011; Oladimeji and Oyekunle, 2015). The trans-esterification of castor oil by Oladimeji and Oyekunle (2015) produced a maximum yield of 87.1% at 100% methanol.

Castor oil biodiesel has lower cost when compared to biodiesel obtained from other vegetable oils due to its solubility in alcohol such that the trans-esterification easily occurs at ambient temperature (Ramezani et al., 2010)

The petro-diesel fuel is a complex mixture with carbon atoms ranging between 12 and 18, whereas vegetable oil is a mixture of organic compounds ranging from simple straight chain compounds to complex structures of proteins and fat soluble vitamins which are commonly referred to as triglycerides (Barnwal and Sharma, 2005; Srivastava and Prasad, 2000). Vegetable oils are usually triglycerides, generally with a number of branched chains of different lengths and different degrees of saturation. Vegetable oils have about 10% lower heating value than petro-diesel due to the oxygen present in their molecules. The viscosity of vegetable oil, due to its large molecular mass and chemical structure, is several times higher than that of petro-diesel. While the cloud point and pour point are higher, the cetane number is comparable to that of petro- diesel (Barnwal and Sharma, 2005; Srivastava and Prasad, 2000). Any inefficient mixing of fuel with air contributes to incomplete combustion, therefore the high flash point and lower volatility characteristics of petro-diesel result in increased carbon deposit formation, injector choking, lubricating oil dilution and degradation. With vegetable oil as fuel, short term engine performance results are comparable to those with petro-diesel, but long term results with vegetable

oil or blends with petro-diesel lead to severe engine deposits, piston ring sticking and injector coking and thickening of the lube oil. High viscosity, low volatility and a tendency to polymerize within the cylinder are at the root of many problems associated with direct use of vegetable oils as fuel (Barnwal and Sharma, 2005; Peterson, 1986). Vegetable oils need to be modified to bring their combustion related properties closer to those of petro-diesel; the fuel modification is mainly achieved by reducing the viscosity and increasing the cetane number, cold flow property and oxidation stability. Considerable efforts have been made to develop vegetable oil derivatives that approximate the properties and performance of the hydrocarbon fuels (Demirbas, 2000; Ma and Hanna, 1999; Aldo and Abraham, 2013). The most widely used method is trans-esterification.

Trans-esterification is a chemical reaction between fat or oil (triglyceride) and alcohol in the present of a catalyst to form fatty acid alkyl esters (biodiesel) and glycerol. According to Dossin et al. (2006), the three main reaction stages in trans-esterification of triglyceride with methanol can be represented by equations 1 – 3,

$$T + CH_3OH \Leftrightarrow D + MeOl \quad (1)$$

$$D + CH_3OH \Leftrightarrow M + MeOl \quad (2)$$

$$M + CH_3OH \Leftrightarrow G + MeOl \quad (3)$$

In these reactions, triglyceride (T), diglyceride (D) and monoglyceride (M) react with methanol (CH_3OH) to form D, and glycerol (G) respectively along with methyl oleate (MeOl) or longer chain methyl ester depending on the glyceride chain length.

The overall reaction can be written as (Eqn. 4):

Triglyceride + 3Alcohol ⟶ *Glycerol + Ester*

$$T + 3CH_3OH \Leftrightarrow G + MeOl \quad (4)$$

The reaction is reversible and therefore excess alcohol is used to shift the equilibrium to the right. The alcohols that can be used in the trans-esterification process are methanol, ethanol, propanol and butanol. Methanol is the most frequently used alcohol. Methanol gives higher biodiesel yield than ethanol, this is because methanol is simpler in terms of chemical structure than ethanol, and thus the rate of trans-esterification is higher in methanol than ethanol. Also, the based catalyzed formation of ethyl ester is difficult compared to the formation of methyl esters. In the case of methanolysis, the products formed can easily be separated into upper methyl ester and lower glycerol but in ethanolysis separation is very difficult (Canakci and Gerpen, 2003).

2.0 EXPERIMENTAL SECTION

2.1 Reagents

- Methanol (Analytical grade –BDH, England)
- Isopropyl alcohol (Analytical grade –BDH, England)

- Ethanol (Analytical grade –BDH, England)
- Potassium hydroxide (Analytical grade-Loba Chemie, India)
- Crude castor oil (Holy Land Limited, Lagos)
- Petro-diesel (Total Filling Station, Lagos)

2.2 Equipment

- Cannon-Feske viscometer
- Glass reactor (500ml)
- Separating funnels
- Water bath
- Electronic digital weighing scale
- Pensky-Martens flash point tester
- Shimadzu Fourier Transform Infrared Spectrometer – 8400S

2.3 Determination of Optimum Catalyst Concentration for Trans-esterification Process.

- 1g of KOH was dissolved in 1litre of distilled water
- 1ml of oil was dissolved in 10ml of pure isopropyl alcohol and 2 drops of phenolphthalein solution was added.
- By using graduated syringe, KOH solution was gradually added to the oil-phenolphthalein solution until it turned and stayed pink for 15sec.
- The titre value of the KOH solution required was 6.0ml
- The optimum catalyst required was 1.53% of the mass of the crude castor oil.

2.4 Biodiesel Production

Biodiesel samples were produced by trans-esterification reaction making use of methanol/ethanol alcohol blends.

2.4.1 Methanolysis

- 2.6g of KOH was added to 69.96g of methanol in a 500ml beaker and the reaction was effected by stirring at room temperature. The product methanolate (CH_3OK) was formed and used as catalyst for the esterification reaction.
- 170g of castor oil was heated to 100^oC to remove its moisture content. The dehydrated castor oil was cooled to 60^oC and poured into a 500ml glass reactor placed inside the water bath.
- Prepared CH_3OK was then poured into dehydrated castor oil inside the water bath and the reaction was effected at 500rpm and 60^oC for 100minutes.

2.4.2 Preparation of Alcohol Blends

- A batch of 2.6g KOH was added to each batch of methanol/ethanol mixture in a 500ml reactor at 95%, 90% and 80% methanol using 12:1(alcohol/oil ratio). Each reaction was carried with vigorous stirring at room

temperature and the product formed is called potassium meth-ethoxide.

- The above procedure was repeated, but for only 95% methanol at 6:1, 8:1, 10:1, 13:1 and 14:1(methanol/oil ratio).

2.4.3 Meth-ethanolysis

- 170g of castor oil was heated to 100^{o}C to remove its moisture content. The dehydrated castor oil was cooled to 50^{o}C and poured into 500ml reactor placed inside the water bath.
- Each Prepared potassium meth-ethoxide at various alcohol/oil and methanol/ethanol ratio was now poured into each batch of dehydrated castor oil in the reactor and the reaction was carried out at 500rpm and 50^{o}C for 45mins. 60mins., 100mins., 120mins. and 135mins. This procedure was repeated at 55^{o}C and 60^{o}C.

2.4.4 Products Separation

- The mixture of the products of each run was now poured into a separating funnel and left for 24hours to settle.
- Glycerine and other by-products settled at the bottom of the separating funnel while impure biodiesel was at the top.
- The separating funnel tap was gently opened to discard the bottom products and impure biodiesel was now collected in a 500ml beaker.

2.4.5 Washing and Drying of Biodiesel

- Water was heated to 50^{O}C was poured into each run of impure biodiesel in 1:1(w/w) in a separating funnel and shaken together for 7 minutes.
- The mixture was left to settle for 40 minutes; the upper layer contained mainly the biodiesel while the lower layer was water solution containing traces of other products.
- The separating funnel tap was now gently opened to discard the water solution.
- The washing process was repeated for each run thrice and by the last washing the water had become very clear meaning that traces of other products have been completely removed remaining only pure biodiesel.
- The drying was done by heating the biodiesel to 100^{O}C to remove its moisture content.

2.5 Preparation of Biodiesel – Petrodiesel Blends

- B5, B10, B15, B20 were prepared by homogeneous mixing of 5ml, 10ml, 15ml, and 20ml of biodiesel with the corresponding volumes of petro-diesel.
- All the blends were prepared at room temperature.

2.6 Properties of biodiesel and the blends

2.6.1 Specific Gravity

The specific gravity of each sample was determined at 15^0Cby making use of 25ml density bottle. Each sample and the water were cooled to 15^OC using salted ice block.

2.6.2 Gross Calorific Value

The calorific value was determined using the formula:

$$Q_V = 12400 - 2100d^2$$

$$where \;\; d = specificgravity \;\; at \;\; 15^0 C$$

2.6.3 Kinematic Viscosity

This was determined at 40^{o}C using Cannon-Feske viscometer at atmospheric pressure. The kinematic viscosity constant was determined using the kinematic viscosity of water which is 1mm^2/s. Two arms out of three arms of the viscometer were filled with the sample at 40 ^{o}C. The sample temperature was maintained constant by placing the viscometer inside the water bath set at 40^{o}C during the experiment. The sample was now allowed to move up to the lower mark of the third arm. The time it took the sample to move from the lower mark to the upper mark of the third arm was taken. The kinematic viscosity was calculated using the formula:

$$k_V = Cxt$$

$$where \; k_V = kinematic \;\; viscosity \;\; at \;\; 40^0 C$$

$$C = kinematic \;\; constant$$

$$t = time \; taken \; by \; sample \; to \; move \; from \; lower \; to \; upper \; mark \; of \; the \; third \; arm \; in \; secs.$$

2.6.4 Flash Point

The flash point of the sample was determined using Pensky-Martens flash point tester. The sample was poured into the tester cup and covered. Thermometer was inserted into the tester to read the temperature. The sample was now heated and stirred with in-built heater and stirrer. A lighted flame was placed at the opening through which the vapor from the sample was ignited. The temperature at which the flame released was ignited was the flash point. (5)

2.6.5 Infra Red Spectroscopy

The infra red spectroscopy of the sample was carried out using Shimadzu Fourier Transform Infrared Spectrometer – 8400S. The infra red radiation was passed through the biodiesel sample. The sample absorbed some of the radiation while some passed through the sample (transmitted). The resulting spectrum represented the molecular absorption and transmission, creating a molecular finger print of the sample.

3.0 RESULTS AND DISCUSSION

3.1 Characterization of Crude Castor Oil and Petro- Diesel

The crude castor oil and petro- diesel used were characterized as shown in Table 3.1. The viscosity, specific gravity and flash point of crude castor oil were extremely high compared to petro-diesel. Consequently, transesterification of crude castor oil was carried out to reduce these properties. The petro-diesel properties were within ASTM standard (Kywe and Oo, 2009).

Table 1: Properties of Castor oil, Biodiesel and Petro-Diesel.

Samples	Flash Point (^{0}C)	Gross Calorific Value (cal/g)	Specific Gravity at 15^{0}C	Kinematic Viscosity at 40^{0}C (mm^2/s)
ASTM Standard for biodiesel -B100 (ASTM D6751)	100-170	≥10170	0.86-0.900	1.9-6.0
ASTM Standard for petro-diesel (ASTM D975)	60-80	≥10600	0.82-0.845	1.3-4.1
Crude Castor Oil	190	10482	0.956	923
Petro- Diesel	60	10869	0.854	2.01

3.2. Effect of Methanol-Ethanol Ratio

Figure.1 shows the effect of methanol- ethanol ratio at 12:1 alcohol/oil ratio, 60^{O}C reaction temperature, 100mins.and 500rpm. 100% methanol gave the highest yield (86.9%) followed by 95%methanol (84.5%). As the percentage of methanol decreased the yield decreased. From 80% methanol to 100% ethanol there was no product separation. This was due to the fact that the chemical structure of methanol was simpler than that of ethanol thus separation was easy when methanol was used but difficult when ethanol was employed and eventually leading to no separation of reaction products (Canakci and Gerpen, 2003).

3.3 Effect of Temperature and Reaction Time

Subsequent reactions were carried out at 95% methanol blend at 50^{0}C, 55^{0}C, 60^{0}C and 45mins, 100mins, 120min, 135mins as shown in Figure.2. The biodiesel yield increased with temperature with an optimal yield obtained at 120min at different temperatures. The optimal yields were 80.1 % (50^{0}C), 84.3% (55^{0}C), and 89% (60^{0}C) respectively.

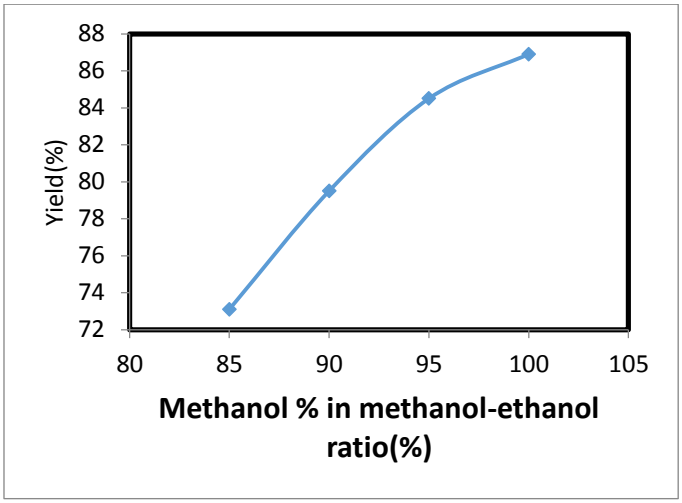

Figure 1: The Effect of Methanol – Ethanol Ratio (%) on the yield at 60^{0}C, 500rpm, 12:1 alcohol/oil, 1.53 % w/w (KOH) and 100mins.

Production of biodiesel was found to be favourable at temperatures below the alcohol boiling point but with increase in time, the reverse reaction occurred leading to decrease in biodiesel yield (Pramanik, 2003; Huaping et al., 2006).

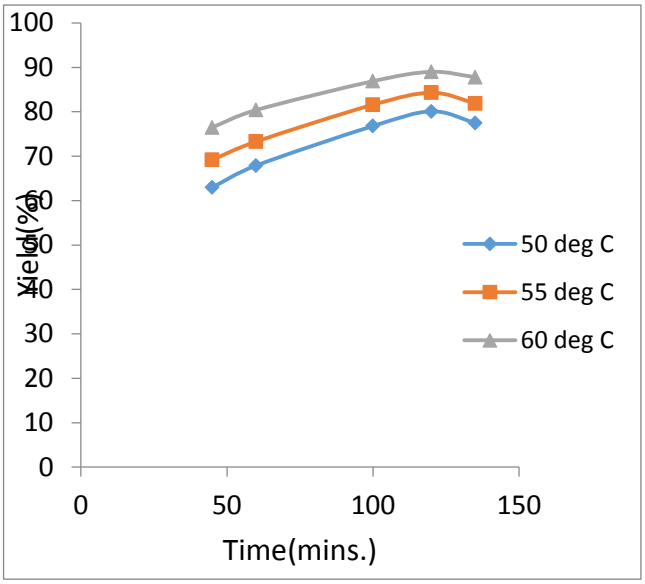

Figure 2: Effect of time on biodiesel yield at different temperatures, 500rpm, 12:1 Alcohol-Oil , 1.53 % w /w(KOH).

3.4 Effect of Alcohol – Oil Ratio

In order to shift the reaction forward excess alcohol was used ranging from 6:1(alcohol-oil ratio) to 14:1 as can be seen in Figure 3. The yield increased with increasing alcohol-oil ratio up to 13:1 when it remained constant. This correlates to the fact that optimal alcohol to oil ratio can be different based on the nature and quality of the vegetable oil used. It was reported that a maximum of 92% conversion was achieved using 10:1 methanol to oil ratio for biodiesel preparation from Karanja oil (Karmee et al., 2005).

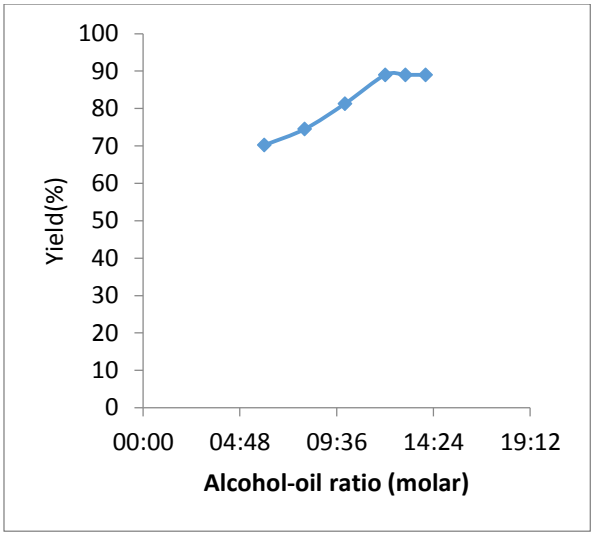

Figure 3. The Effect of Alcohol-Oil ratio on the Yield at 60^0C, 500rpm, and 120 mins and 1.53 %w/w (KOH).

3.5 Characterization of Castor Oil Biodiesel

Samples from all experimental runs were characterized to establish the kinematic viscosity, specific gravity, flash point and gross calorific value of the biodiesel produced. Table 2 showed the characteristic properties of the biodiesel samples obtained at optimum reaction conditions: 60^OC, 1.53%w/w (KOH), 500rpm, 12:1 Alcohol/Oil. These values were in conformity with the ASTM standards.

Table 2: Biodiesel yields at 60^{O}C, 1.53%w/w (KOH), 500rpm, 12:1 Alcohol/Oil.

Reaction time (min.)	Biodiesel yield (%)	Biodiesel properties			
		Kinematic viscosity at 40^{0}C (mm^{2}/s)	Specific gravity at 15^{0}C	Flash point (^{0}C)	Gross calorific value (cal/g)
45	76.5	5.89	0.891	138	10733
60	80.4	5.76	0.890	133	10735
100	86.9	5.98	0.891	135	10733
120	89.0	5.01	0.889	132	10740
135	87.8	4.99	0.888	130	10742

3.6 Blending of Biodiesel with Petro-Diesel

American Standard for Testing and Materials (ASTM) allows the blending of biodiesel with petro-diesel between B5 to B20. Samples of biodiesel obtained at the optimal conditions (89% yield, viscosity = 5.01 mm^{2}/s, specific gravity = 0.889, flash point =132^{0}C and gross calorific value = 10740.3 cal/g were subsequently blended with petro- diesel to produce B5 – B20. The properties of these B5 – B20 samples were plotted in Figure 4. The kinematic viscosity, specific gravity and flash point increased while gross calorific value decreased from B0 to B20.

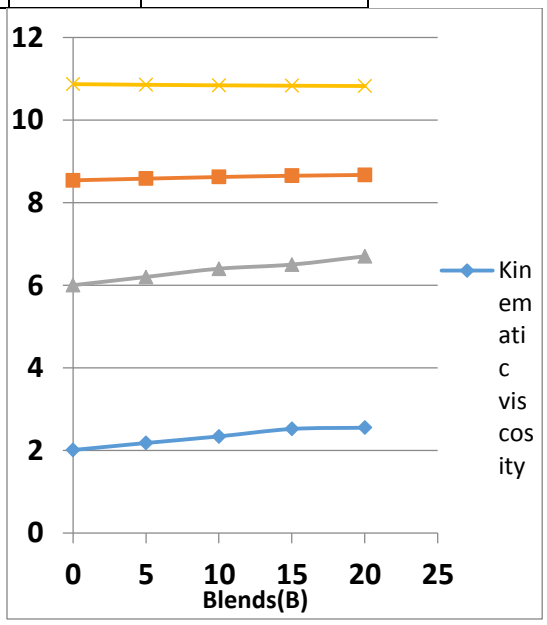

Figure 4: Kinematic viscosity, Specific gravity, Flash Point and Gross Calorific value of Petro-Diesel (B0) and the Blends.

3.7 Infra Red Spectroscopy

The infra red spectroscopy of each of the castor oil and biodiesel was obtained using Shimadzu Infra Red Spectrometer 8400S. The obtained spectrum as shown in Figures 5 and 6 with the biodiesel spectra conforming to ASTM standard.

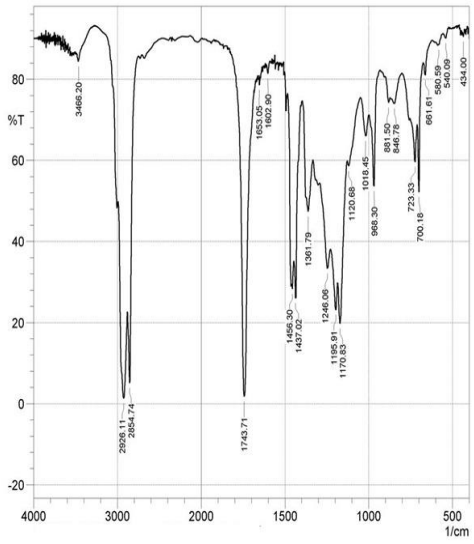

Figure 5 : Infra Red Spectroscopy of Castor Oil Biodiesel

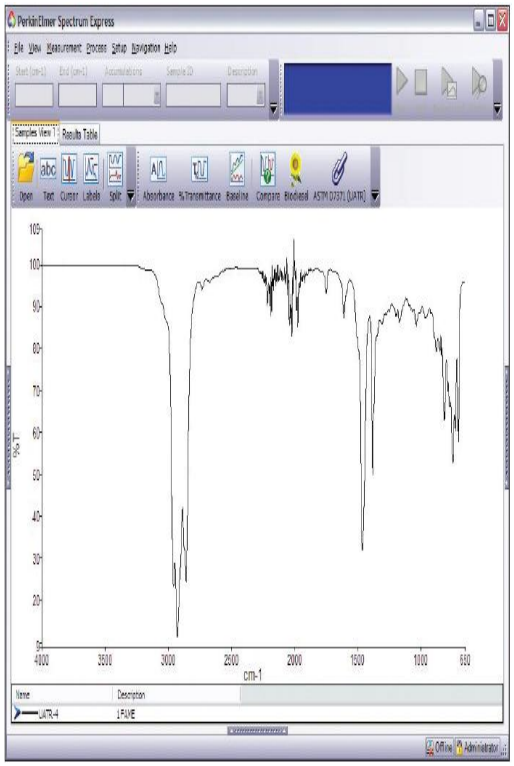

Figure 6: ASTM Standard Infra Red Spectroscopy of Biodiesel

4.0 CONCLUSION

A highly viscous castor oil was transesterified to lower viscous biodiesel using a blend of methanol and ethanol. Biodiesel samples formed by only methanolysis were easily separated from other by-products. Increase in concentration of ethanol in the binary blend reduced the biodiesel yield and at 20% ethanol blend, product separation was not physically possible. The yield increased with increase in the alcohol/oil ratio to an optimum of 12:1 at 60^0C and 120 minutes reaction time. The infra red spectroscopy of different biodiesel samples conformed to the ASTM standards. Also, the properties of the biodiesel, petro-diesel and their blends were within the ASTM standards

showing the acceptable quality of the products obtained.

The work majored on meth-ethanolysis and that application of the blends of methanol and ethanol makes the transesterification process more sustainable since ethanol production is renewable.

REFERENCES

Aldo, O.A. and Abraham, K.T. (2013), 'Investigation of the parameters affecting castor oil transesterification reaction kinetics for biodiesel production' *International Journal of Scientific and Engineering Research*, Vol. 4, pp.1-5.

ASTM (2008), Standard specification for biodiesel fuel (B100) blend stock for distillate fuels (ASTM D6751-08).

Barnwal, B.K. and Sharma, M.P. (2005), 'Prospects of biodiesel production from vegetable oils in India: Review, *Renewable and Sustainable Energy*, vol.9, pp. 363-378.

Berman, P., Nizri, S. and Wiesman, Z. (2011), 'Castor oil biodiesel and its blends as alternative fuel', *Biomass and Bioenergy*, vol. 35, pp. 2861- 2866.

Canakci, M. and Gerpen, J. (2003), A pilot to produce biodiesel from high free fatty acid feedstocks, *American Society of Agricultural Engineer*, vol. 46, pp. 945-955.

Dossin, T. F., Reyniers, M. F., Berger, R. J., and Marin, G. B.(2006). Simulation of heterogeneously MgO-catalyzed transesterification for fine-chemical and biodiesel industrial production. *Appl. Catal. B, Environ.* 67:136–148.

Escobar, J.C., Lora, E.S., Venturini, O.J., Tanez, E.E., Castillo, F.E. and Lamaze, O. (2009), Biofuel: Environment, technology and food security: Review, *Renewable and sustainable Energy*, vol.13, pp.1275-1297.

Hemant, Y.S., Panwar, N.L., Bamniya, B.R. (2011), Biodiesel from castor oil – a green energy option, *Journal of Low Carbon Economy*, vol.2, pp. 1-6.

Holloway, T. and Johnson, M. (2007), 'A global comparison of national biodiesel production potentials', *Environmental Science and Technology*, vol.41, No.23, pp.7967-7973.

Huaping, Z., Zongbin, W., Yuanxiong C., Ping, Z., Shijie,D., Xiaohua, L., Zongqiang, M., (2006), 'Preparation of biodiesel catalysed by solid super base of calcium oxide and its refining process', *China Journal of Catalyst*, vol. 27, pp. 391-396.

Karagiannnidis, A., Papadopoulos, A. and Cebrat, G. (2008), 'Proposing intelligent alternative propulsion concepts contributing higher CO_2, savings with first generation biofuels', *Management of* Environmental *Quality*: *An International Journal*, vol.19, No.6, pp.740-749.

Karmee, S.K. and Chadha, A. (2005). 'Preparation of biodiesel from crude oil of *Pongamia pinnata', Bioresource Technology* vol. 96, pp.1425-1429.

Kywe, T.T. and Oo, M.M. (2009), 'Production of biodiesel from Jatropha oil (Jatropha curcas) in pilot

plant', *Proceeding of World Academy of Science Engineering and Technology*, vol.38, pp: 2070-3740.

Ma, F. and Hanna, M. A. (1999), 'Biodiesel Production: A review', *Bioresources Technology*, vol. 70, pp. 1-15.

Oladimeji Ayodeji and Oyekunle, L.O. (2015) "Characterization of Biodiesel Produced by Meth-butanolysis of Castor Oil" *International Journal of Research in Engineering and Technology (IJRET)*, vol. 4, issue 9, pp. 29 - 33.

Peterson, C.L. (1986), 'Vegetable oil as a diesel fuel: Status and research priorities', *America Society of Agricultural Engineer*, vol.29, pp. 1413-1422.

Pramanik, K. (2003), 'Properties and use of *Jatropha curca* oil and diesel fuel blends in compression ignition engine,' *International Journal of Renewable Energy*, vol. 28, pp. 239 -248.

Ramezani, K., Rowshanzamin, S. and Epicene M.H., (2010), 'Castor oil transesterification reaction: A kinetics study and optimization of parameters', *Energy*, vol. 35, pp.4142-4148.

Srivastava, A. and Prasad, R. (2000), 'Triglycerides-based diesel fuels', *Renewable Energy Review*, vol.4, pp.111-133.

THE USE OF I_{MN} APPROXIMANTS TO ACCURATELY SOLVE STIFF DIFFERENTIAL EQUATIONS AND SYSTEMS POSSESSING STEEP AND OSCILLATORY RESPONSES

Femi Taiwo
Department of Chemical Engineering, Obafemi Awolowo University, Ile-Ife, Nigeria.
Email: femtaiwo@yahoo.com, ftaiwo@oauife.edu.ng

ABSTRACT

I_{MN} approximants are a fast and convenient method of solving initial value problems in linear stiff differential algebraic equations as well as obtaining the numerical inversion of Laplace transforms. In the past it was impossible to use them to obtain sufficiently accurate inversions of certain steep and highly oscillatory responses as use-able values of N had to be relatively small not only to ensure reliable evaluation of I_{MN} constants but also in order to avoid undue rounding errors in the computed results. However, the development of computer algebra systems such as Mathematica which permit infinite precision computation has provided greater latitude for the application of the method. This work is an exposition of the potency of I_{MN} approximants in accurately and cheaply inverting functions in the Laplace domain whose time functions are steep, oscillatory or stiff. We show how to obtain very accurate results in these circumstances using both the global and step by step methods. The results of using I_{MN} step-by-step technique to rapidly solve the stiff differential equations of a large staged process are also presented. Since the computation time is larger when a computer working precision is set higher than the default, it is expedient to use the minimum working precision (higher than default) guaranteing computed results of desired precision. A novel algorithm has been devised by Taiwo et al (2006) to ensure this. As Matlab gives inaccurate results, Mathematica has been used to compute both the transfer function and the analytical expression for the time response of the plant. This work is dedicated to Prof Vladimir Zakian, as indicated at the end of this paper.

1.0 INTRODUCTION

I_{MN} approximants have wide applicability in tackling practical problems in engineering and science. Their applications range from repeated computation of closed-loop responses when designing control systems using the method of inequalities (Zakian, 1979; Taiwo, 1980; Zakian, 1996; Whidborne and Liu, 1993), the identification of kinetic parameters in adsorption (Taiwo and King 2003), the analysis of boundary conditions in both filled and empty tubes (Taiwo et al., 1995) and the design of robust centralized multivariable controllers (Taiwo et al., 2014a, b).

The I_{MN} approximant numerically inverts the Laplace transform of the function describing a phenomenon, either recursively or in a global manner rapidly yielding sufficiently accurate results in typical applications.

The present work is to further explore the untapped potentials of the technique for solving process systems engineering problems. The first problem solved here is a large scale staged tri-diagonal process with stiff differential equations. Such plants are common place in the chemical plant. The particular example solved here is a bench mark and has been identified by Kim and Friedly (1974) as an optimally designed staged system. I_{MN} step-by-step technique which is known to be immune to stiffness has been used to solve the resulting differential equations, while Mathematica has been used to compute both the transfer function and the analytical expression for the time response as Matlab gives inaccurate results. It has been decided to include the numerical inversion of the sine wave as an example since this is a common test signal in practical work. Moreover, it serves to highlight the way to obtain accurate results for open or closed loop systems possessing oscillatory responses. Both the step-by-step technique and higher I_{MN} approximants, applied in the global form, can solve this problem. The last example is characterized by very steep responses and involves concentration profiles in an empty tube at high Peclet Numbers. The recommended procedure for solving this problem is the use of higher I_{MN} global method, as the mathematical basis for the extension of the step-by-step technique to partial differential equations is still being developed.

Using the notions of acuity and equivalent-width, as well as the derivation of the I_{MN} formula in the Appendix, it becomes clear why higher N for the global method or small step h for the step by step technique, is needed to obtain I_{MN} results of sufficient accuracy for functions which vary rapidly at large t.

By using higher I_{MN} approximants of full grade, it is not only possible to accurately invert functions for which it had earlier been erroneously concluded that the I_{MN} approximant did not produce accurate results but also to check the accuracy of the computed results for cases where no analytical solution exists. In view of the large values of the I_{MN} constants involved for some of the examples solved here and in order to minimize rounding errors, infinite precision arithmetic available in Mathematica has been exploited in the computations involving the global method. Taiwo et al., (2006) have done work on determining the computer working precision in order to ensure computed results of desired precision. The important fact is to realise that computation time heavily depends on computer working precision. Hence one should utilize the minimum computer working precision guaranteeing desired precision in the computed results.

Where applicable, the I_{MN} results have been compared with those obtained using the method of Honig and Hirdes (1984), which is based on Fourier series expansion. Higher I_{MN} results have been used to accurately estimate the error in the results of both methods.

2.0 Zakian's (1975a,b) I_{MN} approximants

Let f(t) have a Laplace transform:

$$L(f,s) = F(s) = \int_0^\infty f(t)e^{-st}dt \quad (1)$$

where Re(s) > σ and f(t) is continuous for t ≥ 0 and of exponential order σ. The I_{MN} approximant of f(t) (see the Appendix for the derivation) is an expression of the form:

$$I_{MN}(f,t) = t^{-1}\sum_{i=1}^{N} K_i L(f, \frac{\alpha_i}{t}) \quad (2)$$

Many different sets K_i, α_i may be defined, but for the purpose of this work, they are assumed to satisfy the relation:

$$e^{-z}_{MN} = \sum_{i=1}^{N} \frac{K_i}{z+\alpha_i} \quad (3)$$

where e^{-z}_{MN} is the (M/N) Padé approximant of e^{-z}. Let $\hat{\alpha}_{MN} = \min_i\{\mathrm{Re}(\alpha_i)\}$. It is known that under certain conditions on f(t):

$$f(t) - I_{MN}(f,t) = 0(t^{M+N+1}),\ t \to 0^+ \quad (4)$$

whenever $\hat{\alpha}_{MN} > 0$. Numerical tests have been performed (Zakian, 1975a) to determine all (M,N) in 0≤M<N≤ 20 for which $\hat{\alpha}_{MN} > 0$. Taiwo et al. (1995) and Taiwo and King (2002) have carried out further tests and produced a table of all (M,N) in 21 ≤ N≤ 540 (M<N) for which $\hat{\alpha}_{MN} > 0$. Furthermore, if f(t) is of exponential order σ <0 as $t \to \infty$, then:

$$f(t) - I_{MN}(f,t) = 0(t^{M-N}),\ t \to \infty \quad (5)$$

Thus, I_{MN} approximant is capable of good approximation at both large and small t; for a fixed N, a trade-off between accuracy at large t and accuracy at small t is implemented by changing M. Equation (2) is useful in the numerical inversion of Laplace Transforms. Computationally, for N even, (2) may be reduced to an expression of the form:

$$I_{MN}(f,t) = 2\ t^{-1}\sum_{i=1}^{N/2} \mathrm{Re}\{K_i L(f, \frac{\alpha_i}{t})\} \quad (6)$$

since the constants K_i , α_i occur in complex conjugate pairs. The constants K_i , α_i are obtained by evaluating the residues and poles in the partial fraction expansion of e^{-z}_{MN} (see for example, Zakian and Edwards, 1978).

The inversion formulae give rise to a number of techniques for the solution of initial value problems of the form

$$\frac{dx}{dt} = Ax(t), \quad x(0) = x_0$$

(7)

where A is an n*n constant matrix, x(t) is an n-vector and x_0 is the given initial condition.

Firstly, the Laplace transform of the solution x(t) may be obtained explicitly from (7) and the inversion formula (2) applied in a global manner. Secondly, (7) may be Laplace transformed to give

(sI-A)L(x,s) = x(0)

(8)

where L(x,s) is the Laplace transform of the solution x(t). The vectors L(x, α_i/t) may be obtained by solution of the algebraic systems

$((\alpha_i/t)I-A)\ L(x, \alpha_i/t) = x(0),\ i = 1,2,\ldots,N$

(9)

for particular values of t, and thus the inversion formula (2) may then be applied, again in a global manner. When N is even, the formula (6) may be applied, whence only N/2 systems (9) need to be solved.

However, the accuracy of I_{MN} at small t may best be exploited in a step-by-step technique. Let t_r, r = 0,1,2,.. be points on the half-line $t \geq 0$ such that t_0 = 0, $t_{r+1} - t_r = h$ and h > 0, where h depends, in general, on r. Let x_r denote a numerical approximant to $x(t_r)$. Let $X_{tr}(s)$ denote the Laplace transform:

$$X_{tr}(s) = \int_0^\infty x(t_r + \lambda)e^{-s\lambda}d\lambda$$

(10)

Then replacing x(t) by $x(t_r+\lambda)$ in (7) and taking Laplace transforms we obtain

$(sI-A)\ X_{tr}(s) = x(t_r)$

(11)

Clearly, the inverse of $X_{tr}(s)$ evaluated at h is $x(t_{r+1})$. The I_{MN} approximant of $x(t_r+\lambda)$ evaluated at h is

$$h^{-1}\sum_{i=1}^{N} K_i X_{t_r}(\frac{\alpha_i}{h})$$

(12)

On combining (9) and (10), the following recursion formula is obtained:

$((\alpha_i/t)I-A)\ X_{i,r} = x_r,\ i = 1,2,\ldots,N$

(13a)

$$x_{r+1} = h^{-1}\sum_{i=1}^{N} K_i X_{i,r} \qquad r = 0,1,2,\ldots$$

(13b)

The main work at each recursion lies in the solution of N uncoupled n*n algebraic systems (13a). In fact, if N is even, the vectors $K_iX_{i,r}$ occur in complex conjugate pairs and (13b) reduces to an expression of the form

$$x_{r+1} = 2h^{-1}\sum_{i=1}^{N/2} \mathrm{Re}(K_i X_{i,r}) \qquad r = 0,1,2,\ldots$$

(13c)

for which only N/2 systems (13a) need to be solved. In practice, considerable economy is achieved by keeping the step length constant and calculating, once for all, upper and lower triangular factors of the matrix $((\alpha_i/t)I-A)$ for each i. Moreover, any special structure of the A matrix, such as sparseness, is preserved in the matrices $((\alpha_i/t)I-A)$ and can therefore be exploited. Further economy can be achieved by the use of small N, while accuracy is controlled by the step length.

Additionally, the use of small N reduces round-off error for software possessing only finite precision arithmetic.

It has been shown (Zakian 1975a, Zakian and Edwards 1978) that for I_{MN} approximants of full grade, the recursion (13) has the useful property of A stability, i.e. when applied to the scalar problem

$$\frac{dx}{dt} = zx(t) \quad x(0) = x_0 \tag{14}$$

for any Re(z) < 0 and using a constant step length of any size, the recursion yields a sequence $\{x_r\}$ which tends to zero as $r \rightarrow \infty$, thus preserving the stability of (14). Moreover, it is known (Zakian 1975a) that for any matrix A, all whose eigenvalues have negative real part, the recursion yields a similarly converging sequence when applied with constant step length of any size to the problem (7). This property is known as Σ stability. It will be readily appreciated that a Σ stable recursion has considerable advantages over other methods, particularly when the system (7) is stiff.

From the foregoing, the difference between the global and step-by-step methods is that while for the global method the origin is fixed and the I_{MN} approximant is calculated at a number of values of t whereby the distance from the origin at which the approximant is calculated increases with t, for the step-by-step method, the origin is effectively shifted at the (r+1)th step to the point t_r, and the I_{MN} approximant is calculated at a distance h from the new origin so that the distance h from the new origin at which the approximant is calculated remains small.

It may be noted that both global and step-by-step techniques can be easily applied to equations of the form

$$\frac{dx}{dt} = Ax(t) + u(t), \quad x(0) = x_0 \tag{15}$$

where u(t) is Laplace transformable and represents the input to the system. This is dealt with in detail in Zakian (1975a).

As indicated in Taiwo et al. (1995) and Taiwo and King (2002), comparison of computed results with higher I_{MN} results facilitates an estimation of the error for both the step-by-step and global methods.

3.0 ILLUSTRATIVE EXAMPLES.

3.1 Example 1

A large number of separation equipment in the chemical plant are staged systems having linearized models with tri-diagonal A matrices. Such systems have been of interest to many investigators (Kim and Friedly,1 974; Georgakis and Stoever, 1982; Celebi and Chimowitz, 1985; Shimizu et al., 1985; Skogestad et al., 1988; Carmola and Chimowitz, 1990; Prabhu and Chidambaram, 1991). A number of such systems have characteristics which render them difficult to analyse and control. Such characteristics include their large scale, stiffness and ill-conditioning. Their large scale nature has prompted investigators (Kim and Friedly, 1974; Georgakis and Stoever, 1982; Celebi and Chimowitz, 1985; Carmola and Chimowitz, 1990) to devise methods for reducing their dimensionality while several robust control methods (Shimizu et al., 1985; Skogestad et al., 1988; Prabhu and Chidambaram, 1991) have been proposed to minimize the sensitivity caused by ill-conditioning. In this work, we propose the exploitation of I_{MN} step-by-step method for their rapid and accurate simulation. For our example we take the following model (Kim and Friedly, 1974; Carmola and Chimowitz, 1990):

$$\frac{dx}{dt} = Ax(t) + bu(t), \quad y(t) = cx(t), \quad x(0) = x_0 \tag{16}$$

where

$b = [1,0,0,\ldots. 0]^T$, $c = [0,0,0,\ldots 0 ,1]$.

$$A = \begin{bmatrix} -2 & 1 & 0 & \dots & 0 & 0 & 0 \\ 1 & -2 & 1 & \dots & 0 & 0 & 0 \\ 0 & 1 & -2 & \dots & 0 & 0 & 0 \\ \vdots & \vdots & \vdots & \ddots & \vdots & \vdots & \vdots \\ 0 & 0 & 0 & \dots & -2 & 1 & 0 \\ 0 & 0 & 0 & \dots & 1 & -2 & 1 \\ 0 & 0 & 0 & \dots & 0 & 1 & -2 \end{bmatrix}$$

u(t) is the plant input while y(t) is the output. This matrix was used by Evans et al. (1985) to test their eigenvalue algorithm, while Carmola and Chimowitz (1990) used it to test their model reduction technique. Kim and Friedly (1974) noted that this A matrix represents an optimally designed staged system.

We first consider the 50^{th} order model. It was impossible to compute an accurate transfer function model of this plant using Matlab, hence Mathematica can be used to directly determine the transfer function from $c(sI-A)^{-1}b$. However, as the A matrix is tri-diagonal, the transfer function can also be accurately and more rapidly computed using Mathematica by separately determining the characteristic polynomial and the numerator polynomial of the model. The numerator polynomial is determined from first principles and formulae for these are available (Carmola and Chimowitz, 1990). The analytical expression for the step response of the plant can be accurately determined using Mathematica by decomposing the product of the transfer function and the step input into partial fractions and Laplace inverting, since direct use of the Inverse Laplace Transform function available in Mathematica did not produce a result because the personal computer ran out of memory. For the determination of this analytical expression, 40 digits of precision are needed in the computation in order to obtain accurate results. From the analytical time response expression, it is noted that the fractional response of the plant at t = 100 is 0.00893, signifying that the plant exhibits a time delay of almost 100. Furthermore, the response of the system is 99.99% complete at t = 2600. This is a stiff system with stiffness ratio $1.0535*10^{3}$.

We now investigate the results of numerically computing the step response of this plant using $I_{3,4}$ and $I_{5,6}$ step by step approximants. Since the response of the plant is practically zero for t < 100, we shall first investigate the performance of these approximants for t = 50(50)2600 and consider other step lengths later. Although we know that the response at t = 50 is virtually zero, we include this point in the experiment in order to test the goodness of the approximant for computing the response of high order systems, with large relative degree (and hence large delay), near the origin. It was found that with $I_{3,4}$ approximant, although the absolute error ($2.0265*10^{-7}$) at t = 50 is small, the percentage error is 43.42 because the analytical value of the response ($4.667*10^{-7}$) at this point is small. It was therefore decided to use the $I_{5,6}$ approximant to compute the single sample at t = 50 while the $I_{3,4}$ approximant was used to compute the other samples for this step length. The result of doing this is given in the second row of Table 1. The row $I_{3,4}$ (a) (Table 1) is the result obtained using $I_{3,4}$ approximant alone for t = 100(50)2600, since the response for t < 100 is virtually zero. The row $I_{3,4}$ (b) is the result obtained using $I_{3,4}$ approximant alone for the interval t = 100(100)2600 since $y(t<100) \approx 0$. It is seen that I_{MN} requires the smallest CPU time to do the computation. For this and other cases tabulated, the largest percentage error occurred during the first sample. This is because the actual value of the response is small for small times. It was discovered that the $I_{3,4}$ approximant gave sufficiently accurate results for

other step lengths, larger or smaller than 50. It is worth pointing out that in performing the LU factorization for this problem, the tri-diagonal structure of the matrix was exploited to reduce storage requirements and computing time (Cheney and Kincaid, 1999).

The other methods with which I_{MN} approximant has been compared are the various functions in Matlab specially written to handle stiff systems (these have names beginning with ode) and the classical fourth order Runge Kutta method (RK4TH). The Matlab functions automatically determine the desired (variable) step-length, although the user can observe the computed response at any desired value of time, so in uniformity with the first case above the computed results were observed at t = 50(50)2600. The best result from these functions was obtained using ode15s followed by ode23T, ode23TB and ode23s. It is noted that the performance of ode23s is much worse than those of the other three Matlab functions. On the other hand, ode15s is more than 1.5 times faster than the other two. RK4TH required the largest CPU time and the largest useable stable step-length is 0.685.

It was noted earlier that the I_{MN} method is immune to stiffness, hence one can use large step lengths in the computation. For t = 200(200)2600 and t = 300(300)2700, $I_{3,4}$ approximant gave respectively the following maximum percentage errors 1.064 and 0.416 with the corresponding CPU times of 0.11s and 0.055s. Still larger steps were used with accurate results in all situations. Where one is required to compute process responses for both short and long times for stable systems, it may be expedient to use varying steps, with shorter ones near the origin and longer ones at long times.

Table 1. Maximum percentage errors and CPU times for the 50th order model of Example 1.

Method	Maximum percentage Error	Average CPU Time(s)
$I_{3,4}$ and $I_{5,6}$	1.212	0.431
$I_{3,4}$ (a)	1.196	0.388
$I_{3,4}$ (b)	2.386	0.184
Ode15s	0.813	0.474
Ode23T	4.679	0.714
Ode23TB	3.723	0.830
Ode23s	5.218	7.052
RK4TH	0.927	33.372

Further computations were also done for the 100th order model of (16). The stiffness ratio in this case is $4.113*10^3$, the response being 99.4% complete for t = 6000, and the fractional response at t = 300 is 0.0014, signifying that the system effectively has a time delay of 300. Here, one needs 80 digits of computation in order to accurately determine the analytical expression for the time response. The computed results were compared with the analytical ones at t = 200(100)6000 and the relevant results given in Table 2. As with the foregoing example, the $I_{3,4}$ step by step approximant requires the minimum CPU time and the performance of Matlab functions follows the trends described earlier.

Table 2. Maximum percentage errors and CPU times for the 100th order model of Example 1.

Method	Maximum percentage Error	Average CPU Time(s)
$I_{3,4}$	1.398	1.45
Ode15s	0.944	1.48
Ode23T	4.723	2.15
Ode23TB	3.799	2.70
Ode23s	5.718	30.38
RK4TH	1.421	158.24

Further computations were carried out using the $I_{3,4}$ approximant with the following results. For t = 200(200)6000, although the error ($1.188*10^{-7}$) of the computed result at t = 200 is small, the percentage error (48.07) is large as the value of the response at this time ($2.471*10^{-7}$) is small. Hence it was decided to compute this one sample using the $I_{5,6}$ step by step approximant while the remaining samples were computed using the $I_{3,4}$ approximant with the maximum percentage error and CPU times given respectively as 1.439 and 0.74s. For t =

300(300)6000, 400(400)6000, 500(500)6000 and 600(600)6000, the respective CPU times are 0.50s, 0.39s, 0.33s and 0.27s with the corresponding maximum percentage errors of 3.572, 2.303, 0.021 and 1.038.

The following should be noted from the above results.

• Unless otherwise stated, the largest percentage error occurred at the first sample observed for all the methods. This is because the value of the response at this time is small.

• When one is required to compute process responses for both short and long times for smooth stable functions using I_{MN}, it may be expedient to use varying steps, with shorter ones near the origin and longer ones at long times.

• The more widely separated the points are where responses are desired, the greater the advantage of I_{MN} over other methods for solving initial value problems as it gives sufficiently accurate results for typical problems in chemical engineering even when large steps are used.

• The step by step method is ideal when one does not have facilities for infinite precision computation as low approximants give sufficiently accurate results by utilizing the accuracy of the I_{MN} at small t, through the appropriate control of h. Notice that one does not need an explicit expression for the transfer function in order to numerically invert the transform in this case.

• It is noted that one does not need any special procedure in order to obtain accurate results for this problem. This is because the response is smooth and monotonic so that the existence of a finite equivalent-width (27) (See Section 4 for the explanation of this term) at long times for the small N used does not lead to significant error as (23) gives sufficient accuracy in this case.

• The I_{MN} techniques are easily programmed and one does not require programming expertise to implement it in different software packages.

3.2 Example 2

$$F(s) = \frac{1}{s^2+1}$$

Which has the inverse f(t) = sint

This example has been included in order to properly address some issues in the literature concerning what had been perceived as the limitations of I_{MN} approximants. Additionally, it is felt that this function is readily encountered in analysis as a common test function and also simulates the

behaviour of a lightly damped open or closed-loop system.

In their very useful book (Rice and Do, 1995), three examples are given to illustrate numerical Laplace inversion using I_{MN} approximants. Although all the results can be improved, we deal only with the improvement of the results of their example 9.17 (Rice and Do, 1995, pp 386-387), since the results of their example 9.16 (Rice and Do, 1995) are sufficiently acceptable. The necessary procedure required to improve the results of their example 9.18 have been given elsewhere by Taiwo et al., (2002).

On employing the $I_{9,10}$ approximant, Rice and Do (1995) obtain a result that is more than 25% in error at t = 16.5. However, this result can be easily improved by using either, in a global fashion, higher approximants or I_{MN} step-by-step method. We have reworked the example for t = 0.5(1.0)20.5 and obtained the results given in Table 3 using I_{MN} global method, from where it is clear that the $I_{14,22}$ approximant gives a result accurate to five decimal places and therefore of sufficient accuracy for practical purposes.

If a more accurate result is desired, then the $I_{19,28}$ approximant could be used. The result in this case (with accuracy of 11 decimal places) is more accurate than that obtained using the method of Honig and Hirdes (1984). We have not bothered to manually set the free parameters for this latter method here as it is felt that this result is already sufficiently accurate for practical purposes. Notice that the time range used here is more than that in the original problem. Using the $I_{3,4}$ step-by-step method, the maximum error in the computed results is $1.1141*10^{-7}$ at t = 20.5 for a step h = 0.5s.

Table 3. Maximum errors in the computed results using the various approximants as well as the maximum errors when the method of Honig & Hirdes (1984) is used for example 2.

Method	Maximum Error, E_{max}	Location of E_{max}, x_{Emax}
$I_{14,22}$	$3.98*10^{-6}$	20.5
$I_{19,28}$	$7.58*10^{-13}$	20.5
Honig & Hirdes (1984) automatic setting of free parameters	$1.05*10^{-11}$	5.5

3.3 Example 3

This example concerns the dispersion model for an empty tube involving correct boundary conditions of Danckwert (1953). See also, Seidel-Morgenstern (1991), Taiwo et al., (1995) and Taiwo and King (2001). The differential equation model of this process is available in the above references and Seidel-Morgenstern (1991) and Taiwo and King (2001) did a study of the effect of the assumed boundary conditions on the computed exit response. In the present work we are interested in accurately determining the exit response when the correct boundary condition is used as well as providing novel results on required values of M and N in order to get accurate results for different Peclet Numbers when I_{MN} approximants are used for this problem. We employ only the global method here as the step-by-step technique has not been sufficiently developed for partial differential equations. The Laplace transform of the normalised concentration is given by

$$F(x,s) = \frac{\lambda_2 \exp(\lambda_1 x) - \lambda_1 \exp(\lambda_1 + \lambda_2 x - \lambda_2)}{s((1-\lambda_1/Pe)\lambda_2 \exp(\lambda_2) - (1-\lambda_2/Pe)\lambda_1 \exp(\lambda_1))} \quad (17)$$

Where

$$\lambda_1 = \frac{Pe}{2} - \sqrt{\frac{Pe^2}{4} + Pes} \quad ;$$

$$\lambda_2 = \frac{Pe}{2} + \sqrt{\frac{Pe^2}{4} + Pes} \quad (18)$$

Pe denotes the Peclet number for axial mass transport. This example is particularly instructive in demonstrating the need to use higher I_{MN} approximants as Pe (and correspondingly the steepness of the response) increases.

The smallest Peclet number considered here was 20 and the Laplace transform inversion was done at τ = 0.4(0.2)1.8, with τ being dimensionless time (Seidel-Morgenstern, 1991). From Table 4 we noted that the results of the $I_{9,16}$ approximant were accurate to 5 decimal places while those of the $I_{25,34}$ approximant were accurate to 12 decimal places. The results obtained using the method of Honig and Hirdes (1984) with automatic setting of free parameters were accurate to 11 decimal places. The next situation concerns Pe = 100 where the Laplace inversion was done at τ = 0.7(0.1)1.4. From Table 4, $I_{14,22}$ approximant gave results accurate to 4 decimal places while the $I_{30,40}$ approximant results were accurate to 11 decimal places and the results obtained using the method of Honig and Hirdes (1984) were accurate to 12 decimal places. For Pe = 500, Laplace inversion was done at τ = 0.9(0.02)1.08 with respective accuracies of 6 and 12 decimal places for $I_{35, 46}$ and $I_{58,70}$ approximants. 11 decimal places of accuracy was obtained using the method of Honig and Hirdes (1984). With Pe = 10000, the Laplace transform inversion was done at τ = 0.97(0.01)1.03 giving results that were accurate to 6 and 14 decimal places for $I_{145,160}$ and $I_{268,288}$ respectively. When using the method of Honig and Hirdes (1984), one has to manually set the free parameters in order to obtain results accurate to 12 decimal places. The difficulty encountered in this case was due to the steplike response (Fig. 1).

Table 4. Maximum errors in the computed results using the various approximants as well as the maximum errors when the method of Honig & Hirdes (1984) is used for the dispersion problem at various Peclet numbers for example 3.

Pe =20	Method	Maximum Error, E_{max}	Location of E_{max}, x_{Emax}
	$I_{4,10}$	$2.79*10^{-4}$	1.4
	$I_{9,16}$	$1.14*10^{-6}$	1.8
	$I_{14,22}$	$3.90*10^{-9}$	1.8
	$I_{25,34}$	$2.36*10^{-13}$	1.8
	Honig & Hirdes, automatic setting of free parameters	$1.90*10^{-12}$	1.8
Pe =100	Method	Maximum Error, E_{max}	Location of E_{max}, x_{Emax}
	$I_{4,10}$	$3.63*10^{-3}$	1.4
	$I_{9,16}$	$4.04*10^{-4}$	1.4
	$I_{14,22}$	$9.31*10^{-6}$	1.4
	$I_{30,40}$	$2.17*10^{-12}$	1.4
	Honig & Hirdes, automatic setting of free parameters	$1.02*10^{-13}$	1.3

Pe =500	Method	Maximum Error, E_{max}	Location of E_{max}, x_{Emax}
	$I_{14,22}$	$5.18*10^{-3}$	1.04
	$I_{19,28}$	$7.11*10^{-4}$	1.04
	$I_{25,34}$	$7.20*10^{-5}$	1.08
	$I_{30,40}$	$5.00*10^{-6}$	1.06
	$I_{35, 46}$	$2.52*10^{-7}$	1.08
	$I_{41,52}$	$9.47*10^{-9}$	1.06
	$I_{46,58}$	$4.36*10^{-10}$	1.08
	$I_{58,70}$	$1.25*10^{-13}$	1.06
	Honig & Hirdes, automatic setting of free parameters	$4.18*10^{-12}$	0.96
Pe=10000	Approximant	Maximum Error, E_{max}	Location of E_{max}, x_{Emax}
	$I_{46,58}$	$3.3374*10^{-2}$	0.99
	$I_{86,100}$	$1.3123*10^{-3}$	1.01
	$I_{121,136}$	$3.9699*10^{-5}$	1.03
	$I_{145,160}$	$2.9788*10^{-7}$	1.03
	$I_{223,238}$	$1.7307*10^{-11}$	1.03
	$I_{268,288}$	$1.2910*10^{-15}$	1.03
	Honig & Hirdes, automatic setting of free parameters	$2.82*10^{-2}$	1.01
	Honig & Hirdes, manual setting of free parameters	$1.4530*10^{-13}$	0.99
	Honig & Hirdes, previously computed best result. (Seidel-Morgenstern, 1991)	$1.1179*10^{-5}$	0.99

This was as expected, because for very high Pe, the flow through the tube was very close to ideal plug flow so that the exit composition response was virtually $1(\tau\text{-}1)$, which was a delayed step response stepping at $\tau = 1$.

This was another example with steep response. By varying Pe we have demonstrated that a steeper response demanded higher acuity (Zakian, 1969; Taiwo and King, 2002), which led to larger N, thus as N increased the sifting ability of the method was near perfect.

Taiwo et al., (2006) have done work on determining the computer working precision in order to ensure computed results of desired precision. The important fact is to realise that computation time heavily depends on computer working precision. Hence one should utilize the minimum computer working precision guaranteeing desired precision in the computed results. It is also worth noting that the response profile of the above process to 31 decimal places had been computed (Taiwo and King, 2002).

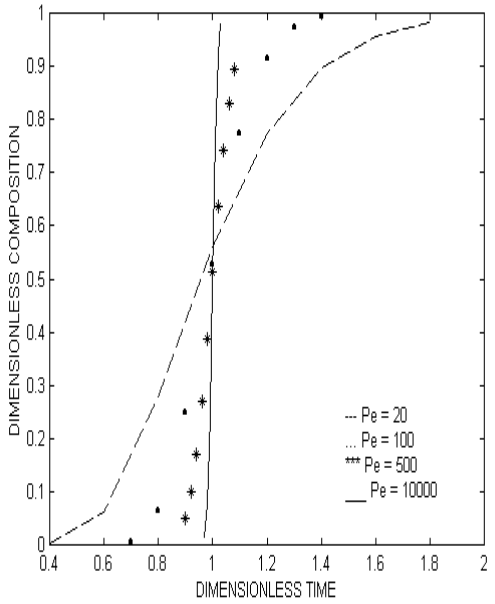

Figure 1: Graph of Composition against Time in an Empty Tube with Dispersion

5.0 DISCUSSION AND CONCLUSION

It has been shown in this work that I_{MN} techniques can be used to rapidly solve the differential equations of large scale systems which may be stiff as well as the solution of oscillatory and steep responses. For the solution of the large scale staged system, it has been found that the step-by-step technique is faster than currently available Matlab functions for solving such problems. Mathematica had to be used to compute the transfer function of the large scale system as Matlab gave inaccurate results. This former software was also adapted to get the analytical expression of the time response. For ordinary differential equations, we have shown that it is possible to obtain accurate inversion of oscillatory functions by using either higher I_{MN} approximants in a global manner or I_{MN} step by step techniques. I_{MN} global method gave accurate results for steep responses either in ordinary or partial differential equations. Through the concept of acuity and equivalent-width (Zakian, 1969; Taiwo and King, 2002) and the derivation of the I_{MN} formula given in the Appendix, we explained why the use of high N or small h gave accurate I_{MN} results. In general, the use of higher approximants facilitated the estimation of the error in the results. Another powerful method of Laplace transform inversion is the method of Honig and Hirdes (1984). This method, which unlike I_{MN} approximants, is inapplicable to unstable systems (having poles in the open right half plane) has been applied to the examples where it is applicable yielding agreeable results. Although this method automatically gave a rough estimate of the error, higher I_{MN} approximants have been exploited to

accurately estimate the errors for situations where there were no analytical Laplace inversions. For example, while MATLAB or double precision arithmetic offered by FORTRAN would in general be good enough for computations involving up to N=16, it would be preferable to utilize extended or infinite precision arithmetic for N>16 in order to minimize rounding errors. For our case where Mathematica had been used, knowing the range of values of the I_{MN} constants facilitated the specification of the number of digits (or working precision) for an accurate determination of the I_{MN} constants and the subsequent numerical Laplace inversion. Consider for example that one needs to use $I_{145,160}$ approximant, then at least 100 digits should be specified in the computation of the I_{MN} constants and the subsequent numerical Laplace inversion. The final number of digits specified will be determined by the desired accuracy, the smallest value of time, t, and the largest value of $F(\alpha_i/t)$, see (2). Note that in using the I_{MN} method and for economy of computation, the I_{MN} constants were computed once and stored for subsequent use.

Since the computation time was larger when a computer working precision was set higher than the default, it is expedient to use the minimum working precision (higher than default) guaranteing computed results of desired precision. A novel algorithm has been devised by Taiwo et al (2006) to ensure this.

REFERENCES

Carmola, R. E. and Chimowitz, E. H. (1990): Analysis of modal reduction techniques for the dynamics of general Tri-diagonal systems. *Comp. Che. Eng*. **14** 227-239.

Celebi, C. and Chimowitz, E. H. (1985): Analytic reduced-order dynamic models for large equilibrium staged cascades. AIChEJ, 31, 2039-2051.

Chen, T. L. and Hsu, C. J. T., (1987). Prediction of breakthrough curves by the application of Fast Fourier Transform. *AIChEJ*, **33**, 1387-1390

Cheney, W. and Kincaid, D. (1999). *Numerical mathematics and computing*. (Pacific Grove: Brooks/Cole Publ. Co.)

Danckwerts, P. V., (1953). Continuous flow systems, *Chem. Eng. Sci.***, 2**, 1-9

Edwards, M. J. (1977). Applications of Zakian's I_{MN} and J_{MN} approximants to the unsteady state solution of the differential equations of a periodically cycled plate column. *Chem. Eng. J. & Biochem. Eng. J.,* **13**, 119-125

Evans, D. J., Shanehchi, J. and Rick, C. C. (1985). A modified bisection algorithm for the determination of the eigenvalues of a symmetric tridiagonal matrix. *Numer. Math*. **38**, 417-419

Honig, G. and Hirdes, U. (1984). A method for the numerical inversion of Laplace transforms, *J. Comp. Appl. Math.,* **10**, 113-132

Kim, C. and Friedly, J. C. (1974). Approximate Dynamic Modeling of Large Staged Systems. Ind. Eng. Chem. Proc. Des. Dev. 13, 177-181

Prabhu, E. S. and Chidambaram, M. (1991). Robust Control of a Distillation Column by the Method of Inequalities. J. Proc. Cont 1, 171-176.

Rice, R. G. and Do, D. D. (1995). *Applied mathematics and modeling for chemical engineers*. New York: John Wiley & Sons

Shimizu, K., Holt, B. R., Morari, M. and Mah, R. S. H. (1985). Assessment of control structures for binary distillation columns with secondary reflux and vaporization. Ind. Eng. Chem. Proc. Des. Dev. 24, 852-858

Skogestad, S., Morari, M. and Doyle, J. C. (1988). Robust control of ill-conditioned plants: high-purity distillation. *IEEE Tran. Aut. Cont*. 33, 1092-1105

Saff, E. B. and Varga, R. S. (1975). On the zeros and poles of Padé approximants to e^z. *Numer. Math.* 25, pp. 1-14.

Seidel-Morgenstern, A. (1991). Analysis of boundary conditions in the axial dispersion model by application of numerical Laplace inversion. *Chem. Eng. Sci.*, **46**, 2567-2571

Stoever, M. A. and Georgakis, C. (1982). Time domain order reduction of tridiagonal dynamics of staged processes. *Chem Eng Sci*, 37, 687-698

Taiwo, O. (1980). Application of the method of inequalities to the multivariable control of binary distillation columns. *Chem. Eng. Sci*, **35,** 847-858

Taiwo, O., Schultz, J. and Krebs, V. (1995). A comparison of two methods for the numerical inversion of Laplace transforms. *Comp. Chem. Eng.* **19**, 303-308

Taiwo, O. and R. King, 2001, "The Computation of higher I_{MN} Constants and Application to the Accurate Determination of Numerical Laplace Inversion", 2001 International Mathematica Symposium, Tokyo Denki University, Chiba New Town Campus, Japan, pp 459-466

Taiwo, O. and R. King, 2002, "Rapid Solution of Stiff Differential Equations Accurate Numerical Laplace Inversion of Steep and Oscillatory Functions using I_{MN} Approximants", Dev. Chem. Eng., Mineral Process. Vol 10, pp 143-164.

Taiwo, O. and R. King, 2003, "Determination Of Kinetic Parameters For The Adsorption Of A Protein On Porous Beads Using Symbolic Computation And Numerical Laplace Inversion", Chemical Engineering & Processing vol 42 pp561-568.

Taiwo, F., Daramola I. and Koya, N., 2006, Efficient Computation of I_{MN} Constants needed in numerical Laplace Inversion Using Mathematica, Proceedings of the 36th Annual Conference and Annual General Meeting, 23rd – 25th Nov, Ibadan, Nigeria

Taiwo, O., Adeyemo, S. and Bamimore, A. (2014a). Centralized robust multivariable controller design using optimization, 19th World Congress of IFAC, Cape Town, South Africa, August 24-29, 6pp

Taiwo, O. and Sorinolu, A. (2014b). Multivariable Design Procedure Based on Optimization, Proceedings 44th Annual NSChE Conference, Owerri, 20th -22nd November, 9pp

Whidborne, J. F. and Liu, G. P. (1993). *Critical control systems: theory, design and applications*. Taunton: Research Studies Press.

Wolfram, S. (1999). *The Mathematica book* (4th ed.). Champaign & Cambridge: Wolfram Media and Cambridge University Press

Zakian, V. (1975a). Properties of I_{MN} and J_{MN} approximants and applications to numerical inversion of Laplace transforms and initial value problems. *J. Math. Anal. Appl.*, **50**, 191-222

Zakian, V. (1975b). Applications of J_{MN} approximants to numerical initial value problems in linear differential-algebraic systems. *J. Inst. Math. Appl.*, **15**, 267-272

Zakian, V. (1979). New formulation for the method of inequalities. *Proc. IEE*, **126**, 579-584

Zakian, V. (1996). Perspectives on the principle of matching and the method of inequalities. *Int. J. Contr*. 65, 147-175.

Zakian, V. and Edwards, M. J. (1978). Tabulation of constants for full grade I_{MN} approximants. *Math. Comp.*, **32**, 519-531

Zakian, V. (1969). Stiff equations solved by numerical inversion of Laplace transform, Report No. 51, Control Systems Centre, UMIST, Manchester, England

APPENDIX

Derivation of the I_{MN} Formula (2)

Using the property of the Dirac delta function, we have

$$f(t) = \frac{1}{t}\int_0^\infty f(\lambda)\delta(\frac{\lambda}{t} - 1)d\lambda$$

(A.1)

Following Zakian (1975a) the function $\delta(\frac{\lambda}{t} - 1)$ can be expressed in terms of the series

$$\delta(\frac{\lambda}{t} - 1) = \sum_{i=1}^{\infty} K_i \exp(-\alpha_i \frac{\lambda}{t})$$

(A.2)

where the α_i and K_i are defined by (3) for the case N = ∞

If we denote the sequence δ_N as the partial sum of δ, then

$$\delta_N(\frac{\lambda}{t} - 1) = \sum_{i=1}^{N} K_i \exp(-\alpha_i \frac{\lambda}{t})$$

(A.3)

and

$$f_N(t) = \frac{1}{t}\int_0^\infty f(\lambda)\delta_N(\frac{\lambda}{t} - 1)d\lambda$$

(A.4)

which on substituting for δ_N from (A.3) into (A.4) yields

$$f_N(t) = \frac{1}{t}\sum_{i=1}^{N} K_i \int_0^\infty f(\lambda)\exp(-\alpha_i \frac{\lambda}{t})d\lambda$$

(A.5)

which is the same as (2). For the purposes of the discussion in the body of the paper we also define (A.5) as

$$f_N(t) = \int_0^\infty f(\lambda)\Delta_N(\frac{\lambda}{t} - 1)d\lambda$$

(A.6)

where

$$\Delta_N(\frac{\lambda}{t} - 1) = \frac{1}{t}\sum_{i=1}^{N} K_i \exp(-\alpha_i \frac{\lambda}{t})$$

(A.7)

(A.6) represents a linear transformation T_N, which converts f into f_N, and may therefore be written in the form

$$f_N = T_N[f(\lambda)]$$

(A.8)

DEDICATION TO PROFESSOR VLADIMIR ZAKIAN

I am dedicating this work to the late Prof Vladimir Zakian of the University of Manchester Institute of Science and Technology (UMIST) Control Systems Centre. I first heard his name from Prof Larry Gibilaro, another giant, while I was in the second year of the three year BSc program in Chemical Engineering at University College, London. Prof Gibilaro then introduced the class to numerical Laplace Inversion in general and his on-going work in particular. We all respected him as very brilliant, but were taken aback that he had so much regard for Zakian's work in this area. My working with Prof Zakian was fortuitous as my going to UMIST was precipitated by a piece of advice from Prof Alvin Nienow, my then personal tutor, and another academic giant, based on its high standards and not to work with any particular personality. I did not even know that Prof Zakian was in UMIST. Suffice it to say that he supervised both my MSc and PhD works and he was definitely more than a supervisor. He was a mentor and father figure. He was ready to play with me if I did my work as instructed but was ready to be harsh if I was slack with it. We sometimes went swimming together and we discussed almost any subject under the sun. He taught me to be Spartan in my living and amply demonstrated this in his own life. He detested junk food and often took me to health food restaurants. He also encouraged me to publish in very high quality journals rather than conference proceedings. This may explain the rigour with which I normally work. I was always welcome to the suburban solace of his Cheshire home. I visited him last in 2000 while on an Alexander von Humboldt Fellowship to Germany through funding provided by a joint research project with our Japanese Colleagues from Tohoku University in Sendai. I additionally visited and gave a talk on my research at King's College, London, being hosted by Dr James Whidborne, a former student of Prof Zakian, who worked with him much later after me. The last collaborative work he and we his former students did was to produce our research work as a collection in a book titled ***CONTROL SYSTEM DESIGN A NEW FRAMEWORK*** **published by Springer Verlag (2005) and edited by V. Zakian.** Four of us his former students met at the 2014 IFAC World Congress in South Africa (to which I went with one of my PhD students), sharing the same table. None of the other three met me in Manchester, but we were always introduced to each other even in absentia by the father himself. We, his former students usually relate as though from the same family even though we, in this case, were a Nigerian working in Nigeria, a white South African working in England, a Chinese working in England and an Indonisean working in his country. We quickly planned to go out together for a good time the following day. Alas I missed this as I had been booked for my return trip early the next morning. Since his death in 2012, the cohesion of the group has slackened somewhat and we all sorely miss him. He was a superb organizer, brilliant engineer and good man.